Republic of Iraq
Ministry of Higher Education & Scientific Research
University of Babylon
College of Science for Women
Laser Physics Department

Study Structural, Optical and Electrical Characteristics of Heterojunctions SiC doped with Silver Oxide Nanostructures Thin Films using PLD in Sensing Applications

A Thesis

Submitted to the Council of the College of Science for Women,

University of Babylon

In Partial Fulfillment of the Requirements for the Degree of

Doctor of Philosophy in Laser Physics and its Applications

By

Hussein Hamad Khudhur

B.Sc. Physics, University of Al-Mustansiriya (1996)
M.Sc. Physics, University of Kufa (2017)

Supervised by

Assist. Prof. Dr. Jinan Ali Abd

2022 A.D. **1443 A.H**

بِسْمِ اللّهِ الرَّحْمنِ الرَّحِيمِ

﴿هُوَ الَّذِي جَعَلَ الشَّمْسَ ضِيَاءً وَالْقَمَرَ
نُورًا وَقَدَّرَهُ مَنَازِلَ لِتَعْلَمُواْ عَدَدَ
السِّنِينَ وَالْحِسَابَ مَا خَلَقَ اللّهُ ذَلِكَ إِلاَّ
بِالْحَقِّ يُفَصِّلُ الآيَاتِ لِقَوْمٍ يَعْلَمُونَ﴾

صَدَقَ اللهُ العليّ العَظيم

سورة يونس الآية (5)

Supervisoŕ s certificate

I certify that this thesis entitled "***Study Structural, Optical and Electrical Characteristics of Heterojunctions SiC doped with Silver Oxide Nanostructures Thin Films using PLD in Sensing Applications***" was prepared by the student (***Hussein Hamad Khudhur***) under my supervision in the department of Laser Physics, College of Science for Women, University of Babylon, as a partial fulfillment of the requirements of the degree of Doctorate of philosophy in laser physics and its applications.

Signature:
Name: Jinan Ali Abd
Title: Assistant Professor
(Supervisor)
Date: / / 2022

Head of the Department Certificate

In view of the available recommendations, I forward this dissertation for debate by the examining committee.

Signature:
Name: Jinan Ali Abd
Title: Assistant Professor
(Head of Laser Physics Department)

Examination Committee Certification

We certify that after reading this thesis, entitled: "***Study Structural, Optical and Electrical Characteristics of Heterojunctions SiC doped with Silver Oxide Nanostructures Thin Films using PLD in Sensing Applications***" and as committee, examined the student "***Hussein Hamad Khudhur***" its contents and that in our opinion it meets the standards of a thesis for the Degree of Philosophy of Doctorate in Laser Physics and its Application.

Signature:
Name: **Dr. Nadir Fadhil Habubi**
Title: Professor
Date: / / 2022
(Chairman)

Signature:
Name: **Dr. Alaa Jewad K. Al- Gidsawi**
Title: Professor
Date: / / 2022
(Member)

Signature:
Name: **Dr. Oday A. Al- Owaedi**
Title: Assistant Professor
Date: / / 2022
(Member)

Signature:
Name: **Dr. Asmahan Asaad Muhmood**
Title: Assistant Professor
Date: / / 2022
(Member)

Signature:
Name: **Dr. Mohammed Hamza Al- Mamoori**
Title: Assistant Professor
Date: / / 2022
(Member)

Signature:
Name: **Dr. Jinan Ali Abd**
Title: Assistant Professor
Date: / / 2022
(Member/Supervisor)

Approved by the Dean of College

Signature:
Name: **Dr. Abeer Fauzi Murad**
Title: Professor
Address: Dean of the College of Science for Women.
Date: / / 2022

Dedication

To: Army Martyrs of Iraqi

To: My Family and Friends

Acknowledgement

First of all, Praise is to Allah, mercy and peace are to the Prophet Mohammed and his relatives and companions.

I would like to express my deep thanks and gratitude to my supervisor, Assistant Professor Dr. Jinan Ali Abd for suggesting this work and for her guidance and help.

I am deeply grateful to the Head of the Laser Physics Department, the staff and the dean of the College of Science for Women for the supporting that provided.

I wish to express my thanks to all my friends, especially the (Ph.D) group, for their kind assistance and support during our course studies and thesis work.

Hussein

Abstract

The PLD technique was used to prepare SiC:AgO thin films with different AgO ratios (1, 3, 5, and 7) wt% and study the structural, optical, and electrical properties of these films, where this technique could be considered a highly efficient in the production of such films. The films were deposited using a Q-switched Nd:YAG laser with a wavelength of (1064 nm), with a number of pulses (1000 pulse), a repetition rate (6 Hz), and an energy per pulse of (500 mJ), while the pressure inside the deposition chamber was (10^{-4} mbar) and the substrate temperature was about (250 ℃).

Structural properties of the as-deposited thin films using the X-ray diffraction (XRD) technique were studied. The results showed that the SiC:AgO films have a polycrystalline structure with a cubic phase. Also, it is noted that the increase in the average crystal size is irregular due to the addition of silver oxide atoms, where the highest value was for the sample (1% AgO) while the lowest value was for the sample (7% AgO).

The results of field emission scanning electron microscopy (FESEM) and energy-dispersive X-ray spectroscopy (EDX) showed that the shape of the particles was irregular and with different sizes that gradually increased with the increase in the ratios of doping.

The surface topography of the films under study was studied using atomic force microscopy (AFM), where the highest value of the surface roughness (Ra), root mean squared (RMS), and particle size was of the film (3% AgO) and the lowest value was for the film (7% AgO).

The optical properties of the films were studied in the spectral range (200 - 900) nm, while the thickness of all films under study was about (200 ± 5) nm. It was found that the increase in the AgO ratios led to a decrease

in the energy gap from (2.61 eV) to (2 eV) and the transition of the indirect type allowed, in addition to calculating some the optical constants for all films.

The electrical properties were studied as the Hall effect, where the results of the sample examination show that the values of Hall's constant (R_H) decrease gradually with the increase of the doping ratios and all films are n-type, it is also noted that the values of the kinematics of charge carriers (μ_H) decrease for the same reason mentioned above.

The current-voltage characteristics of the prepared (SiC:AgO/p-Si) films heterojunction showed that the forward bias current at illumination changes exponentially with the applied voltage and that the efficiency values are very slight, and gradually increase due to the increase in the concentration of charge carriers as a result of the change in AgO ratios.

The sensing properties of thin films prepared by the PLD were measured on different substrates of silicon (SiC:AgO/Si) and glass (SiC:AgO/glass) for ammonia (NH_3) and nitrogen dioxide (NO_2) at different operating temperatures. The results showed that all samples deposited on silicon substrate can operate at room temperature, while samples that were deposited on glass substrate operate at high temperatures (200 ℃).

For samples deposited on a silicon substrate, the maximum sensitivity of SiC:AgO films was (62.98%) for (3% AgO) gas sensor of NO_2 gas at (25 ℃), and the fastest response time was (12.6 s) and (13.5) for the NH_3 and NO_2 gases at (100 ℃) of the (3% AgO) sample, while the fastest recovery time was (33.3 s) and (30.6 s) at (100 ℃) and (200 ℃) for NH_3 and NO_2 gases of SiC sample.

Abstract

For samples deposited on a glass substrate, the maximum sensitivity for SiC:AgO films were (90.77%), (91.89%) for NO_2 gas at (300℃) of (1% AgO) and (7% AgO) samples respectively, and the fastest response time was (11. 7 s) and (6.3 s) at (300 ℃) and (250 ℃) for NH_3 and NO_2 gases of SiC sample at (300 ℃) and (200 ℃) respectively, the fastest recovery time was (34.2 s) of (1% AgO) sample at (250 ℃).

Table of Contents

List of Symbols

Symbol	Physical meaning
D_m	The supersaturation of laser plasma
k_B	Boltzmann's Constant
T_s	substrate temperature
R_a	The actual deposition rate
R_e	The deposition rate of the thin film
n_o, p_o	The equilibrium carrier concentrations
n_i	The intrinsic carrier concentrations
λ	Wavelength
d_{hkl}	The interplanar distance
hkl	Miller indices
θ	Bragg diffraction angle
a	The lattice spacing
D	Average Crystallite Size
β	The full width at half maximum
δ	Dislocation Density
ε	Microstrain
I_A	The intensity of absorbed light
I_o	The intensity of incident light
A	Absorbance
I_T	The intensity of transmitting rays

List of Symbols

T	Transmittance
R	Reflectance
λ_{max}	The maximum wavelength
h	Planck constant
ν	The incident photon frequency
c	The velocity of light in a vacuum
α	Absorption Coefficient
t	The thickness of the film
E_g	Optical band gap
E_a	Activation energy
E_P	The energy of an absorbed or emitted phonon
n_c	Complex refractive index
n	The refractive index
k_o	Extinction Coefficient
ε_r	The real part of dielectric constant
ε_i	The imaginary part of dielectric constant
R_H	Hall coefficient
V_H	Hall voltage
B	The magnetic field
p	The carriers concentrations of holes
n	The carriers concentrations of electrons

List of Symbols

e	The charge of the electrons
μ_p	The mobility for holes
μ_n	The mobility for electrons
σ_p	The Conductivity of holes
σ_n	The Conductivity of electrons
σ	Electrical Conductivity
μ_H	Hall Mobility
I-V	Current-Voltage
I_{Ph}	Photocurrent
I_{sc}	Short circuit current
V_{oc}	Open circuit voltage
I_s	The reverse saturation current
I_L	The light generated current
R_s	The series resistance
R_{sh}	The shunt resistance
V_m	Maximum voltage
I_m	Maximum current
F.F	Fill Factor
η	Conversion efficiency
P_o	Maximum power
P_{in}	Input power
S	Sensitivity

List of Symbols

R_a	The resistance of the sensor in the air
R_g	The resistance of the sensor in the presence of a gas
I_a	Sample current measured at ambient environment
I_g	Sample current measured under the test gas
τ_{res}	The response time
τ_{rec}	The recovery time
x	The width of the light fringes
y	The width of the dark fringes

List of Abbreviations

Symbol	Physical meaning
PVD	Physical Vapour Deposition
CVD	Chemical Vapour Deposition
PLD	Pulse Laser Deposition
SEM	Scanning Electron Microscopy
XRD	X-Ray Diffraction
AFM	Atomic Force Microscopy
FESEM	Field Emission Scanning Electron Microscopy
XPS	X-ray Photoelectron Spectroscopy
PL	Photo Luminescence spectroscopy
HW-CVD	Hot-Wire Chemical Vapor Deposition
HJ	Heterojunction
KrF	krypton fluoride laser
RF-PECVD	Radio-Frequency Plasma-Enhanced Chemical Vapor Deposition
FTIR	Fourier Transform Infrared Spectroscopy
HR-TEM	High-Resolution Transmission Electron Microscopy
TEM	Transmission Electron Microscopy
IR	Infrared
NCs	Nanocauliflowers
FWHM	Full Width at Half Maximum

List of Abbreviation

V.B	Valence Band
C.B	Conduction Band
PV	Photovoltaic
EDX	Energy-dispersive X-ray spectroscopy
Nd:YAG	Neodymium-doped yttrium aluminium garnet
HF	Hydrofluoric acid
3D	Three-dimensional
RT	Room temperature
R.M.S.	Root Mean Square
UV	Ultra Violet
ViS	Visible Spectrum

List of Tables

List of Figures

List of Figures

Chapter One

General Introduction

1.1 Introduction

The significant progress in thin-film growth techniques has attracted many researchers to manufacture devices based on thin film. The substitution of traditional bulk materials with thin films enables the manufacture of devices with a smaller weight and size and good performance and low cost. The structural, electrical, and optical properties of thin film-based devices have a crucial role in improving efficiency. There is great interest in studying materials with a wide bandgap. At the same time, electronic devices are being minimized to replace silicon as a base material in these devices for new applications such as high levels of radiation and high temperatures devices [1].

Nowadays, developments of semiconductor materials and devices have been a strong driving force for various revolutionary changes and innovations in modern fields. Electronic and optoelectronic devices based on silicon carbide (SiC) have been widely studied for use in high voltage, high temperature, and extreme radiation conditions where traditional silicon (Si) devices cannot perform well. In particular, the high temperature and high power characteristics of SiC provide substantial economic benefits to industries such as aerospace, power, automotive, and energy production [2].

The distinguished advancements in science and technology for SiC have led to the achievement of sensors, strong material structures, and electronics. Those have been achieved via the ability to deposit SiC thin films, manufacture nanostructures, engineer stable metal contacts, and etch features for SiC. The fundamental motivation for creating the SiC materials platform is to overcome the constraints of existing Si-based

platforms. Due to heat carriers and junction leakage production, Si can only be used at temperatures below (200℃). Furthermore, the poor chemical resistance and the poor radiation tolerance of Si-based devices require the use of alternative materials to mitigate the need for complex packaging and active cooling [2, 3].

As a consequence of its temperature tolerance, radiation resistance, biocompatibility, and chemical inertness, SiC has emerged as a material to overcome the limitations of Si. SiC has been used as the structural material in constructing high-temperature energy conversion devices and sensors that have functioned in harsh settings such as high temperatures, corrosive chemical environments, and great shock [3].

1.2 Thin Films

Thin film technology is considered one of the most essential techniques that contributed to the development of the study of semiconductors and gave a clear idea of their properties. The term "thin films" is used to describe a layer or many layers of atoms of a substance whose thickness ranges from fractions of a nanometer (monolayer) to less than about one micrometer. Because it is thin and fragile, it must be deposited on a solid material such as glass or silicon or some salts or polymers. Thin films have properties and advantages that are not available in the compositions of other materials. Their infinitesimal thickness and the large surface-to-volume ratio give them a unique physical composition that is at times comparable to a monocrystalline structure and sometimes superior to it [4].

All modern electronic devices depend entirely on their work on their materials with physical and chemical properties specific to semiconducting materials that possess insulating properties at low temperatures and have the ability to electrical conduction when their

temperature rises to a certain extent. The study of the properties of any material in the form of thin films, as known, is one of the very important topics. The material as a thin film has applications in many fields, especially electronics such as solar cells, photovoltaics, reagents, and sensors [5].

1.3 Thin Films deposition techniques

Thin-film preparation techniques can be divided into two categories depending on the nature of the deposition [5, 6]:

1. Physical vapour deposition technique (PVD)
2. Chemical vapour deposition technique (CVD)

1.3.1 Physical vapour deposition technique

The physical vapour deposition technique is used to deposit the material from the target over a substrate in a few angstroms to several micrometres. The deposition process in PVD involves the following steps [5, 6]:

1. The first stage is the high energy transfer to the target material utilizing filament heating or bombardment of electron/ion over the target material.
2. In the second stage, the target material vaporizes due to energy transfer through evaporation, sublimation, or physical sputtering to the target atom under high vacuum or low-pressure conditions.
3. In the third stage, the transportation of vaporized target material travels towards the substrate surface.
4. The fourth stage involves the reaction between the vaporized target material and the gas present in the chamber during transportation.
5. In the fifth stage, the vaporized material transported to the substrate surface undergoes a condensation process that induces the growth of the thin film.

In the physical vapour deposition technique, the deposition is carried out through the vaporization of the target material by either thermal or athermal processes. In a thermal process, the target material undergoes sublimation or evaporation through the supply of thermal energy. In contrast, vaporization physically strikes the ionized gas molecules over the target material in an athermal process. Hence, the overall PVD process involves transporting material at an atomistic level to the substrate surface leading to the formation of the thin film. Figure (1.1) explains all the five stages of the PVD process during the deposition [5, 6].

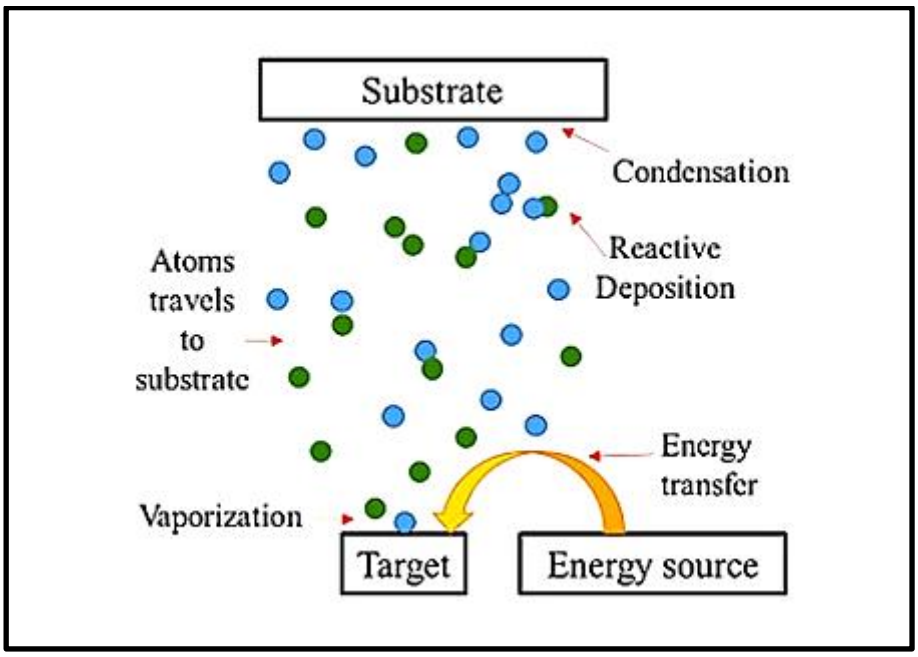

Figure (1.1): Schematic representation of the five stages of the PVD process [5].

1.3.2 Chemical vapor deposition technique

The CVD process involves the reaction of vapour phase chemicals with the substrate to result in the deposition of the thin film. CVD is a versatile technique used to form simple and complex compound thin films with desired morphology and chemical compositions. Both organic and inorganic materials can be fabricated as thin films using the CVD

technique. The deposition process in CVD, which is shown in figure (1.2) involves the following steps [5, 6]:

1. In the first reaction stage, the reactant gas (precursor) and the carrier gas (inert gas, if required) are introduced into the reaction chamber at a required flow rate.
2. In the second stage, the adsorption of reactant gas takes place over the substrate, where the reactant gases undergo a chemical reaction activated by the thermal energy of the ionized plasma.
3. In the third stage, these gases undergo surface diffusion and decomposition on the substrate, which leads to the formation of nucleation sites.
4. In the fourth stage, the by-product formed on the substrate undergoes desorption and is carried out through the outlet of the reaction chamber.

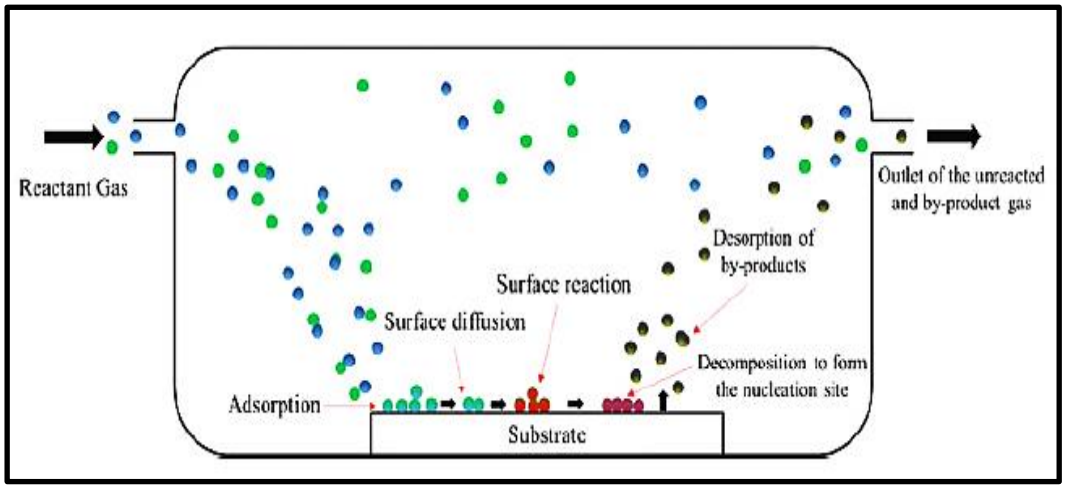

Figure (1.2): Schematic representation of the four steps of the CVD process [5].

The quality of the thin film formation is determined by the thermodynamics and kinetics of the chemical reaction, the flow rate of the gaseous reactant, the substrate temperature, and the chemical-physical properties of the substrate.

The classification of the thin-film technique based on the nature of the deposition process is shown in figure (1.3) [5, 6].

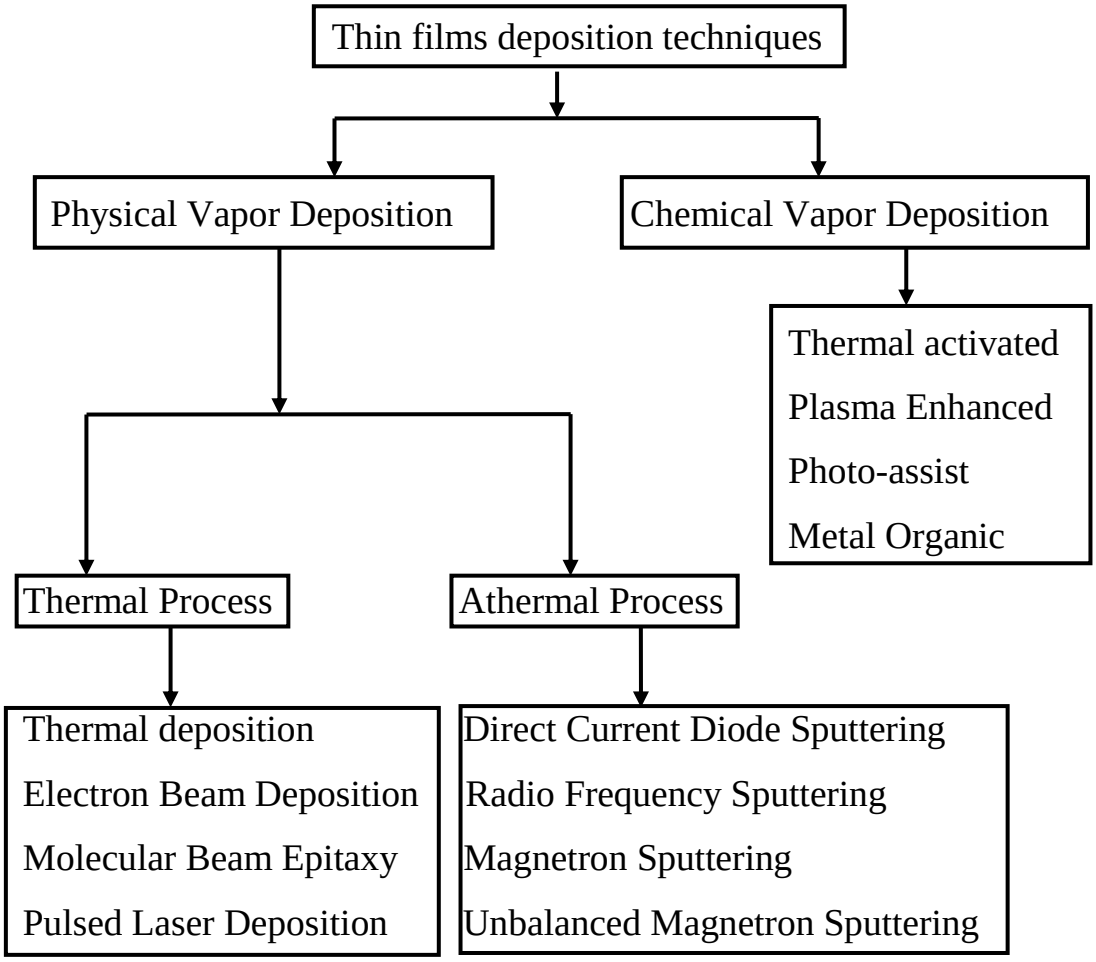

Figure (1.3): Classification of thin film deposition technique [5, 6].

1.4 Thin Film Growth Mechanism

The vaporized atom from the target material travels towards the substrate inside the vacuum chamber. Accordingly, the vaporized atom impinges on the substrate surface either by chemisorption or physisorption. At the initial stage, the adsorbed atom (adatom) reaching the substrate surface has its energy transferred to the atom during vaporization. Also, in most PVD processes, the substrate is kept at higher temperatures during deposition. Hence, the adatom arriving on the substrate undergoes migration either by its initial energy or substrate energy or both. The different parameters of the PVD process, such as substrate temperature, deposition rate, and residual gas pressure, influence adatom's migration energy during the growth process of the thin

film [5, 7]. The growth mechanisms involved in the formation of thin films can be divided into three modes: as shown in figure (1.4) [5]:

1. Island growth (Volmer Weber):
    a) Form three dimensional islands.
    b) Film atoms are more strongly bound to each other than to the substrate.
    c) Slow diffusion.
2. Layer-by-layer growth (Frank–van der Merwe):
    a) Generally, the highest crystalline quality.
    b) Film atoms are more strongly bound to the substrate than to each other.
    c) Fast diffusion.
3. Mixed growth (Stranski-Krastanov):
    a) Initially layer by layer.
    b) Forms three-dimensional islands.

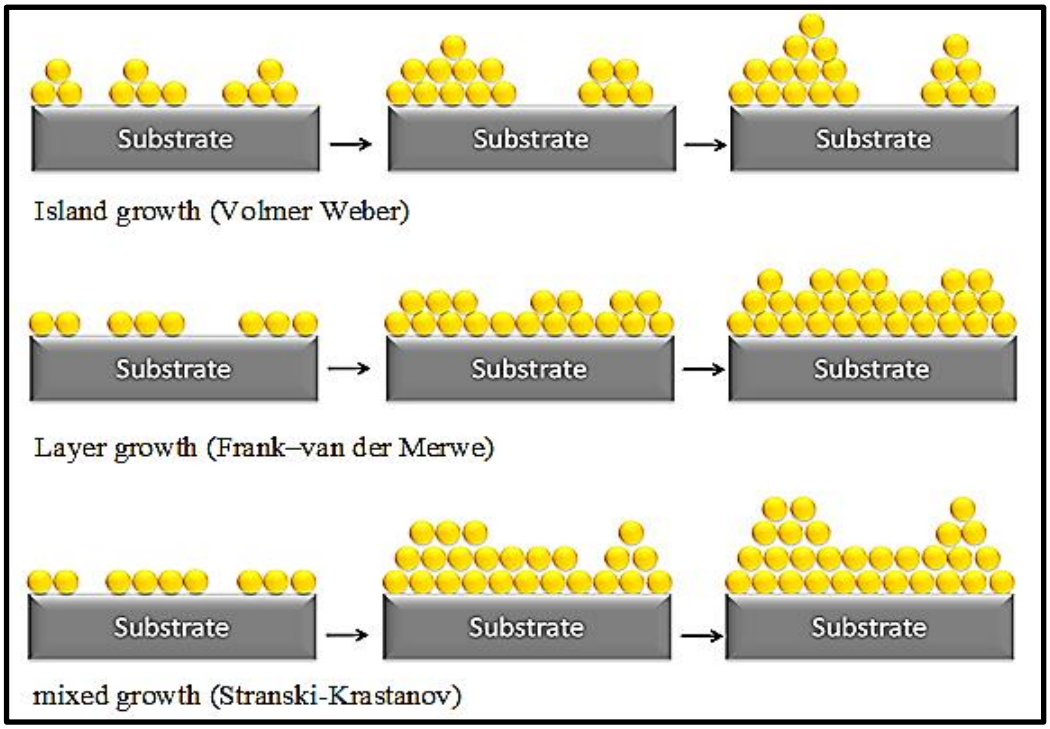

Figure (1.4): Thin film deposition growth mechanisms [5].

1.5 Silicon Carbide

1.5.1 Crystal structure of SiC

Silicon carbide is the only chemically stable form of silicon and carbon. SiC is a binary compound consisting of Si and C atoms, which are group IV elements. The basic building block of a silicon carbide crystal is the tetrahedron of four carbon atoms with a silicon atom in the centre. Each silicon atom (or carbon atom) shares its electrons with four C atoms (or silicon atoms), which means that every atom makes a covalent bond with its four neighbouring atoms, and vice versa. As shown in figure (1.5), the distance between the carbon and silicon atoms is 1.89 Å, while the distance between Si or C atoms is about 3.08 Å. Further, the bonding between Si and C atoms is 88% covalent and only 12% ionic [8-11].

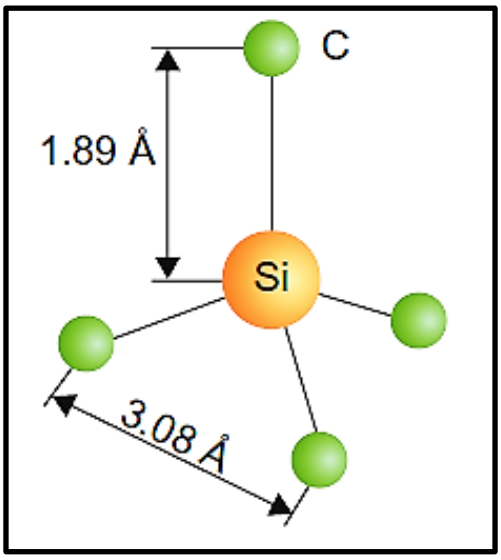

Figure (1.5) The Basic structural unit in silicon carbide [8].

1.5.2 Physical Properties of SiC

The crystalline structure of silicon carbide can be considered a close-packed stacking of double layers of Si and C atoms. The stacking of the double layers follows one of three possible relative positions, which are arbitrarily labelled A, B, and C, as shown in figure (1.6); each letter represents a bilayer of individual Si and C atoms. Different stacking

sequences of these three double layers result in many other crystal structures called polytypes. The polytype can be defined as the ability to crystallize in several different crystal structures despite all SiC polytypes having the same atomic composition of carbon and silicon. Each polytype has its own distinct set of semiconductor properties depending on the stacking periodicity of similar planes. Despite more than 250 different polytypes of SiC having been identified, only three crystalline structures (cubic, hexagonal, and rhombohedral) exist. The cubic structure of SiC has been referred to as β-SiC, while the hexagonal and rhombohedral structures are called α-SiC. By adopting a more descriptive nomenclature that identifies the crystalline symmetry and stacking periodicity, cubic SiC is denoted 3C-SiC, wherein the number (3) represents the number of double layers in the stacking sequence, and the letter (C) represents the crystal structure. It is noticeable that each polytype differs in terms of the bandgap, and other fundamental properties. Therefore, SiC can be considered as a family of a large number of semiconductors. The most common polytypes are 3C (cubic), 4H and 6H (hexagonal) and 15R (rhombohedral). 4H and 6H have ABAC, and ABCACB stacking sequences, respectively, while 3C has an ABC stacking sequence [12-17].

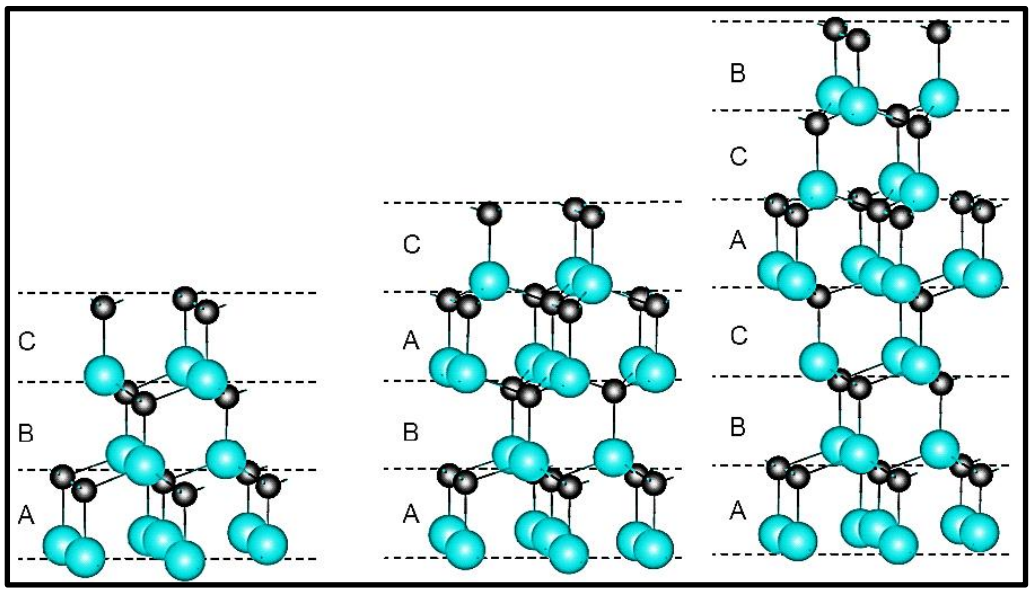

Figure (1.6): The various stacking sequences for 3C, 4H, and 6H in SiC [12].

Compared with Si and GaAs, SiC is a wide bandgap semiconductor with many remarkable properties, such as a higher bandgap, a higher breakdown field, higher thermal conductivity, and a higher saturation drift velocity. These properties make SiC suitable for the fabrication of high-temperature, high-power, and high-frequency electronic devices. The electric properties of SiC differ according to different polytypes; for example, the bandgap for SiC ranges from (2.3 eV) for 3C-SiC to (3.4 eV) for 2H-SiC. Despite having the smallest bandgap, 3C-SiC has the highest electron mobility and saturation drift velocity [18, 19].

Other well-known properties include high hardness, chemical inertness to most acids, and a high melting point (sublimation), making SiC an attractive material for sensors operating in harsh environments. Compared with diamond, another wide bandgap semiconductor, one of the attractive features of SiC is that it can be doped with p- and n-type, by which some essential electric properties could be adjusted. The surface of SiC can be passivated by forming a thermal SiO2 layer, but the oxidation rate is prolonged compared with Si [20]. A summary comparing important semiconductor properties of 3C-, 4H- and 6H-SiC is presented in Table (1.1) [20-24].

Table (1.1): Physical properties of 3C-, 4H- and 6H-SiC [20-24].

Properties	**3C-SiC**	**4H-SiC**	**6H-SiC**
Crystal structure	Zinc blende (cubic)	Hexagonal	Hexagonal
Lattice constant (Å) *a* *c*	4.3596 -	3.073 10.053	3.081 15.12
Density (g/cm^3)	3.21	3.21	3.21
Melting Point (℃)	2830	2830	2830
Band gab (eV)	2.36	3.23	3.05
Refractive index	2.69	2.55	2.65
Dielectric Constant	9.7	9.7	9.6-10
Electron mobility $cm^2/(V \cdot s)$	900	900	400
Hole mobility $cm^2/(V \cdot s)$	320	120	90
Thermal expansion coefficient $℃^{-1}$	4×10^{-6}	4×10^{-6}	4×10^{-6}
Saturated electron velocity ($x10^{-6}$ cm/s)	2.2	2	2
Breakdown field ($x\ 10^5$ V/cm)	20	30	32
Thermal conductivity $(W \cdot m^{-1} \cdot K^{-1})$	360	370	490
Hardness (kg/mm^2)	3980	2130	-

SiC is a compound of silicon and carbide with many superior characteristics, such as a wide (tunable) bandgap, excellent thermal conductivity and thermal shock resistance, good chemical and oxidation resistance, high electron mobility, and biocompatibility [21, 25]. In addition to these well-known characteristics of bulk SiC, interesting

biological, electronic, and optical properties of SiC nanomaterials, which have great potential for applications in electronics, biosensors, aerospace, and optical devices, have received significant interest from the scientific community. SiC can exist in the form of single-crystalline, polycrystalline, or amorphous. The different forms of SiC allow its service in various applications [26-28].

1.5.3 Doping in SiC

Doping is another challenge for SiC device fabrication due to its hardness, chemical inertness, and most impurities' low diffusion coefficient. Doping is a way to change the electronic structure of a material by substituting some of the native atoms with a foreign element. In the case of SiC, this means that some other elements replace either silicon or carbon. The band structure of the material changes depending on which impurity is introduced to the crystal. By choosing the dopants, it is possible to tailor the band structure to create various new properties of the material [29].

An important factor in changing the band structure is the number of valence electrons in the introduced element compared to the element it replaces. Silicon and carbon have four valence electrons, creating four bonds with their neighbouring atoms in the crystal. The electrons are firmly bound to the atomic nuclei, requiring energy corresponding to the bandgap to free one electron. Suppose an element replaces one silicon or carbon atom with five valence electrons. The additional electron is not as strongly bound to the nucleus and can quickly release an electron into the conduction band. This is called a donor atom. Similarly, suppose an atom with only three valence electrons is introduced to the crystal. In that case, it can readily bind an electron from the valence band, creating an electron deficiency, or hole, in the valence band. This is called an acceptor atom.

Figure (1.7) shows a simplified band diagram with a donor and an acceptor level. The donor level donates an electron to the conduction band when the electron is supplied with the energy E_D. When the electron is provided with the energy E_A, the acceptor accepts an electron from the valence band. The energy required to supply the material with one carrier from the dopant level is called the dopant's binding energy (or ionization energy) [29, 30].

As dopants are introduced into the material, the position of the Fermi level relative to the bands changes. The Fermi level resides in the middle of the band for undoped materials, but will move nearer to the conduction (valence) band as donors (acceptors) are introduced. This change in Fermi energy corresponds to a change in occupancy in the different levels [30].

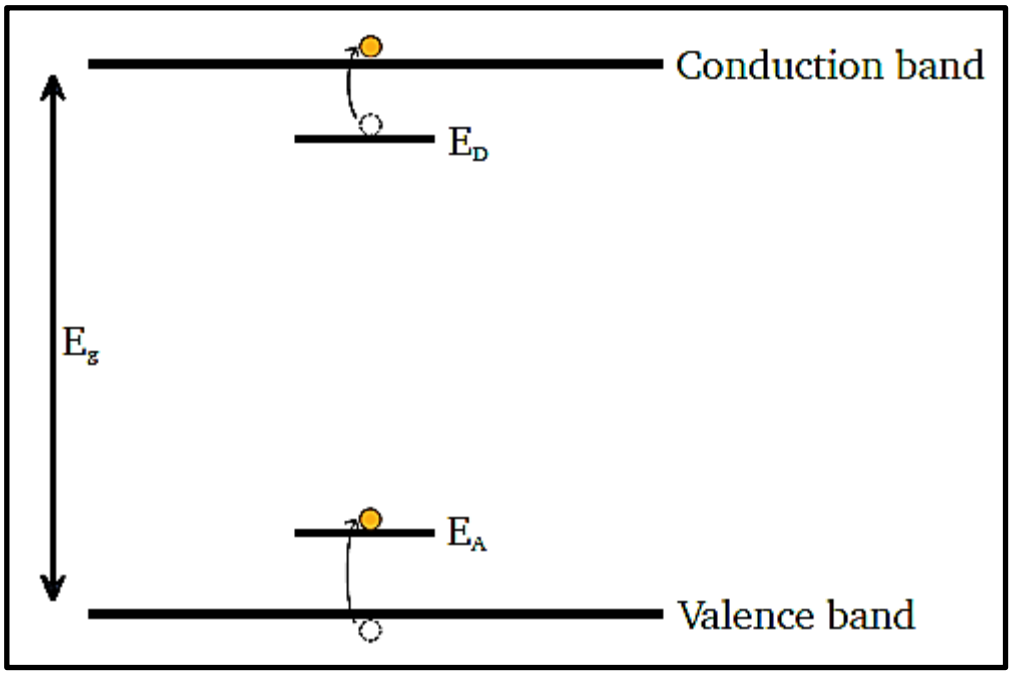

Figure (1.7): Two new energy levels are introduced by doping [30].

1.6 Properties of Silver

Silver is a chemical element with the symbol Ag and atomic number (47). It is located among the transition metal elements in the periodic table in the elements of the fifth period and the eleventh group. Silver has a distinctive color that lies between white and grey. Silver is found in the earth's crust either in its natural elemental free form, or in the form of an alloy with gold, or within the components of some metals. It has distinctive properties, as it has the highest value among metals in terms of electrical and thermal conductivity and reflectivity.

Silver is used in the manufacture of solar panels, water filtration, jewellers, electrical contacts and conductors, specialized mirrors, window coatings, catalysis of chemical reactions, and other applications, while some of their compounds are used in photographic and X-ray film [31].

Silver is similar in physical and chemical properties to its two vertical neighbours in group II of the Periodic Table: copper and gold. Metallic bonds in silver lack a covalent character and are relatively weak. This observation explains the low hardness and high ductility of single crystals of silver. Very high electrical and thermal conductivity are common to the elements in group II. Their single s electron is free and does not interact with the filled d subshell as such interactions lower electron mobility. The thermal conductivity of silver is among the highest of all materials, although the thermal conductivity of carbon and superfluid helium-4 is higher. The electrical conductivity of silver is the highest of all metals, greater even than copper. Silver also has the lowest contact resistance of any metal. Silver is rarely used for its electrical conductivity, due to its high cost where silver plating improves electrical conductivity because those currents tend to flow on the surface of conductors rather than through the interior [32-34]. Table (1.2) shows some physical properties of silver:

Table (1.2): Some physical properties of silver [33].

Properties	Value
Name	Silver
Symbol	Ag
Atomic number	47
Weight number	107.8682
Group and Period	11 and 5
Melting_point	961.78 °C
Boiling point	2162 °C
Phase	Solid
Density (solid)	10.49 g/cm^3
Density (liquid)	9.320 g/cm^3
Crystal structure	Face center cubic (FCC)
Thermal conductivity	429 W/(m·K)
Thermal expansion	18.9 µm/(m·K) (at 25 °C)
Electrical resistivity	$15.87\times10P^{-9}$ Ω.m (at 20 °C)
Thermal diffusivity	174 mm^2/s (at 300 K)
Molar heat capacity	25.350 J/(mol·K)
Mohs hardness	2.5

1.7 Literature Survey

This review summarises the recent scientific research that has received great interest in the past decade on the preparation of pure and doped silicon carbide films by different physical and chemical methods.

Monaco, et al. in (2010) have deposited a thin film of SiC on Si substrate by pulsed laser deposition (PLD) using two different targets. At the same deposition conditions (as laser fluence, target-substrate distance, and repetition rate) and at a high temperature, the resulting films differ depending on the substrate and the target. The properties of the films have been examined by scanning electron microscopy (SEM), atomic force microscopy (AFM) and X-ray diffraction (XRD) techniques. Surface analysis has shown that the film structure is not related to the crystallinity of the target but is more sensitive to the substrate structure [35].

In (2010), *Lim, et al.* have used the crystalline silicon carbide polytype 6H-SiC with an appropriate dopant to fabricate the optical gas sensors and test them at high temperatures (650℃). SiC sensors have been fabricated by doping a 6H-SiC chip with Ga and Al at dopant energy levels. The doped regions exhibit distinct changes in the refractive index of SiC in the presence of CO_2 and NO gases, respectively [36].

In (2011), the pulse laser deposition technique has been applied by *Monaco, et al.* with an Nd:YAG laser (1064 nm) to prepare silicon carbide films on silicon and sapphire (Al_2O_3) substrates at temperatures of (650℃) in a vacuum. XRD, AFM, and SEM techniques have been used to study the structurally and morphological properties of the as-deposited films. The deposition conditions they used led to the formation of highly oriented cubic 3C-SiC on sapphire substrates [37].

Zheng, et al. have used the sol-gel and carbothermal reduction techniques in (2011) to make Mn-doped 3C-SiC nanoparticles. The nanoparticles have an average particle size of (126) nanometers.

Raman scattering experiments show that when Mn was doped, the transverse and longitudinal optical modes shifted to low wavenumbers, and the full widths at half-maximum of Raman peaks increased. The doped-Mn atoms in the 3C-SiC lattice replace the C sites, according to the fine structure revealed by extended x-ray absorption [38].

In (2011), *Kim and Chung* have used electrochemical anodization with a mixture of HF and ethanol as the electrolyte solution to prepare porous 3C-SiC (pSiC) samples from polycrystalline n-type 3C-SiC films. The changes in the resistance were observed according to H_2 concentrations in the range between (110 and 410 ppm). The sputtering of Pd and Pt nanoparticles as a hydrogen catalyst chemically changes the pSiC surface. The capacity of Pd and Pt-deposited SiC samples to detect hydrogen was proven by changes in electrical resistance in the presence of nitrogen diluted with hydrogen. The sample with a pore size of 25 nm exhibited superior sensing characteristics compared to the sample whose pore diameter was (60 nm). The response time, resistance ratio, and response factor all increased with temperature [39].

Bhimasingu, et al. in (2012) have deposited the silicon carbide films on silicon substrates using the PLD technique with an Nd:YAG laser at (355 nm). The influence of the SiC powder grit size, ambient pressure, and substrate temperature on the morphology and structure of SiC thin films have been studied. Experimental studies show that polycrystalline SiC film can be obtained at a temperature ranging between (600 and 700℃) and at a pressure of about (5.5×10^{-3} Pa). The XRD studies on as-deposited films have been exhibited the polycrystalline nature of SiC films (3C-SiC and 4H-SiC) [40].

In (2012), the RF-magnetron sputtering technique was used by *Yukai, et al.* to make Mn-doped silicon carbide films on silicon substrates. The structure, composition, and photoluminescence properties of films

were investigated by XRD, SEM, X-ray photoelectron spectroscopy (XPS) and photoluminescence (PL) as a function of Mn-doped concentration**.** The XRD results show that the Mn-doped SiC films have a preferential (111) orientation of 3C–SiC and the doped Mn atoms occupy the C sites of the SiC lattice. The XPS results indicate that the films include Si-C, C-C, and Si-Mn bonds [41].

In (2012), *Mao, et al.* have used a hot-wire chemical vapor deposition (HW-CVD) method to prepare films of p-type nanocrystalline SiC (p-nc-SiC) as window layers in n-type crystalline Si heterojunction (HJ) solar cells. An X-ray diffractometer and Raman spectroscopy have been used to study the effect of H_2 flow rates on the properties of p-nc-SiC films. The optical and electrical properties of prepared films were also measured. It was found that H_2 flow rates played an important role in the forming of the SiC films and increasing the optical bandgap (E_g) and decreasing the activation energy (E_a). The SiC/Si heterojunction solar cells with an open-circuit voltage of (0.59 V), a short-circuit current density of (38.06) mA/cm^2, a fill factor of (62.03%), and a conversion efficiency of (14.09%) could be obtained after the deposition and hydrogenation parameters were optimized [42].

In (2013), a pulse laser deposition technique was used by *Mishra, et al.* to prepare silicon carbide films on substrates of silicon (100) with a KrF excimer laser (λ=248nm, pulse width 20ns) under pressure (2 x 10^{-5} bar) and at a temperature of (800℃). The films were annealed after deposition at (800℃) for 3 hours. Microstructure and phase studies were carried out by X-ray reflectivity, X-ray diffraction, FESEM, Raman techniques, and SiC films of high elastic modulus and hardness (18 to 19 GPa) have been prepared. The prepared films were used as photodetectors [43].

Ma, et al. used a radio-frequency plasma-enhanced chemical vapor deposition (RF-PECVD) in (2013) to produce Boron-doped amorphous silicon carbide films (a-SiC) as windows layers on nc-Si heterojunction using silane–methane gas mixtures at a low temperature of (150℃). The structural properties of films were investigated using Raman, FTIR, and HR-TEM techniques. The researchers developed a high-quality p-type a-SiC/nc-Si hybrid window layer with tunable nano-sized silicon crystals. For n-i-p-type a-Si single-junction solar cells, high open-circuit voltage (40.96 V) and high quantum efficiency values at short wavelengths were achieved using high-quality p-type window layers and intrinsic a-Si layers [44].

Keffous, A., et al. in (2013) have used a pulsed laser deposition technique to deposit SiC films on the silicon substrate. The properties of current-voltage (I-V) and current–time (I-t) have been measured. Schottky diode characteristics (ideality factor, barrier height, and series resistance) were investigated at different H_2 gas concentrations, where they noticed that they change considerably when exposed to H_2 gas. The effect of H_2 gas concentration on the maximum sensitivity value of the sensor was studied. A high sensitivity value of about (86%) has been obtained at an approximate bias voltage of (1V). In addition, response and recovery times were determined to be (55 s) and (160 s), respectively [45].

In (2013), *Zakhvalinskii, et al.* have prepared thin films of amorphous SiC on a substrate of p-Si (100) by non-reactive magnetron sputtering in an Ar atmosphere. AFM has achieved the surface morphology and the control of the SiC thin film thickness under a low vacuum or controlled atmosphere. The amorphous nature of SiC grown on the Si substrate is confirmed by the presence of the diffraction rings, which indicate the absence of the dominant orientation of the obtained films. Under standard illumination conditions, the I-V characteristics of

n-SiC/p-Si heterojunction solar cells show a conversion efficiency of about 7.22 % [46].

In (2014). a pulse laser deposition technique has been used by Socol, et al. with a KrF excimer laser to prepare silicon carbide films on silicon substrates under different CH_4 pressures and temperatures ranging from (400 to 1000℃). The films were annealed at their deposition temperature under the pressure of (500 mbar) of CH_4 for (1-1.5 h). X-ray diffraction studies indicate that films deposited at (800℃) or higher substrate temperatures were nanocrystalline. The results explained that the SiC films were very hard, with hardness values over (40 GPa) for films deposited at temperatures higher than 800 ℃ [47].

Wang, et al. in (2014) have used the radio frequency magnetron sputtering method to produce the SiC: Mn films on Si (100) substrates. The effect of Mn doping on the structural, magnetic, and transport properties of films was studied. According to the results, Mn-doped SiC films have the 3C-SiC crystal structure. With an increase in Mn content, the carrier concentration increases and resistivity decreases monotonically. The metal-semiconductor transition temperature lowers as the Mn concentration increases, indicating a shift from semiconducting to metallic transport behavior. Magnetic characterizations show that all films are ferromagnetic with a Curie temperature greater than (27℃) [48].

In (2014), *Latha, et al.* used the low-pressure chemical vapor deposition technique to prepare a SiC:N thin film at (1040℃) and (250 Pa) by using methyl trichlorosilane (CH_3Cl_3Si) and ammonia (NH_3) for high-temperature sensor applications. The effect of nitrogen doping concentration on the microstructure, crystallinity, and electrical properties of SiC thin films is analyzed. X-ray diffraction studies revealed that the crystallinity and crystallite size decreased as the nitrogen doping concentration increased. Using atomic force microscopy, the grain size

and average root-mean-squared roughness of SiC thin films are investigated. The increase in the nitrogen concentrations in the film results in an increase in the grain size and a decrease in the barrier height of the grain boundaries, leading to a decrease in resistivity [49].

Ryndya, et al. have used silicon (100) and (111) substrates in (2015) to prepare the SiC films by the PLD technique from α-SiC ceramic target with Nd:YAG laser at substrate temperatures of (30-1000℃) under high vacuum (~10^{-5} Pa). Fourier transform infrared spectroscopy (FTIR), transmission electron microscopy (TEM), SEM, AFM and XRD techniques were used to study the effect of substrate temperature on the composition, structure, and surface morphology of experimental samples. The SiC films prepared at substrate temperatures lower than (500℃) were found to be amorphous [50].

Badea, et al. in (2016) have prepared and studied the hydroxyapatite coatings, enriched with SiC and Ag. SiC and Ag were added to enhance the film's corrosion resistance and antibacterial properties. With different Ag contents, the coatings were deposited on (Ti_6Al_4V) alloy substrates by co-sputtering of hydroxyapatite, SiC, and Ag targets, using a magnetron sputtering system. EDS, XRD, FTIR, SEM, AFM techniques, and electrochemical and antimicrobial tests were used to characterize the films in terms of elemental and phase composition, texture, morphology, corrosion resistance, and antibacterial activity. The effect of Ag content on film characteristics was studied. The investigated coatings demonstrated good ability against possible bacterial infection with different germs [51].

Dey and Alika have studied the effect of substrate temperatures (T_s) in (2016) on the structural and optical properties of nanostructured amorphous silicon carbide (a-SiC) films prepared by the PLD on a fused silica substrate. Fourier transform infrared spectroscopy, Raman

spectroscopy, and XRD have been used to analyze films' compositional and structural properties. The SiC thin films showed amorphous features as confirmed by XRD and Raman studies, and the thin films exhibited slight improvement in crystallinity at higher T_s. The films' thickness, absorption coefficient, optical band gap, and refractive index were determined by the UV-Vis-IR spectra. The refractive index of the films change from (2.99 to 2.54) and the optical band gap increases from (1.5 eV to 2.33 eV) as the substrate temperature increases [52].

In (2017), the boron-doped amorphous silicon carbide thin films have been prepared by *Šály, et al.* using a plasma CVD reactor with parallel plate electrodes to improve the performance of heterojunction solar cells. DC and AC measurements and subsequent evaluations were carried out to analyze the electrical transport mechanisms in the prepared structures. The fill factor values have been found low for all investigated samples because of the low collection of photogenerated carriers [53].

Cheng, et al. have applied the radio frequency magnetron sputtering method under different RF powers in (2017) to prepare the amorphous SiC thin films on a quartz substrate. XRD, AFM, XPS, Raman spectroscopy, and UV-Vis spectroscopy have studied the structural and optical properties. The results showed that the prepared silicon carbide films have different structures and high absorption capacity in the ultraviolet region but a low absorption capacity in the infrared (IR) region. The results revealed that the thin film surface roughness prepared under different RF powers initially increases and then decreases. As the sputtering power increases, the optical bandgap of the thin films ranges between (1.29 eV and 1.80 eV) [54].

In (2018), *Perný, et al.* have used the plasma CVD technique to deposit the pure and boron-doped a-SiC thin layers on the c-Si substrate to improve the performance of solar cells. DC and AC measurements

evaluated the electrical transport mechanisms in the produced a-SiC/c-Si heterojunction solar cell structure. The effect of methane concentration in the deposition gas mixture has been studied and different electrode configurations [55].

Kumar, et al. in (2018) have used DC magnetron co-sputtering to fabricate Pd decorated SiC nanocauliflowers (NCs) thin films on an electrochemically etched porous silicon substrate. The gas-sensing performance of Pd/SiC NCs to hydrogen gas was investigated under a high operating temperature regime (40-500)℃ with a low detection limit (5-500 ppm). The NCs sensor shows a fast response/recovery time (10s/18s), a high sensing response of about (14.48%) and excellent stability when exposed to 100 ppm H_2 at a high temperature of (380℃). The Pd/SiC NCs investigated can be utilized as highly sensitive and selective hydrogen gas sensors in harsh environments at high operating temperatures [56].

Paneerselvam, et al. have prepared the Al-doped SiC films on MgO (100) substrates in (2019) by the PLD technique at a substrate temperature of (800℃). XRD and FTIR were used to confirm the SiC phases and Si-C bond structure of the grown thin films. Measurements based on XRD and Raman scattering techniques confirmed the improvement in crystallization of 3C-SiC thin films with laser-assisted doping. The optical bandgap of the 3C-SiC film was obtained from the UV-visible spectroscopic analysis [57].

In (2019), *Hsu, et al.* have used a high-frequency plasma-enhanced chemical vapor deposition technology to produce boron-doped hydrogenated amorphous silicon carbide (a-SiC:H) thin films as a window layer for silicon heterojunction (SHJ) solar cells. The optical and electrical characteristics of the different a-SiC:H films are studied. It has been shown that a higher CH_4 flow rate leads to an increase in band gap

(2.1 eV) and a reduction in absorption coefficient, but the electrical conductivity is significantly reduced. The highest conversion efficiency can be obtained for the manufactured solar cell (22.14%), which is higher than that from the (a-Si: H) [58].

Tavsanoglu, et al. used the reactive direct current magnetron sputtering technology in (2019) to deposit the SiC thin films of a high purity silicon target with CH_4 as the reactive gas on glass and Si (100) substrates. XRD analyses have shown that the SiC films deposited in this study were amorphous. The microstructural analyses showed the surface roughness of the films decreased with the increase in the CH_4 flow rate. The films' transmittance values increased with the CH_4 flow rate for the same coating thicknesses in the visible light range. Optical absorption studies indicated the band gap values increased from about (1.7 to 2.7 eV) with the increase in CH_4 flow rate [59].

In (2019), the amorphous and nanocrystalline SiC thin films were prepared by *Tehrani et al. They have used the hot-wire chemical vapor deposition and studied* their optical properties. Raman scattering spectroscopy, FTIR spectroscopy, and UV-Vis spectroscopy were used to investigate the film's change in structure and optical properties as a function of total gas partial pressure. The absorption coefficient, optical band gap, and refractive index of SiC films were determined. The results revealed that deposition pressure and total gas partial pressure have a substantial impact on the structure of the films and hence control their optical properties. The energy gap also showed a notable decrease from (2.5 eV to 1.6 eV) [60].

Mourya, et al. in (2019) have utilized the RF magnetron sputtering to deposit a nanocrystalline SiC thin layer on an anodized porous silicon substrate. Study of hydrogen gas (H_2) sensing characteristics of palladium-platinum (Pd-Pt) functionalized SiC thin film grown on a

porous Si substrate for high-temperature applications. The proposed device architecture (Pd-Pt/SiC/Psi) has several advantages, such as fast response/recovery time, extensive tunable detection range (5-500 ppm), stable high sensing response, high selectivity, wide operating temperature regime (25-500℃), good durability, and excellent reproducibility. The high response seen can be attributed to the combined impact of the bimetallic Pd-Pt layer's higher catalytic activity and the suggested sensor's increased surface area [61].

In (2020) the effect of SiC thin film thickness on the hydrogen sensing properties of Pd/SiC thin films has been studied by *Kumar, et al*. RF magnetron sputtering has been used to produce the Pd/SiC thin films on Si (100) substrates at (400℃) with deposition times ranging from 1 to 3 hours. FESEM cross-section views and XPS were used to determine the thickness of the Pd/SiC films and Pd capping layer, respectively. XRD and Raman spectroscopy indicate the growth of films. AFM was used to study the surface morphology of films, and all of the deposited films were found to be dense, evenly dispersed, and spherically shaped surface particles. At a working temperature of (250℃), the Pd/SiC thin-film sensor exhibits good sensitivity with a high response (17%) and response time (18 s) towards hydrogen gas (2 bar) [62].

Paneerselvam, et al. have used the pulsed laser deposition to produce SiC thin films on Si (100) substrates at an (800℃) substrate temperature in (2021). In addition, laser annealing of the post-deposited intrinsic amorphous SiC films was carried out in an Ar atmosphere using a Nd:YAG laser (355 nm). The crystalline features were seen in the laser-annealed samples. X-ray diffraction and Raman analyses were used to identify the crystalline properties of PLD generated, laser annealed samples. To further understand the process of laser aided annealing, a

numerical analysis was done on the SiC/Si contact to study the temperature distribution [63].

In (2021), *Mohsin, et al.* have used the pulsed laser deposition technique to prepare the SiC films on quartz and silicon substrates with Nd:YAG laser at two wavelengths (1064 nm and 532 nm). The structural, morphological, and optical properties of the deposited nanostructure SiC have been analyzed as a function of the wavelengths. The bandgap values of the deposited Nano SiC films increase as the laser wavelength increases and their values range from (2.94 eV to 3.14 eV). The produced SiC Nano-films have a grain size range of (36.34-48.75 nm) and a roughness of about (4.462 to 3.062 nm), according to SEM and AFM studies [64].

1.8 The aims of the study

The aims of this work are to:

1. Synthesis of the SiC:AgO thin films using pulsed laser deposition technique, and study the structural, optical and electrical properties of the as-deposited films.
2. Manufacturing and characterizing SiC:AgO thin films for solar cell applications.
3. Study the sensitivity, response time, and recovery time of as-deposited SiC:AgO thin films for gas sensing applications.

Chapter Two

Theoretical Part

2.1 Introduction

This chapter includes an explanation of the pulsed laser deposition technique and its advantages and the most important theoretical physical concepts and the mathematical relationships and laws that contribute directly or indirectly to the calculation and interpretation of the results obtained.

2.2 Mechanism of the Pulsed Laser Deposition (PLD)

The theory of pulsed laser deposition is a very complex physical phenomenon. It involves the physical process of the laser-material interaction, forming a plasma plume with highly energetic species, and transferring the ablated material through the plasma plume onto the heated substrate surface. Therefore, the thin-film formation process in PLD can be divided generally into the following four stages as shown in figure (2.1) [65-67]:

1. Laser radiation interaction with the target.
2. Dynamics of the ablated species.
3. Deposition of the ablated species on the substrate.
4. Nucleation and growth of thin films on the substrate surface.

Each stage of the PLD process is critical to creating a quality epitaxial crystalline, stoichiometric, uniform and smooth thin film [68].

In the first stage, the laser beam is focused onto the surface of the target. At sufficiently high flux densities and short pulse durations, all elements in the target are rapidly heated up to their evaporation temperature. Materials are dissociated from the target surface and ablated with the same stoichiometry as the target. The instantaneous ablation rate is highly dependent on the fluence of the laser shining on the target.

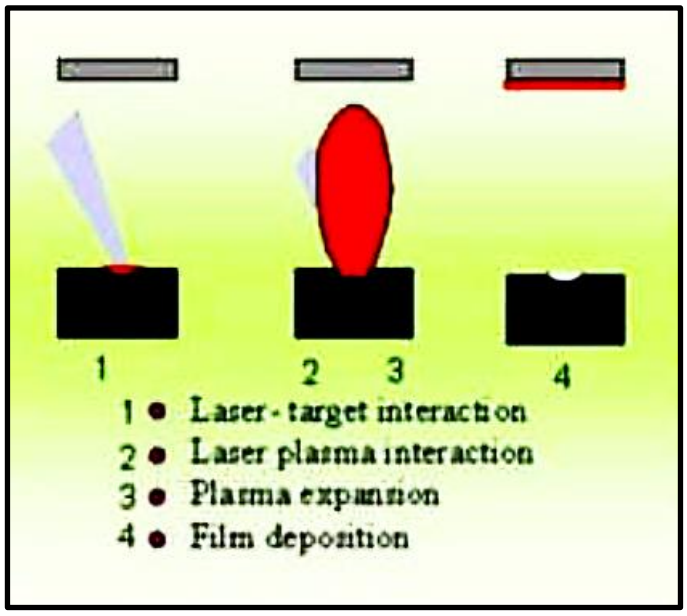

Figure (2.1): Interaction of a laser beam with matter [67].

The ablation mechanisms involve complex physical phenomena such as collisional, thermal, and electronic excitation, ablation and hydrodynamics. During the second stage, the emitted materials tend to move towards the substrate according to the laws of gas dynamics. The spot size of the laser and the plasma temperature significantly affect the uniformity of deposited films. Another parameter that governs the angular spread of ablated materials is the target-to-substrate distance [69, 70].

The third stage has a critical influence on the quality of thin film. The ejected high-energy species impinge onto the substrate surface and may induce various types of damage to the substrate. This energetic species sputters some surface atoms, forming a collision region between the incident flow and sputtered atoms. Films start growing after a thermalized area is formed, and the region serves as a source for the condensation of particles. When the condensation rate is higher than the rate of particles supplied by the sputtering, thermal equilibrium conditions can be reached quickly and the film grows on the substrate surface.

In the fourth stage, the nucleation and growth of crystalline films depend on many factors, such as the density, energy, ionization degree, and type of the condensing material, as well as the temperature and the physical-chemical properties of the substrate [71, 72].

The two main thermodynamic parameters for the growth mechanism are the substrate temperature (T_s) and the supersaturation (D_m). They are linked by the following equation [68]:

$$D_m = k_B T_s \ln\left(\frac{R_a}{R_e}\right) \quad (2.1)$$

Where k_B, R_a, R_e, and T_s are the Boltzmann constant, the actual deposition rate, the thin film deposition rate, and the substrate temperature, respectively.

The nucleation process depends on the interfacial energies between the three phases present-substrate, condensing material, and vapor. The minimum-energy shape of a nucleus is like a cap in which the critical size of the nucleus depends on the driving forces, i.e. the deposition rate and the substrate temperature. For the large nuclei (a case of small supersaturation), islands of the film are grown on the substrate which subsequently coalesces together. As the supersaturation increases, the critical nucleus shrinks until its height reaches an atomic diameter and its shape is that of a two-dimensional layer. For significant supersaturation, layer-by-layer nucleation will happen for incompletely wetted foreign substrates [72, 73].

The crystalline film growth depends on the surface mobility of the adatom (vapor atoms). The adatom will diffuse through several atomic distances before sticking to a stable position within the newly formed film. The surface temperature of the substrate determines the adatom's surface diffusion ability. High temperature favours rapid and defect-free crystal growth. In contrast, low temperature or considerable

supersaturation crystal growth may be overwhelmed by energetic particle impingement, resulting in disordered or amorphous structures [74].

The mean thickness of the growing film that reaches the state of continuity is given by the formula [68]:

$$N_{\text{th}} = A\,(\frac{1}{R})^{\frac{1}{3}}\;\; exp(\frac{-1}{T_s}) \qquad (2.2)$$

Where R is the deposition rate (supersaturation related) and T_s is the temperature of the substrate and A is a constant related to the materials.

In the PLD process, due to the short laser pulse duration (~10 ns) and hence the small temporal spread (<10 ms) of the ablated species, the deposition rate can be enormous. Consequently, layer-by-layer nucleation is favoured and ultra-thin and smooth films can be produced. In addition, the rapid deposition of the energetic ablation species helps to raise the substrate surface temperature. In this respect, PLD tends to demand a lower substrate temperature for crystalline film growth [71-73]. Figure (2.2) shows the pulsed laser deposition technique [75].

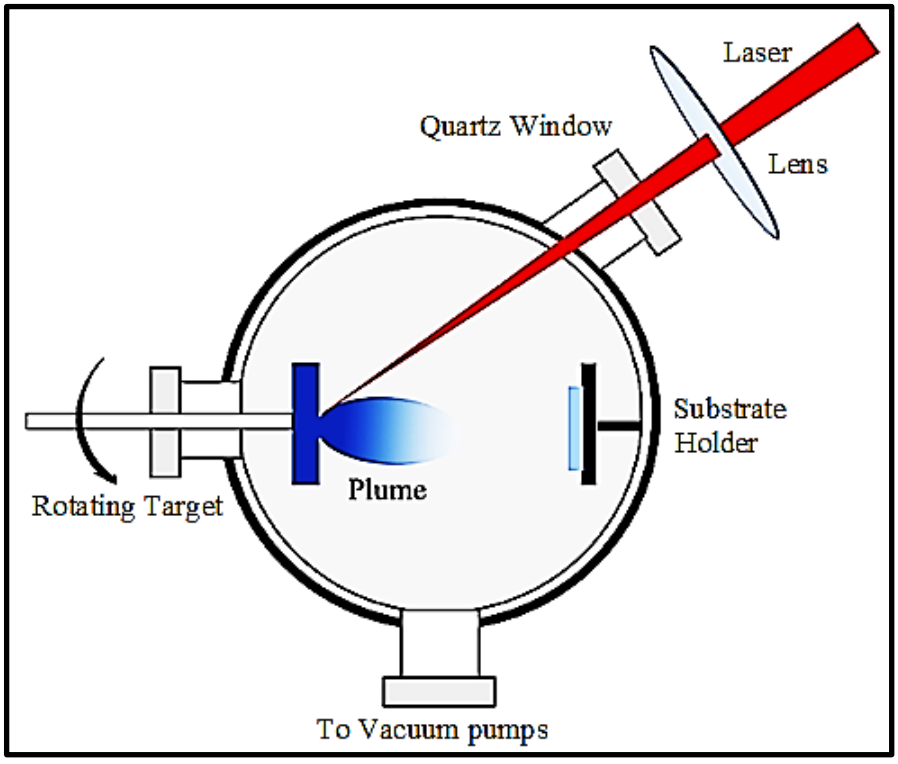

Figure (2.2): Schematic diagram of the pulsed laser deposition setup [75].

2.3 Laser-Target interaction

The plasma plume should have the same stoichiometry as the target to produce a film of the correct composition. For example, if the target surface was heated slowly by absorbing the light from a laser source, then this would allow a significant amount of the incident power to be conducted into the bulk of the target. The subsequent melting and evaporation of the surface would essentially be thermal, i.e. the difference between the melting points and vapor pressures of the target constituents would cause them to evaporate at different rates so that the composition of the evaporated material would change with time and would not represent that of the target. This incongruent evaporation leads to films with very different stoichiometry from the target [76]. To achieve congruent evaporation, the energy from the laser must be dumped into the target surface rapidly, to prevent a significant transport of heat into the subsurface material, so that the melting and vapor points of the target constituents are achieved nearly simultaneously. The high laser power density that this implies is most readily achieved with a pulsed or Q-switched source focused on a small spot on the target. If the energy density is below the ablation threshold for the material, then no material will be removed at all, although some elements may segregate to the surface [77, 78].

In general, the interaction between laser radiation and solid material occurs through the absorption of photons by electrons of the atomic system. The absorbed energy causes electrons to be in excited states with high energy, and as a result, the material heats up to very high temperatures in a short time. Then, the electron subsystem will transfer the energy to the lattice by the electron-phonon coupling [72, 76].

When the focused laser pulse arrives at the target surface the photons are absorbed by the surface and its temperature rises. The rate of surface

heating depends on many factors: most notably the actual volume of material being heated. This will depend not only upon how tightly the laser is focused but also on the optical penetration depth of the material. If this depth is small, the laser energy is absorbed within a much smaller volume. This implies the need for a wavelength for which the target is essentially opaque, and it is generally true that the absorption depth increases with wavelength. The rate of heating is determined by athermal diffusivity of the target and the laser pulse energy and duration [72].

In a high vacuum chamber, elementary or alloy targets are struck at an angle of (45^{o}) by a pulsed and focused laser beam. The atoms and ions ablated from the target are deposited on the substrate, which is mostly attached with the surface parallel to the target surface at a target-to-substrate distance of typically (2-10 cm). In the PLD technique, the target materials are first sputtered (or ablated) into a plasma plume by a focused laser beam at 45^{o}. The materials ablated then flow onto the substrate surface, on which the desired thin films are developed. Therefore, the interaction of intense laser matters plays an essential role in the PLD process **[**79-81**]**.

The incident laser pulse leads to highly rapid heating of the target material, and this may cause phase transition and introduce high amplitude stress in the solid target. The output of a pulsed laser is focused onto a target material maintained in a vacuum or with ambient gas. The target is usually rotated to avoid repeated ablation of the same spot on the target [72, 73].

2.4 Laser-Plasma interaction

In the description of the laser-plasma interaction, the laser pulse duration plays a crucial role. In the case of a nanosecond (*ns*) laser pulse, the forming plasma interacts with the laser beam whereas, in the case of

a femtosecond (*fs*) laser pulse, the previous mechanism doesn't occur. Because of the plasma formation in front of the target, the laser beam will be partially absorbed before it reaches the target, i.e. so-called (plasma shielding effect) which increases the plume ionization degree, and complicates the plume expansion mechanism. Due to the plasma-laser interaction, the evaporated material's temperatures increase rapidly to extremely high values and the electrons are further accelerated. The excited particles emit photons, leading to a bright plasma plume, which is characteristic of the laser ablation process [82].

The main absorption processes are the Inverse Bremsstrahlung (IB) and the direct single-photon processes, IB involves the absorption of photons by free electrons which are accelerated during the collision with neutral or ionized atoms. The cross-section for IB via electron-neutral collisions is much smaller than that of electron-ion collisions but can be important for the initial plume of weakly ionized gas. Initially, very few "seed" electrons may be present, produced by thermal emission from the solid or multi-photon ionization processes [83, 84].

2.5 Plasma plume expansion

The spatial structure of the vapor plasma at the early stage of its expansion is well known to be a cloud strongly forwarded in the normal direction to the ablated target. This featured plasma elliptic shape called a plume is a great difference in pressure gradients in axial and radial directions. Another essential characteristic of the ablation plume pertinent to PLD is the angular distribution of the ejected species in the plume, or simply the plume angular distribution [85, 86].

The plasma expands freely and adiabatically in a vacuum. In the case of vacuum, the plasma plume angular distribution is determined by the particles' colliding with each other. In the presence of the ambient gas, the plume's angular distribution is modified due to a collision between the

plume species and background gas atoms. These collisions scatter the plume particles from their original trajectories and broaden the angular distribution. It is generally expected that for a given background gas, these additional collisions will lead to a broader angular distribution of lighter plume species [87, 88].

Expansion of the plume in a vacuum is driven by the energy accumulated as thermal energy and energy stored as excitation and ionization in the initial layer. This energy is converted to the kinetic energy of the atoms in the plume, and eventually, all atoms will move with an asymptotic, constant velocity distribution [89, 90].

Figure (2.3) shows the plasma plume in an ablation process [91].

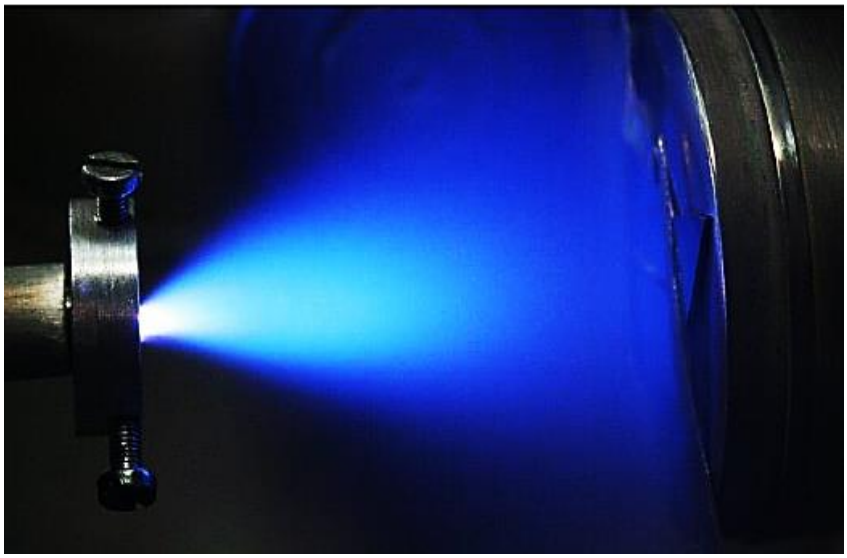

Figure (2.3): Image of a plasma plume generated by the PLD process [91].

2.6 Advantages of the PLD Technique

It is preferable to use lasers in preparing thin films for several reasons, which are [92, 93]:

1. To obtain high-purity thin films.
2. The heating is limited to a specific area of the material and it is not necessary to heat it all.
3. High deposition rates as well as the possibility of obtaining films of different thicknesses by controlling the number of pulses.

4. In laser deposition, crystalline films predominate.
5. The possibility of depositing materials with a high melting point.
6. Easy to manufacture system.
7. The possibility of evaporating more than one substance without the need to break the vacuum.

2.7 Limitations of the PLD Technique

However, despite its simplicity and versatility, the PLD technique also suffers from some limitations. Most notably, the seven main limitations of PLD are [93]:

1. Substrate heating and post-annealing are often needed for depositing high-quality films.
2. It is difficult to use heat-sensitive substrates, e.g. plastics.
3. PLD control parameters such as laser energy, wavelength, and gas pressure are not independent, i.e. not ideal for controlling the process.
4. Creation of particulates in the plasma plume can end up incorporated in the thin film, leading to low-quality films. During the deposition process, the size of the particulates ranges from < 0.1 μm to 10 μm, and depends strongly on the laser energy and wavelength used.
5. It is possible to create asymmetrical fragmented particulates from the target that will affect the uniformity of the film.
6. If the laser energy is too high, there will be heating and melting of the sub-surface, leading to the formation of molten droplets in the sub-surface, which leads to splashing of the target material. These macroscopic droplets will be incorporated into the deposited film, leading to a non-uniform film.
7. The average kinetic energy of the plume particles is relatively high. Therefore, it is expected that the interface and the crystalline quality of the deposited structures might suffer.

2.8 Semiconductors

A semiconductor is a material whose conductivity lies between conductors and insulators. The conductivity of semiconductors is generally sensitive to temperature, illumination and magnetic field, and this sensitivity in conductivity makes the semiconductor one of the most important materials for electronic applications. The structure of semiconductors can be classified according to the arrangement of their atoms into crystalline and amorphous semiconductors [94, 95].

2.8.1 Crystalline Semiconductors

A crystalline semiconductor is made up of a three-dimensional arrangement of atoms in a regular, definite and long-range order. They have a homogeneous composition with a characteristic geometrical shape. They are generally anisotropic, i.e. their properties such as refractive index, electrical conductivity, and permittivity vary with direction. There are two types of the ordered array of atoms in crystalline semiconductors [96, 97]:

A. Monocrystalline Semiconductors

There is a periodicity to the lattice that extends right through the material in this type. Therefore, these materials have a high degree of ordering and therefore, they have long-range order in three dimensions [94, 98], as shown in figure (2.4.a) [99].

B. Polycrystalline Semiconductors

This structure consists of many tiny single crystals known as grains or crystallites which are separated by grain boundaries each of which contains a periodic array of atoms and is considered to pass long-range order, while the grains in the polycrystalline state possess short-range

order with random grain sites [94, 96], shape and orientation packing as shown in figure (2.4.b).

2.8.2 Amorphous Semiconductors

The atoms are arranged in an irregular and short-range order. They are not homogeneous in composition. They are isotropic. They do not have a sharp melting point. The arrangement of atoms in these materials is not entirely random, but their periodicity is absent in three dimensions. They have been ordered only within a few atomic or molecular dimensions [94, 97], as shown in figure (2.4.c).

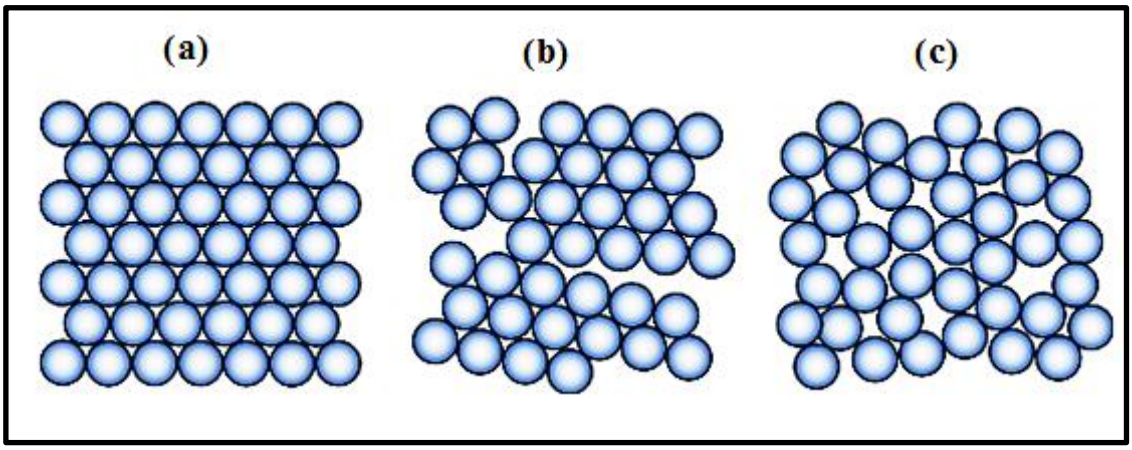

Figure (2.4): Schematics of three general types of structures [99].
(a) Monocrystalline (b) Polycrystalline (c) Amorphous

2.9 Intrinsic and Extrinsic Semiconductors

An intrinsic semiconductor crystal with no impurities or lattice defects is a perfect semiconductor. There are no charge carriers in such material at (0 K) since the valence band is filled with electrons and the conduction band is empty.

In addition to the intrinsic carriers generated thermally, it is possible to create carriers in semiconductors by purposely introducing impurities into the crystal. This process, called "doping", is the most common technique for varying the conductivity of semiconductors. By doping, a crystal can be altered to have a predominance of either electrons or holes.

Thus there are two types of doped semiconductors, n-type and p-type as shown in figure (2.5) [100]. When a crystal is doped such that the equilibrium carrier concentrations n_o and p_o are different from the intrinsic carrier concentration n_i, the material is said to be extrinsic. These (intrinsic and extrinsic) behaviours are essential to the operation of microelectronic devices [101].

When the level is filled with electrons at (0 K), just a little amount of thermal energy is required to excite these electrons to the conduction band. Thus at about (50-100 K), virtually all of the electrons in the impurity level are donated to the conduction band. Such an impurity level is called a donor level, and the impurities in this state are called donor impurities.

When the atoms introduce impurity levels near the valence band where these levels are empty of electrons at (0 K). At low temperatures, enough thermal energy is available to excite electrons from the valence band into the impurity level, leaving behind holes in the valence band. Such an impurity level is called an acceptor level, and the impurities in this state are called acceptor impurities [102].

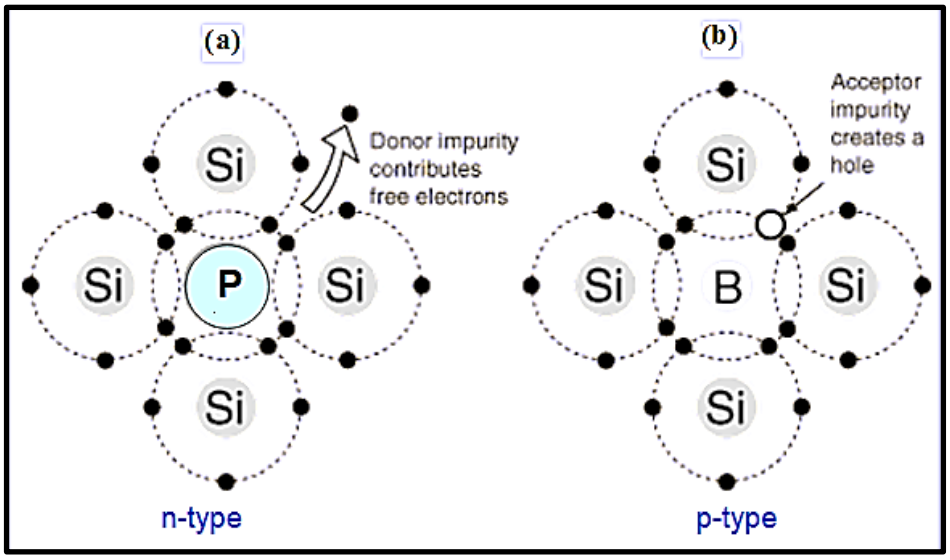

Figure (2.5): Extrinsic semiconductors (a) n-type and (b) p-type [100].

Figure (2.5.a) represents the extrinsic n-type semiconductor model. An impurity atom such as phosphorus, having five valence electrons, may substitute for a silicon atom. Those results are shown an extra bonding electron, which is bound to the impurity atom and orbits it. Figure (2.5.b) shows the extrinsic p-type semiconductor model. An impurity atom such as a boron, having three valence electrons, may substitute for a silicon atom. Those results are shown a deficiency of one valence electron or a hole associated with the impurity atom [100].

2.10 Structure Properties

The structure properties represent a critical tool for studying the crystallographic structure of the thin films as types of crystal, the nature of the film and other parameters.

2.10.1 X-Ray Diffraction (XRD)

X-ray diffraction is used to study the structural properties that define the preferred orientation of the crystal and phase composition. One can calculate different parameters such as lattice parameters, average grain size, lattice strain, residual stress, etc. The spacing between diffracting planes d shown in the figure (2.6) is determined using Bragg's law [103- 105]:

$$n\lambda = 2d_{hkl}\ sin\,\theta \qquad (2.3)$$

Where *n* is the order of reflection, which may be any integer (1, 2, 3, . . .) is a positive integer, λ is the wavelength of the X-ray, and *h*, *k*, and ℓ are the Miller indices of the Bragg plane and θ is the incident angle. Bragg's law can be used to obtain the lattice constants of a particular cubic system through the following relation [103- 105]:

$$d_{hkl} = \frac{a}{\sqrt{h^2 + k^2 + l^2}} \qquad (2.4)$$

Where *a* is the lattice spacing of the cubic crystal.

In the hexagonal crystal system, the interplanar spacing equation naturally involves both *a* and *c* since these are not generally equal [103- 105]:

$$d_{hkl} = \frac{4}{3}\left(\frac{h^2+hk+k^2}{a^2} + \frac{l^2}{c^2}\right) \quad (2.5)$$

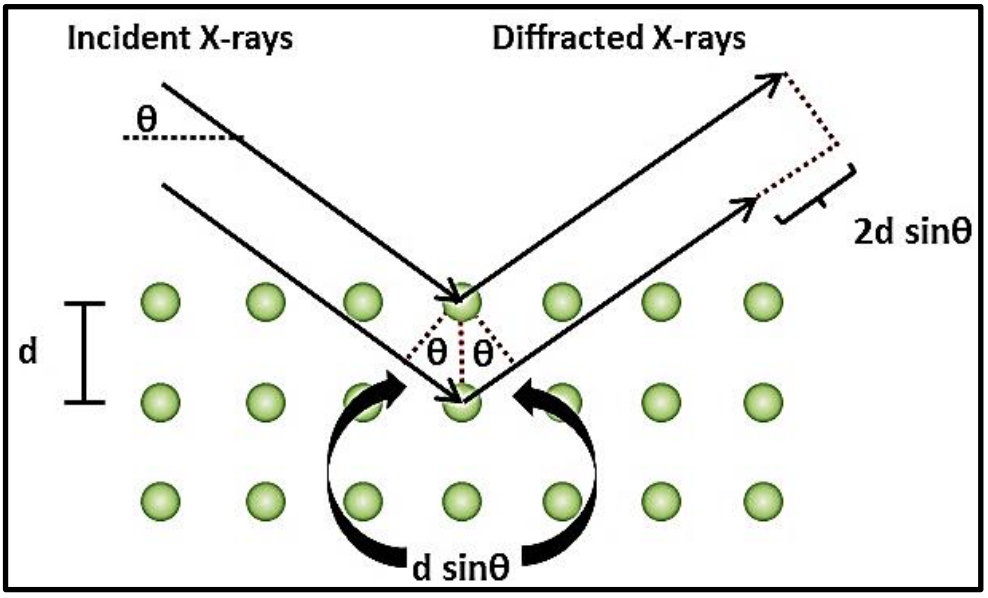

Figure (2.6): Bragg Diffraction [105].

2.10.2 Structure Parameters

2.10.2.1 Full Width at Half Maximum (FWHM)

FWHM of the peak (preferred orientation) could be measured from the width of the peak (in radian unit) at half of the maximum intensity.

2.10.2.2 Average Crystallite Size (D)

The average crystallite size of thin films can be calculated by Scherer's formula [102, 106, and 107]:

$$D = \frac{k\lambda}{\beta \cos\theta} \quad (2.6)$$

Where k is shape factory and β is full width at half maximum (FWHM).

2.10.2.3 Dislocation Density (δ)

It is the total dislocation length per unit area of a random section [106, 108]. δ can be calculated using the following relation [109]:

$$\delta = \frac{1}{D^2} \tag{2.7}$$

δ is measured in units of $(lines/m^2)$.

2.10.2.4 Micro Strains (ε)

The value of strain can be calculated through the following equation [109, 110]:

$$\varepsilon = \frac{\beta \cos\theta}{4} \tag{2.8}$$

2.11 Field Emission Scanning Electron Microscope (FESEM)

A field emission scanning electron microscope examines and analyses the micro-and nanostructured surface morphology. The method is similar to that of a scanning electron microscope (SEM); however, there is a difference in the electron gun used to scan the specimen. In FESEM, a field emission gun is used instead of typical electron gun sources, which provides a sharply pointed beam with high electron energy, resulting in minimized charging effects on the specimen and enhancement of the spatial resolution. An image in FESEM is generated when the electron beam from the field emission gun through the column of an electromagnetic lens impinges the specimen surface. At that time, complex interactions occur on the surface and at a certain depth below the surface of the specimen, resulting in various emissions from the specimen. The interactions between the electron beam and the atom-shell produce an X-ray. EDX detects and analyzes this X-ray emission by the energy identification of elements. Figure (2.7) shows the schematic diagram of FESEM. [111-113].

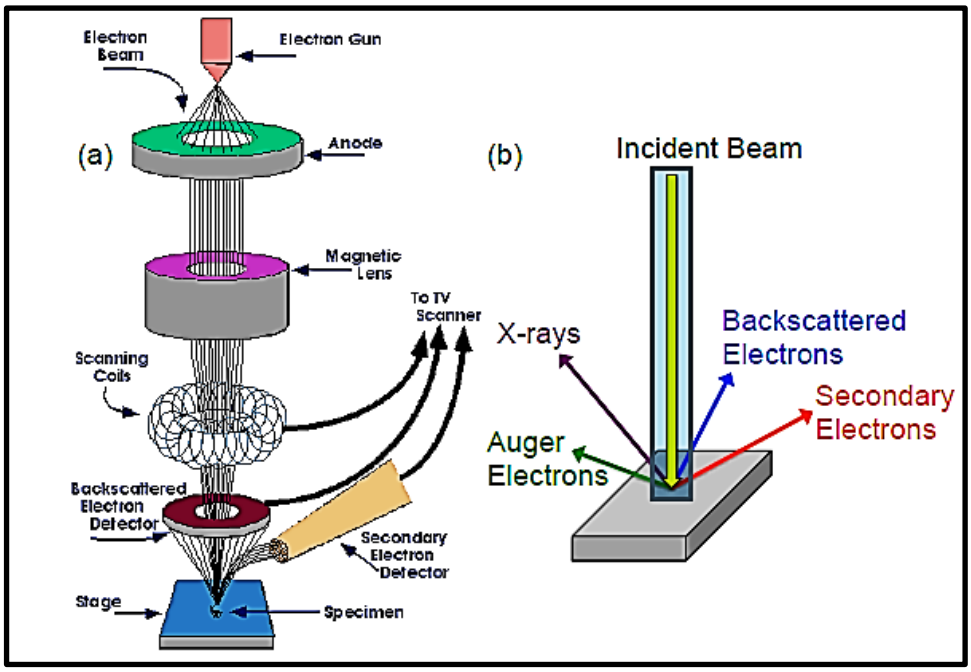

Figure (2.7): Schematic diagram of an FESEM [112].

2.12 Atomic Force Microscope (AFM)

An atomic force microscope (AFM) is one of the most widely used tools for imaging, measuring, and manipulating samples at the nanoscale. No special sample preparation is needed for this technique, and the measurements are allotted to a close ambient environment. Like all other scanning probe microscopes, it utilizes a sharp probe moving over the surface of a sample in a raster scan as shown in figure (2.8). In the case of the AFM, the probe is a tip on the end of a cantilever that bends in response to the force between the tip and the sample. The three basic concepts that one must be familiar with to understand the operation of an AFM are piezoelectric transducers (in AFM, often known as piezoelectric scanners), force transducers (force sensors), and feedback control. The piezoelectric transducer moves the tip over the sample surface, the force transducer senses the force between the tip and the surface, and the feedback control feeds the signal from the force transducer back into the piezoelectric to maintain a fixed force between the tip and the sample [113-115].

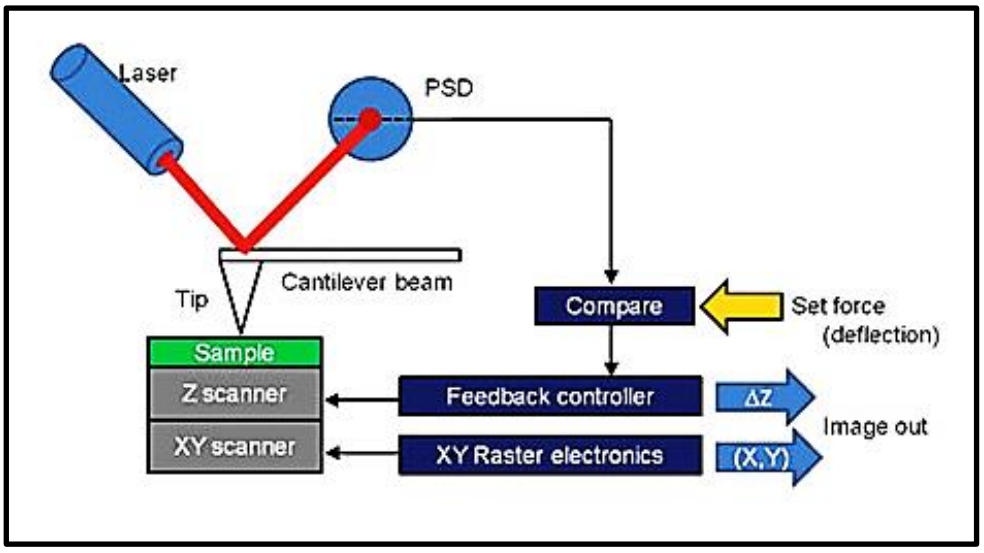

Figure (2.8): Block diagram of an atomic-force microscope using beam deflection detection [114].

2.13 Optical Properties

A solid's optical properties can be determined by applying a monochromatic light onto the sample and then measuring the transmitted or reflected beam from the sample as a function of incident photon energy [106, 116].

When photons are incident on a semiconductor, they may propagate or absorbed, depending on the bandgap energy (E_g) and on the photon energy ($h\nu$), where h is Plank's constant and ν is the incident photon frequency. The photons are not readily absorbed if ($h\nu < E_g$), the light will pass through the semiconductor and the semiconductor looks to be transparent. If the ($h\nu \geq E_g$), the photons can interact with a valence band electrons and rise up the electrons to the conduction band. The conduction band contains many empty levels and the valence band contains many electrons, so this interaction is highly likely when ($h\nu > E_g$). The interaction creates a hole in the valence band and an electron in the conduction band. This phenomenon is called (the electron-hole pair production). When ($h\nu > E_g$) an electron-hole pair is created and the additional energy may give the hole or electron extra kinetic energy, which will be dissipated in the semiconductor as heat figure [116, 117].

2.13.1 Absorptance (A)

Absorption is defined as a ratio between the intensity of absorbed light by material (I_A) and the incident light intensity (I_o) [118]:

$$A = \frac{I_A}{I_o} \tag{2.9}$$

2.13.2 Transmittance (T)

Transmittance is given by the ratio between the transmitting rays (I_T) intensity through the film to the incident rays intensity (I_o) on it as the relationship below [118, 119]:

$$T = \frac{I_T}{I_o} \tag{2.10}$$

Also can find a transmittance as a function of wavelength through the exponential relationship for both transmittance and absorbance which [118, 119]:

$$T = 10^{-A} \tag{2.11}$$

2.13.3 Reflectance (R)

The below relation may be used to calculate reflectance from transmission spectrum and absorption in line with the law of conservation of energy [120, 121]:

$$R + T + A = 1 \tag{2.12}$$

2.13.4 Optical Absorption and Absorption Edge

The fundamental absorption is the most important absorption process that involves the transition of electrons from the valence band (V.B) to the conduction band (C.B), which manifests itself by a rapid rise in absorption, and this can be used to determine the energy gap of the semiconductor. The semiconductor absorbs a photon from the incident beam, the absorption depends on the photon energy, the absorption associated with the electronic transition between the (V. B) and the (C. B)

in the material starting at the absorption edge which corresponds to minimum energy difference (E_g^{opt}) between the lowest minimum of the (C. B) and the highest maximum of the (V. B) [106, 122]. If the photon energy is equal to or more than the energy gap (E_g^{opt}) then, the photon can interact with a valence electron, elevates the electron into the (C. B) and creates an electron-hole pair. The maximum wavelength (λ_{max}) of the incident photon which creates the electron-hole pair is defined as [123, 124].

$$\lambda_{max}\,(\text{nm}) = \frac{hc}{E_g} = \frac{1240}{E_g(\text{eV})} \qquad (2.13)$$

Where c is the light speed in a vacuum.

The intensity of the photon flux decreases exponentially with distance through the semiconductor according to the following equation [106, 116, and 117].

$$I = I_o\, exp(-\alpha t) \qquad (2.14)$$

Where I_o and I are the incident and the transmitted photon intensity respectively, α is the absorption coefficient and t is the thickness of the material.

2.13.5 Absorption Regions

There are three absorption regions as shown in figure (2.9) [125]:

A. High absorption region

In this region, the value of absorption coefficient (α) is about (10^4 cm^{-1}) or more. This region is shown in figure (2.9) part (A), from this region, the absorption edge can be concluded [106, 117, and 126].

B. Exponential absorption

The value of absorption coefficient (α) is in the range of ($1\ cm^{-1} < \alpha < 10^4\ cm^{-1}$), and indicates to transition between the spread

level from the valence band to the local level in the conduction band. This region is shown in figure (2.9) part (B) [106, 117, and 126].

C. Low absorption region

In this region, the absorption coefficient (α) is very small ($\alpha < 1$ cm^{-1}), the transitions are happening here between tails inside the forbidden gap (E_g) as shown in part (C) of the figure (2.9) [106, 117, and 126].

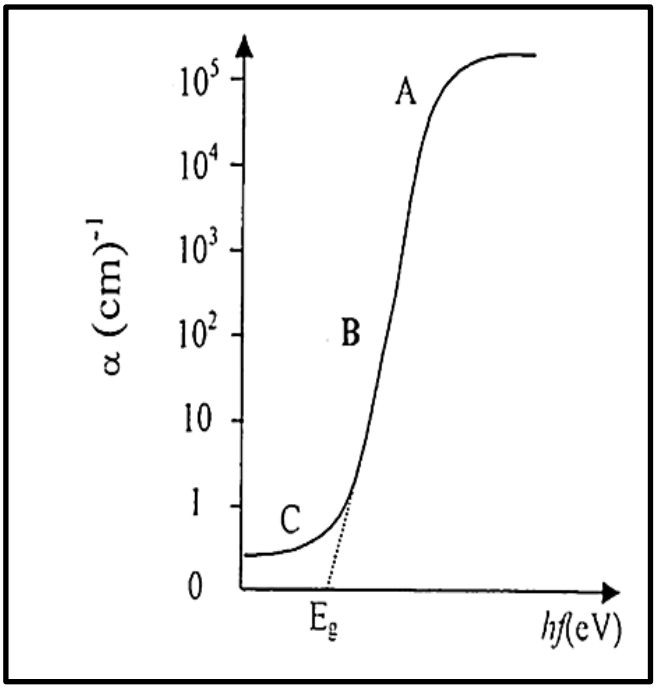

Figure (2.9): The main regions of the optical absorption [126].

2.14 Electronic Transitions in Semiconductors

When an electron makes the smallest-energy transition from the conduction band to the valence band can do so without a change in the k value; on the other hand, a transition from the minimum point in the conduction band to the maximum point of the valence band requires some change in k. Thus, two classes of semiconductor energy bands are direct and indirect, as shown in figure (2.10) [127]. It can be seen that an indirect transition involving a change in k requires a shift in the momentum of the electron [128, 129].

2.14.1 Direct Transitions

The direct transition, in general, occurs between the top of the valence band and the bottom of the conduction band (vertical transition) at the same wave vector ($\overrightarrow{\Delta k} = 0$) for conservation of momentum. The allowed direct transition refers to that transition which occurs between the top of the valence band and the bottom of the conduction band when the change in the wave vector is equal to zero ($\overrightarrow{\Delta k} = 0$), as shown in figure (2.10.a). This transition is described by the following relation [129-133]:

$$\alpha h\nu = B\,(h\nu - E_g^{opt})^{1/2} \qquad (2.15)$$

Where B is a parameter inversely proportional to the amourphosity (depending on the material). If the transition occurs between states of the same wave vector, but the wave vector does not equal zero, the transition is called forbidden direct transition as shown in figure (2.10.b), it obeys the following relation [129-134].

$$\alpha h\nu = B\,(h\nu - E_g^{opt})^{3/2} \qquad (2.16)$$

2.14.2 Indirect Transitions

In indirect transition, there is a significant momentum difference between the points to which the transition takes place in valence and conduction bands. This means that the conduction band minima are not at the same value of k as the valence band maxima, then, the assistance of a phonon is necessary to conserve the momentum, therefore [122, 135]:

$$h\nu = E_g \pm E_P \qquad (2.17)$$

Where E_P is the energy of an absorbed or emitted phonon.

For an allowed indirect transition shown in figure (2.10.c), the transition occurs from the top of the valence band to the bottom of the conduction band and is given in the following relation [129-133].

$$\alpha h\nu = B\,(h\nu - E_g^{opt})^{2} \qquad (2.18)$$

While, the forbidden indirect transitions occur from any point near the top of (V.B) to any point other than the bottom of the (C.B), as shown in figure (2.10.d), this transition is given by the below relation [129-133].

$$\alpha h\nu = B\,(h\nu - E_g^{opt})^3 \qquad (2.19)$$

Experimentally, it is possible to differentiate between direct and indirect processes by the level of the absorption coefficient (α); α which takes values from (10^4 cm^{-1} to 10^5 cm^{-1}) for direct transitions and (10 cm^{-1} to 10^3 cm^{-1}) for indirect transitions at the absorption edge [123].

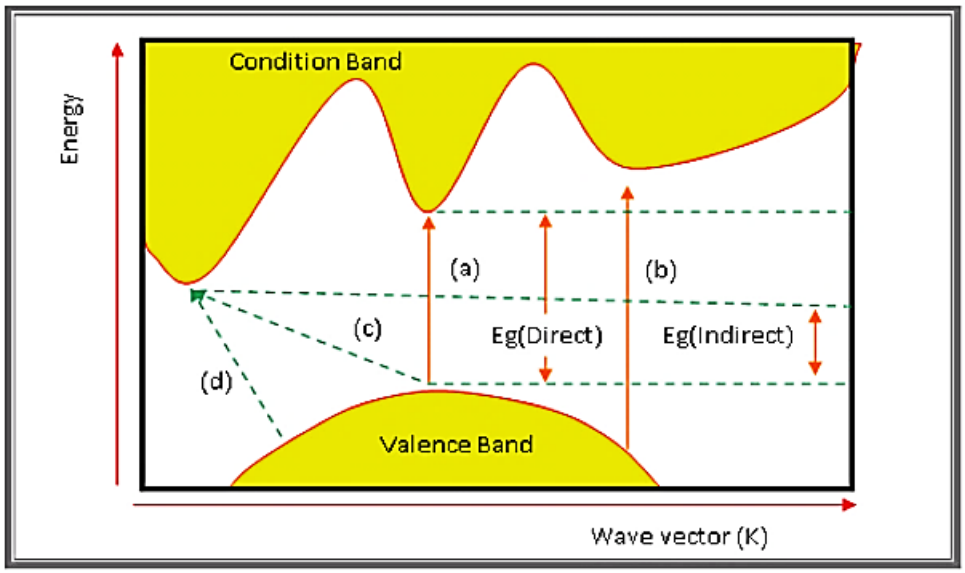

Figure (2.10): The optical transitions [127].
(a) Allowed direct, (b) Forbidden direct, (c) Allowed indirect, (d) Forbidden indirect

2.15 Optical constants

The optical constants are fundamental parameters because they describe the optical behavior of the materials. The absorption coefficient of the material is a powerful function of the photon energy and bandgap energy. The absorption coefficient represents the attenuation that occurs in incident photon energy on the material for unit thickness. The main reason for this is attributed to the absorption processes [128, 136, and 137]. In addition to the absorption coefficient, optical constants included refractive index (n) and extinction coefficient (k_o).

2.15.1 Absorption Coefficient (α)

The absorption coefficient is the percentage of the decrease in radiation energy flux relative to the distance unit along the direction of wave propagation. It depends on the incident photons' energy, properties of the semiconductor (energy gap), and the type of electronic transitions between energy bands. (α) is given by [138, 139]:

$$\alpha = 2.303 \frac{A}{t} \quad (2.20)$$

Where A is the absorbance and t is the sample thickness.

2.15.2 Extinction Coefficient (k_o)

The extinction coefficient is the amount of attenuation in the intensity of electromagnetic radiation due to interaction with film material particles. i.e. represents the amount of absorbed energy in the thin film [113]. It is related to the absorption coefficient according to the following relationship [138, 139]:

$$k_o = \frac{\alpha\lambda}{4\pi} \quad (2.21)$$

Where λ is the wavelength of the incident radiation.

2.15.3 Refractive Index (n)

The ratio between the velocity of light in a vacuum to its velocity in the medium, the complex refractive index (n_c) is defined as [130, 138]:

$$n_c = n - ik_o \quad (2.22)$$

It is related to the velocity of propagation (v), and light velocity (c) by:

$$v = \frac{c}{n_c} \quad (2.23)$$

The refractive index can be calculated by the formula [138]:

$$n = \left[\left(\frac{1+R}{1-R}\right)^2 - (k_0^2 + 1)\right]^{\frac{1}{2}} + \frac{1+R}{1-R} \quad (2.24)$$

Where R is the reflectance and can be expressed by the relation [136, 138]:

$$R = \frac{(n-1)^2 + {k_o}^2}{(n+1)^2 + {k_o}^2} \quad (2.25)$$

2.16 Electrical properties

Consideration of the electrical properties of materials is often important when materials selection and processing decisions are being made during the design of a component or structure. This section will discuss some electrical properties of semiconductors such as the Hall effect [94, 95].

2.16.1 Hall Effect

The Hall effect is used to measure the semiconductor carrier concentration and mobility which is used to detect whether a semiconductor is n or p-type. When a constant current (I) below comes along the x-axis from right to left in the presence of magnetic field (B) at the z-axis with value (0.55T), the electron obeys Lorentz force in the beginning, and they drift toward the negative the y-axis, and thus the sample surface charge too much and causing a transverse voltage. The transverse voltage is Hall voltage (V_H) known as shown in figure (2.11). The Hall coefficient (R_H) can be determined by measuring the Hall voltage (V_H) that produces venues across the field across the sample of a thickness (t) by [141, 142]:

$$R_H = \frac{V_H}{I} \cdot \frac{t}{B} \quad (2.26)$$

From the Hall coefficient equation, the semiconductor carrier concentration can be determined as given in the following [141, 142]:

$$R_H = \frac{1}{p.e} \quad \text{(For p-type)} \quad (2.27)$$

$$R_H = \frac{-1}{n.e} \quad \text{(For n-type)} \quad (2.28)$$

Where (p and n) are the carrier concentrations of holes and electrons, respectively, and (e) is the electron's charge. If the conduction is due to one carrier type e.g. holes [141, 142]:

$$\sigma_p = en\mu_p \qquad \text{(For p-type)} \qquad (2.29)$$

And for electrons:

$$\sigma_n = en\mu_n \qquad \text{(For n-type)} \qquad (2.30)$$

Where μ_p is the mobility for holes and μ_n is the mobility for electrons.

The Hall mobility μ_H can be measured as [141, 142]:

$$\mu_H = \frac{\sigma}{n.e} \qquad (2.31)$$

The Hall mobility is defined as the product of the Hall coefficient and conductivity as in the following relation [141, 143]:

$$\mu_H = \sigma \, R_H \qquad (2.32)$$

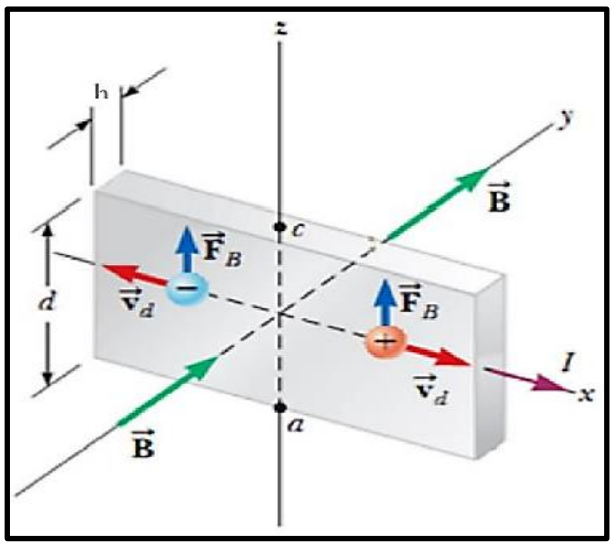

Figure (2.11): Diagram for Hall Effect [141, 142].

2.17 Heterojunctions

The heterojunction is defined as a connection between two semiconductor materials that differ in the energy gap, electronic affinity, dielectric constant, and work function as well as a mismatch in the lattice constant for the two materials, while the homojunction consists of the connection of two semiconductor materials of the same type, i.e. identical

in the energy gap, electronic affinity, dielectric constant, the work function and the lattice constant. [100, 143].

Heterojunctions are classified into sudden heterojunctions and graded heterojunctions and sub-classified as different connection points on both sides of the divide. The semiconductor has the same name as the connection-symmetric uniform combination (heterojunctions isotype) such as (p-p), (n-n), otherwise a different combination of asymmetric (Anisotype heterojunctions) such as called (n-p), (p-n) [144].

Heterojunctions have unique electrical and optical properties and can be divided into three classes [145, 146]:

1. The first class is between two different semiconductor wafers, such as PZT and Si.
2. The second class is between metals and semiconductors, the ohmic connection such as Al and PZT.
3. The third class is between the phase semiconductor crystal with the same type of semiconductor random phase, such as c-Si with a-Si.

2.18 Solar Cells

A solar cell is a (p-n) junction device that converts the incident sunlight to electrical power without applied voltage (photovoltaic PV mode) and pollution and noise. When the light ($hv > E_g$) strikes the cell, the electron-hole pairs will be created in the space charge region. Electrons in the conduction band and holes in the valence band can contribute to produce the current under the electrical field which sweeps out and produces the photocurrent (I_{Ph}) in the reverse bias direction as shown in figure (2.12). Short circuit current (I_{sc}) and the open circuit voltage (V_{oc}) are very important parameters that characterize the performance of a solar cell [147, 148].

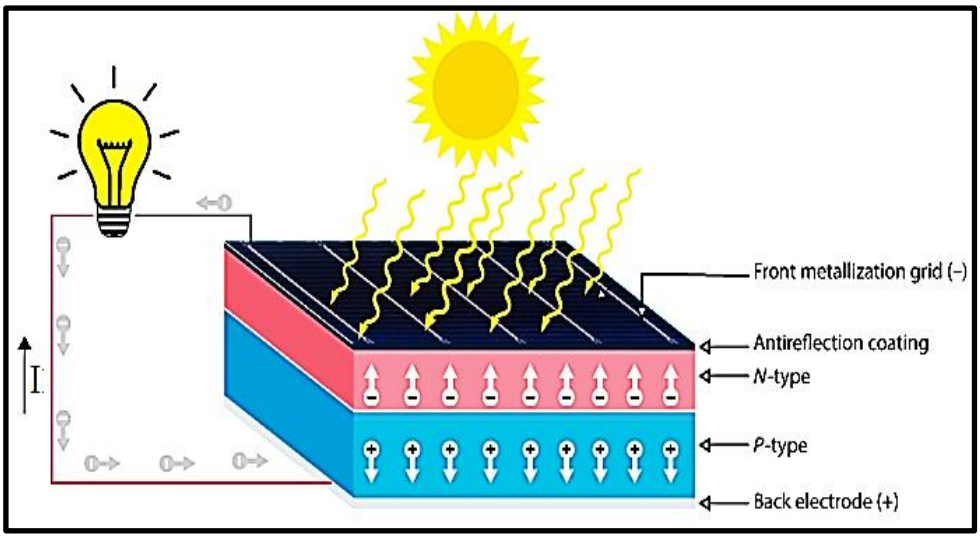

Figure (2.12): Operation of a solar cell [148].

2.18.1 I-V Characteristics of Solar Cell

The I-V curve of solar cells describes the current and voltage characteristics of a specific photovoltaic (PV) cell. It gives a detailed description of its solar energy conversion ability and efficiency. Knowing the electrical I-V characteristics of a solar cell is critical in determining the device's output performance and solar efficiency.

The main electrical characteristics of a PV cell are summarized in the relationship between the current and voltage produced on a typical solar cell I-V characteristics curve. The intensity of the solar radiation that hits the cell controls the current, while the increases in the temperature of the solar cell reduce its voltage [149, 150].

The I-V curve of a solar cell is the superposition of the I-V curve of the solar cell diode in the dark with the light-generated current. The light has the effect of shifting the I-V curve down into the fourth quadrant where power can be extracted from the diode. Illuminating a cell adds to the normal "dark" currents in the diode so that the diode law becomes [149, 150]:

$$I = I_0 [exp(qV/nkT) - 1] - I_L \quad (2.33)$$

Where n is the ideality factor and I_L is the light generated current.

Figure (2.13) represents the I-V curve of the solar cell in the dark and under light [151].

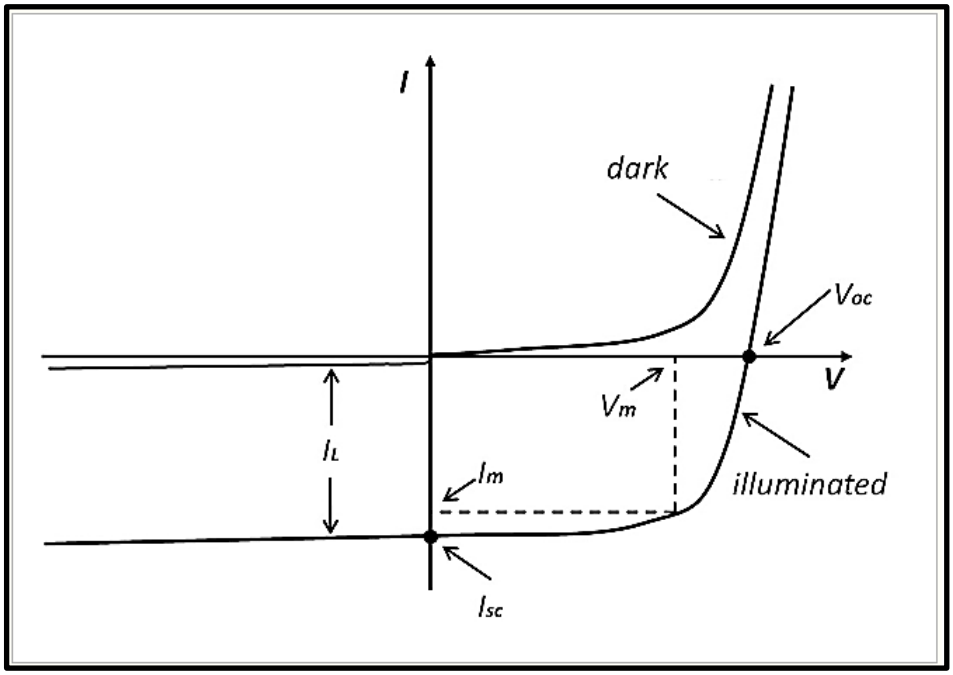

Figure (2.13): The I-V curve of the solar cell in a dark and under light [151].

2.18.2 Solar Cell Circuit and Device Parameters

A photovoltaic cell may be represented by the equivalent circuit model shown in figure (2.14) [152]. This model consists of current due to optical generation (I_L), a diode that generates a current, a series resistance (R_s), and shunt resistance (R_{sh}). The series resistance is due to the resistance of the metal contacts, ohmic losses in the front surface of the cell, impurity concentrations, and junction depth. The series resistance is an important parameter because it reduces both the short-circuit current and the maximum power output of the cell. Ideally, the series resistance should be ($R_s = 0$). The shunt resistance represents the loss due to surface leakage along the edge of the cell or due to crystal defects. Ideally, the shunt resistance should be infinite ($R_{sh} = \infty$) [148, 153].

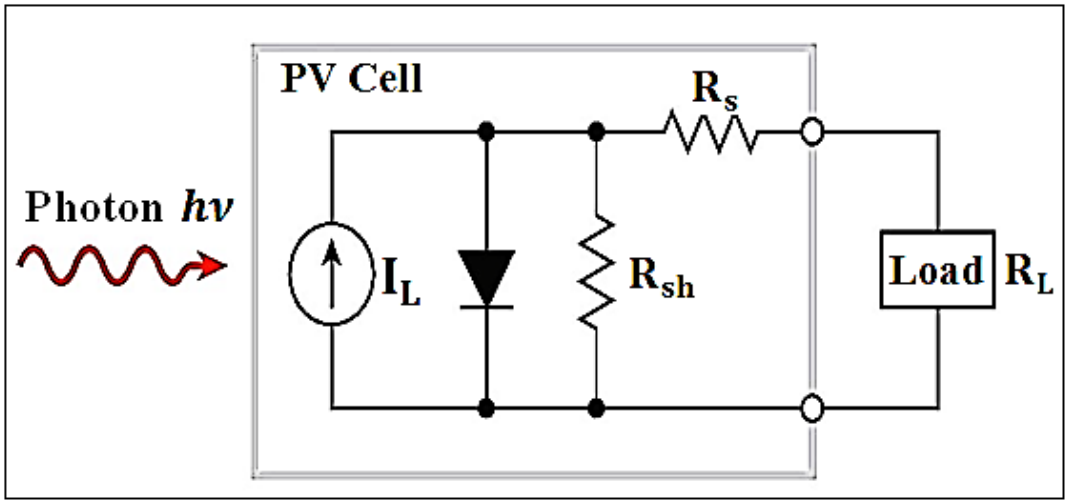

Figure (2.14): Idealized equivalent circuit of a photovoltaic cell [152]

There are several parameters are used to characterize solar cells.

1. **Open circuit voltage (V_{oc})**: It is the maximum voltage produced by a solar cell (the resistance reaches infinity) and the net current is zero and given by the following equation [142, 153]:

$$V_{oc} = \frac{nk_BT}{q} \ln\left(\frac{I_{sc}}{I_0} + 1\right) \quad (2.34)$$

Where T is the temperature, q is the electron charge, and I_o is the reverse saturation current or the dark current.

2. **Short circuit current (I_{sc})**: The current that flows through the solar cell when it is short-circuited (the resistance of load is zero) which leads to (V = 0 volt) and given by the following relation [147, 153]:

$$I_{sc} = I_s\,[exp(qV_{oc}/kT) - 1] + V_{oc}/R_{sh} \quad (2\text{-}35)$$

Where R_{sh} is the shunt resistance.

The short-circuit current depends on a number of factors such as the solar cell area, the number of photons, the spectrum of the incident light, and the optical properties (absorption and reflection) of the solar cell.

3. **Fill factor (FF):** The fill factor measures how far the I-V characteristics of an actual PV cell differ from those of an ideal cell. The fill factor is given by the relation [149-151]:

$$F.F = \frac{I_m V_m}{I_{sc} V_{oc}} \quad (2.36)$$

4. **Conversion efficiency** (η): is a measure of the amount of light energy that is converted into electrical energy and is given by[149-151]:

$$\eta = \frac{P_m}{P_{in}} x\ 100\ \% = \frac{I_m V_m}{P_{in}} x\ 100\ \% \quad (2.37)$$

Where P_m is the maximum power output and P_{in} is the power input to the cell defined as the total radiant energy incident on the cell's surface.

2.19 Semiconductor Gas Sensor Principles

A gas sensor can be defined as a device that informs about the composition of its ambient atmosphere. Remarkably, upon interaction with chemical species (absorption, chemical reaction, and charge transfer), the physicochemical properties of the metal oxide sensitive layer (such as its mass, temperature, and electrical resistance) reversibly change. These changes are translated into an electrical signal such as frequency, current, voltage, or conductance, which is then read out and subjected to further data treatment and processing. Many metal oxides are suitable for detecting explosive, reducing, or oxidizing gases by varying electric conductivity measurements [154, 155].

2.19.1 Thin Film Resistive Gas Sensors

Resistive sensors were utilized to measure a wide range of physical and chemical properties, which can be considered the most familiar and low-cost sensors. The photo-resistive sensors, exhibit changes in conductivity when exposing to light absorption; thermo-resistive sensors have changes in resistivity which is governed by temperature; piezo-resistive sensors, measure the change in resistance as a function of mechanical stress; whereas magneto resistive sensors alter the resistivity according to an external magnetic field and chemo resistive sensor that

alters the resistivity generated from chemical element and the sensing material interaction. The most suitable material for sensing in gas sensing is metal oxides of the chemo resistive type. This knowledge was applied to gas detection applications [156].

2.19.2 Chemical Sensors

Chemical sensors are devices utilized for the fixed chemical properties of materials. The main concept of chemical sensing is the gas or vapor interaction with the oxygen vacancies at the sensitive layer surface as shown in figure (2.15) [157, 158].

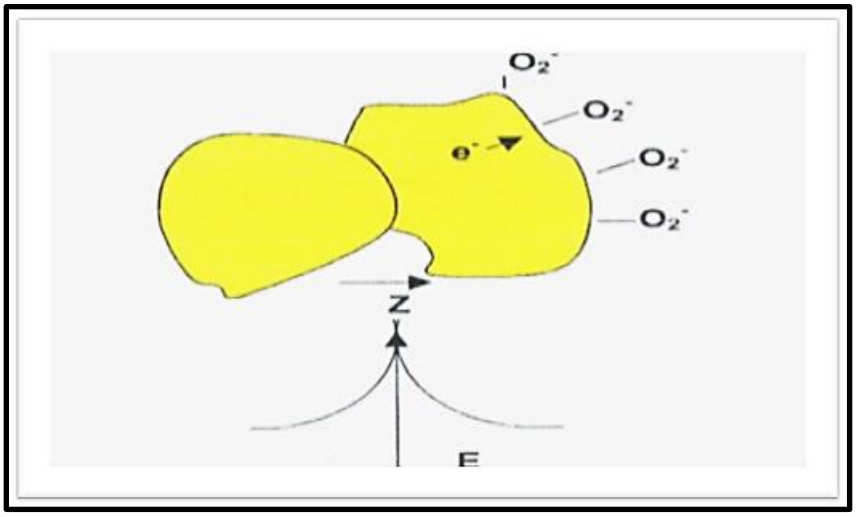

Figure (2.15) Oxygen vacancies at the surface of the grain [158].

The surface conductivity has shown to be much less than that of the bulk, which has been referred to the construction of oxygen ions near surface that are used for trapping electrons, producing a surface depletion layer leading to the growth of Schottky barriers at contacts between particle [159].

In n-type metal oxides, and due to the electrons resulting from ionized donors via the conduction band, the density of the charge carrier at the interface is decreased. Because of oxygen ions adsorption at the surface, the resistance at the connection among the grains of the matter will be altered, leading to depletion layer formation. In reactive gas

existence, the coverage of adsorbed oxygen ions at the surface may be reduced as well as the resistance as a result of the decrement in the surface potential barrier and depletion length [160, 161]:

The nanocrystalline presence is an essential parameter for gas sensing because it shows a significant increment in surface area compared to the microcrystalline [160].

2.19.3 Gas Sensor Characteristics

Gas Sensor are characterized by specific key parameters that characterize and specify the gas sensor in detail such as the sensitivity, response time and recovery time as included as follows:

2.19.3.1 The Sensitivity (*S*)

The sensitivity of sensors is defined as the relative variation of the sensitive thin film resistance in part per million (ppm) of the gas concentration applied. The most common definition of sensitivity is a change in the electrical resistance or conductivity of the thin film relative to the initial state upon exposure to reducing or oxidizing gas components. The sensitivity depends on the background gas composition, relative humidity level, sensor temperature, oxide microstructure, film thickness and gas exposure time. The sensitivity of oxidizing and reducing gases can be determined from the following equations [161, 162]:

$$S = \frac{\Delta R}{R_a} = \left|\frac{R_a - R_g}{R_a}\right| \text{ x } 100\ \% \qquad (2.38)$$

$$S = \frac{\Delta R}{R_g} = \left|\frac{R_g - R_a}{R_g}\right| \text{ x } 100\ \% \qquad (2.39)$$

Where R_a and R_g are the electric resistance of the sensor in air and in the presence of gas, respectively.

As can be calculated from the current as in the below relation [163]:

$$S = \left|\frac{I_g - I_a}{I_a}\right| \times 100\ \% \qquad (2.40)$$

Where I_a and I_g are the sample currents measured in the ambient environment and that under the test gas.

The sensitivity is highly dependent on film thickness, operating temperature, presence of additives and crystallite size.

2.19.3.2 Response Time (τ_{res})

It is the time interval over which the resistance of the sensor material attains a fixed percentage (usually 90 %) of the final value when the sensor is exposed to the full-scale concentration of the gas. A small response time value is highly desirable in applications such as the detection of flammable or combustible gases to prevent fire [164].

2.19.3.3 Recovery Time (τ_{rec})

It is the time interval above which sensor resistance is reduced to (10 %) of the saturation rate when the target gas is switched off and the sensor is sited in artificial (or reference) air a sensor should have a small recovery time so that it can be ready for the subsequent detection. Figure (2.16) atypical response curve of a conduct metric gas sensor [164].

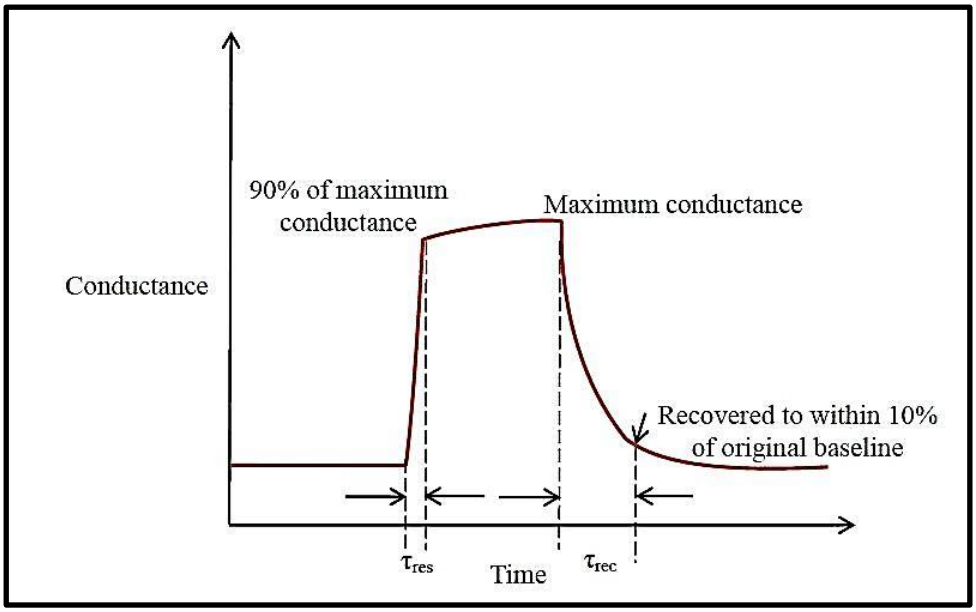

Figure (2.16): The atypical response curve of a conduct metric gas sensor [164]

Chapter Three

The Experimental Part

3.1 Introduction

This chapter includes preparing the pure and Ag-doped SiC thin films on different substrates such as glass, quartz and silicon with various dopant ratios (1, 3, 5 and 7 AgO) wt% using the pulsed laser deposition technique. In addition, it describes all the measurements used to study the properties of as-deposited films that are utilized to characterize the optical properties and gas sensing as shown in the diagram (3.1).

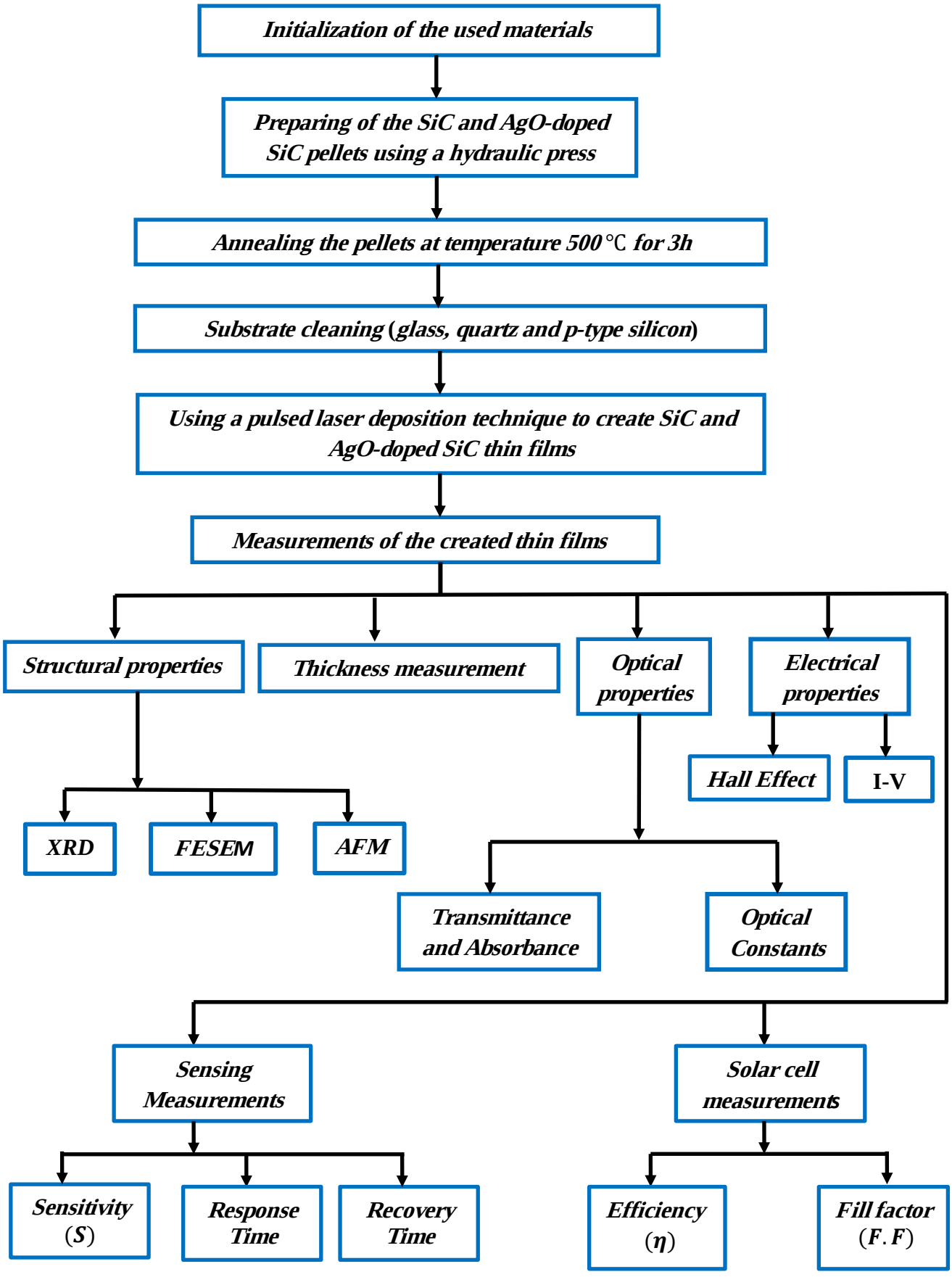

Figure (3.1): Schematic diagram of the experimental work.

3.2 Targets Preparation

SiC and AgO were used as powders supplied by (Nanjing Nano Technology Co., Ltd) with a purity of (99%) and molar mass (40.0962) g/mol for SiC and (123.8676) g/mol for AgO. The powders were weighed and mixed at different ratios of (1, 3, 5, and 7 AgO) wt% as shown in Table (3.1). SiC and AgO-doped SiC powders were compressed into the shape of pellets (tablets) with a thickness of about (5 mm) and a diameter (3 cm) using Chinese manufactured hydraulic piston under the pressure of (400 kg/cm^2). The pellets are annealed in the air at a temperature of (500℃) for 3 hours.

Table (3.1): Weights of tablets and mixing ratios.

Samples	ratio of AgO wt%	Weight of AgO (g)	ratio of SiC wt%	Weight of SiC (g)	Total (g)
SiC	0%	0	100 %	5	5
1% AgO	1 %	0.05	99 %	4.95	5
3% AgO	3%	0.15	97 %	4.85	5
5% AgO	5 %	0.25	95 %	4.75	5
7% AgO	7 %	0.35	93 %	4.65	5

3.3 Films Deposition

The deposition process of thin films consists of the following steps:

3.3.1 Cleaning the Substrates

Glass, quartz and p-type silicon substrates have been used for the deposition of thin films. These substrates are cut into rectangular pieces with dimensions (3.75 x 2.54) cm^2. The thickness of about (0.05 cm) for silicon and (0.12 cm) for both glass and quartz. They are also used to

measure thin films' structural, optical, and electrical properties and optical and gas sensing applications. The process of cleaning substrates is essential due to the influences of the oil or dust that affect the properties of the thin film. This process can be described as the following steps:

1. The substrates are cleaned in distilled water to remove the impurities from their surface.
2. Immersed the substrates in a beaker containing pure alcohol (C_2H_5OH) for (12-15) min to clear any oil.
3. The substrates were dried by exposing them to blown air and wiping them using fine cleaning paper. Finally, the slides are kept in a container and thus ready for the thin film deposition.
4. The silicon substrates have been placed in a container containing a combination of 10% HF and 90% ethanol alcohol with 99 % purity for 10 min. The deposition procedure is carried out promptly after the silicon substrates have been withdrawn from the container.

3.3.2 Pulsed Laser Deposition System

The PLD test has been achieved in a vacuum chamber with a vacuum pressure of about (10^{-4} mbar) in most situations. The Nd:YAG laser is focused by a lens with a focal length of (30 cm) as shown in figure (3.2). The laser beam is passed into the chamber via a window made of quartz material. A sufficient distance is maintained between the substrate and the target such that the substrate holding does not block the incoming laser beam. Adjustment of the deposition components on a regular basis in order to get higher quality films via the process, such as heating the substrate, rotating the target, and positioning the substrate in respect to the target, which is located at the University of Babylon.

Figure (3.2): Pulsed Laser Deposition system.

3.3.3 Nd:YAG Laser Source

Q-switched Nd:YAG laser (Huafei Tongda Technology-Diamond-288 pattern EPLS) was used for the deposition of SiC and AgO-doped SiC. The entire system consists of a light route system, a power supply system, a cooling system, and a computer controlling system, with the light route system being installed in the manual handle and the controlling and cooling systems in the power supply machine box. The Nd:YAG laser system was utilized to precipitate thin films with easy-to-control major parameters, as shown in Table (3.2).

Table (3.2): The main parameters of the Nd:YAG laser used in the deposition process.

Laser model	Q-switched Nd:YAG Laser
wavelength	1064 nm
Energy per pulse	500 mJ
Pulse duration	10 ns
Ambient temperature	30 ˚C
Pulse repetition rate (PRR)	6 Hz
Divergence	0.1 mrad
Diameter of Beam	3 mm
Number of pulses	1000 pulse
Power supply	220 Volt
Cooling technique	inner circulation water cooling

3.3.4 Deposition Chamber

The deposition chamber is cylindrical. The chamber geometry may be created freely since the PLD technique does not require an ultra-high vacuum. The chamber often includes the pumping system, pressure monitoring, gas inlets, substrate, target, laser beam, and view components. The following factors should be taken into account while constructing a chamber:

1. The components inside the chamber should be arranged so that the laser beam path is not disrupted.
2. The components of the chamber are regularly and continually changed. Therefore, the target-substrate should be accessed directly.
3. The substrate-target distance should be changeable.
4. The laser window deposition must be eliminated to the greatest extent feasible.

3.3.5 Target Holder

During the deposition process, the ablation target is held vertically by the target holder. The target was usually in the form of disk-shaped to achieve uniform ablation. It is necessary to rotate during the deposition process while the laser reaction spot remains stationary. This arrangement provides an advantage, where the surface area of the target may be used more effectively and successfully for a more extended period without creating a hole.

3.3.6 Vacuum System

The chamber has been evacuated using the rotary pump connecting at once to the chamber. The use of metal bendy tubes to get a vacuum extra than 10^{-2} mbar and via way of means of the use of Pirani gauge, tracking the stress in the chamber. The rotary pump is a type (GALILEO TP model 949-9325S006) and is the main part of the discharge and the diffusion pump from type (DIFFUSION PUMP DPF-4Z). For depositing all films on silicon and quartz substrates, has been used a Q-switch Nd:YAG laser with a wavelength of (1064 nm), energy per pulse of (500 mJ), a pulse repetition rate of (6 Hz), a pulse duration of 10 ns, several pulses of (1000), and deposition temperatures of (250℃).

3.3.7 Deposition Steps

1. The vacuum chamber was cleaned with acetone alcohol and a soft cloth; after that it left about 24 hours exposed to air.
2. The substrates have been placed on another substrate holder to ensure they will be in opposite direction proportional to the target set on the rotating target holder to obtain that the distance between the target and the substrate is (3 cm).
3. The laser beam of Nd:YAG with energy (500 mJ) and a number of pulses (1000) has been focused on the targets using a lens with a

convex focal length 0f (30 cm) on the surface of the rotating target at a fallen angle of approximately 45^{o}.

4. The vacuum chamber is closed, then the discharge process starts by opening the rotary pump's valve when the pressure reaches about (10^{-2} mbar). Then it closes and the valve of the diffusion pump is opened until the vacuum chamber pressure reaches about (10^{-5} mbar).
5. The temperature is increased to (250℃) using a halogen lamp to improve the adhesion of ablated particles.
6. After the particles reach and are adhered to the substrate, the discharge chamber valve remains open.
7. Finally, the thin films of the SiC and AgO-doped SiC material are obtained on glass, quartz, and silicon substrates and are subjected to structural, electrical, optical, solar cell, and gas sensor investigations.

3.4 Measurement of Thin Film Thickness

The thickness of the films was measured using the optical interference method, using a He-Ne laser with a wavelength of (632.8 nm) with an incidence angle of 45° as shown in figure (3.3). The working principle of the above method depends on the interference of light waves, which are reflected from the thin film surface and those that are reflected onto the substrate on which the films were deposited are prepared and can be using the following relation for calculated the thickness of the films [165]:

$$t = \frac{y}{x} \cdot \frac{\lambda}{2} \qquad (3.1)$$

Where t, x, y, and λ are the thickness of the film, the width of the light fringes, the width of the dark fringes and the wavelength of the laser light, respectively. Film thickness was measured at the University of Al-Qadisiyah.

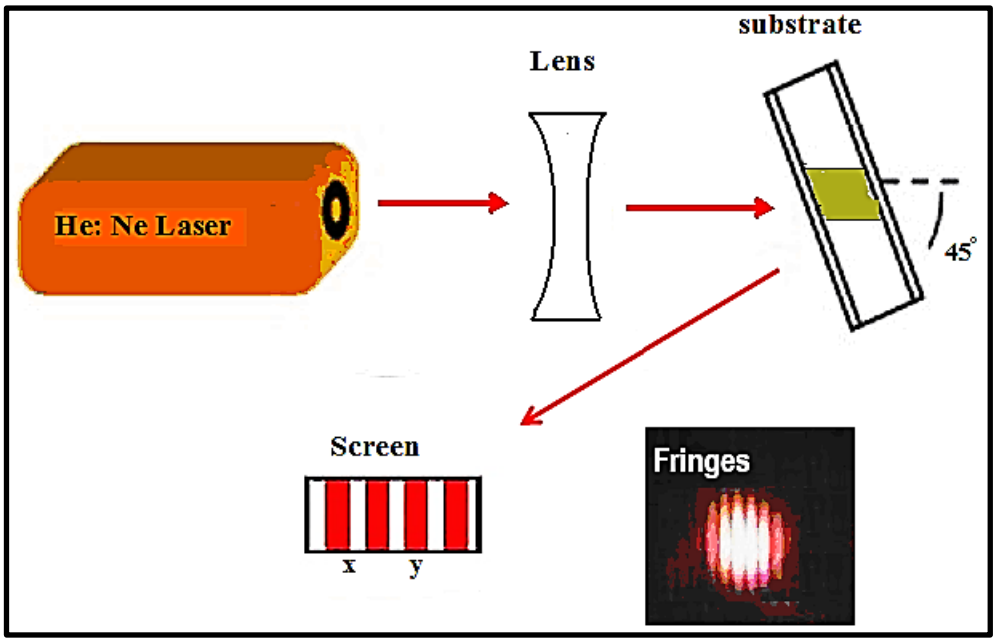

Figure (3.3): Thin film thickness measurement scheme using optical interference

3.5 Structural Measurements and Topographic Surfaces

3.5.1 X-ray diffraction (XRD)

The technique of XRD was used to examine the crystal structure of SiC thin films. The model is (HR-XRD-X'Pert PRO MRD) from PANALYTICAL/PHILIPS Company, which is located at the University of Tehran, and has the following features given in the Table (3.3):

Table (3.3): XRD device specifications.

Target	Cu, kα
Step size	0.05 deg
Time per step	1s
Wavelength	1.5406 Å
Current	20 mA
Voltage	30 kV
Range (2Θ)	from 10 to 80 deg

3.5.2 Field Emission Scanning Electron Microscopic

Using a high-resolution photographs and magnification FESEM. The essence and morphology of the prepared thin films' surface, as well as the internal structure of the thin films' substance have been investigated. Photons with X-ray wavelengths are produced when primary electrons react with the sample. The atomic ratio in the sample can be measured using energy dispersive spectroscopy. After this emission is detected by (Tescan Mira3 FESEM, French) image operating at an accelerating voltage from (0.2 to 30 kV) [112, 113], which is located at the University of Tehran.

3.5.3 Atomic Force Microscope (AFM)

To know the thin film topography of the prepared SiC using the PLD technique, this was done by the atomic force microscope (TT-2 AFM) located at the University of Tehran.

3.6 Optical Measurements

Optical measurements, including the transmittance and absorbance spectrum of deposited films were performed using (UV-Visible Spectrophotometer/2700) two-beam supplied by the (CECIL) English company. The thin films are deposited on quartz substrates that are well-positioned in the substrate window, allowing light to radiate vertically to the thin film. A non-deposited quartz sample with deposited quartz was placed into the window to determine the absorbance of thin films. It is often used as a reference to minimize the quartz influence. The optical energy gap (E_g) was determined as well as calculating the other optical constants finite involve the absorption coefficient (α), extinction coefficient (k_o) and refractive index (n) which is located in our college.

3.7 Electrodes Deposition and Preparation of Masks

Three types of masks were made for electrical and sensing measurements. All masks are shown in the figure (3.4) are used aluminium sheets to get the required form of electrodes. These masks have the exact dimensions as the substrate and have been attached and fully fastened to cover the substrate after cleaning. The golden electrodes were deposited on the surface of thin films using the spraying technique of the type (CRESSINGTON-108). The device is located in the College of Science, University of Baghdad.

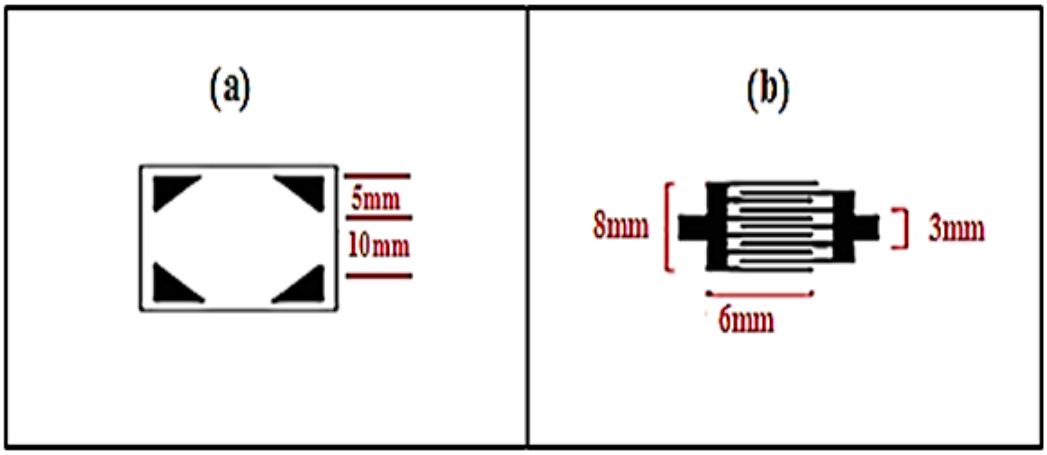

Figure (3.4): The mask patterns used in (a) Hall effect measurement and (b) sensing measurement.

3. 8 Electrical Properties

3.8.1 Measurement of the Hall Effect

Hall effect measurements of deposited films were carried out to know the charge carriers type and to calculate the Hall coefficient (R_H), the concentration of carrier, resistivity and mobility by using a device (Measurement Hall Effect System) type (HMS 3000) manufactured by (Ecopia) Taiwanese origin. It is possible to identify both of type and density of charge carriers using the intensity of the magnetic field (B = 0.55 T) and through the relationship between measured current (I) and Hall voltage (V_H). If the relationship is direct, the film is a positive

type (P-type), while the film is negative (n-type) if the relationship is inverse [141, 142]. The device is located in the College of Science, University of Baghdad.

3.9 Electrical Properties of Heterojunction

The electrical measurements for the n-SiC/p-Si and n-SiC:AgO/p-Si heterojunctions, which are prepared on the Si substrate at (250℃) and different contents of AgO are performed using the Keithley source meter model 2400-SCS. Current-voltage characteristics for the heterojunctions are measured in dark and illumination conditions.

3.9.1 The I-V Characteristics in the Dark Condition

The current-voltage measurements at dark are fulfilled for n-SiC/p-Si and n-SiC:AgO/p-Si heterojunctions as shown in figure (3.5).

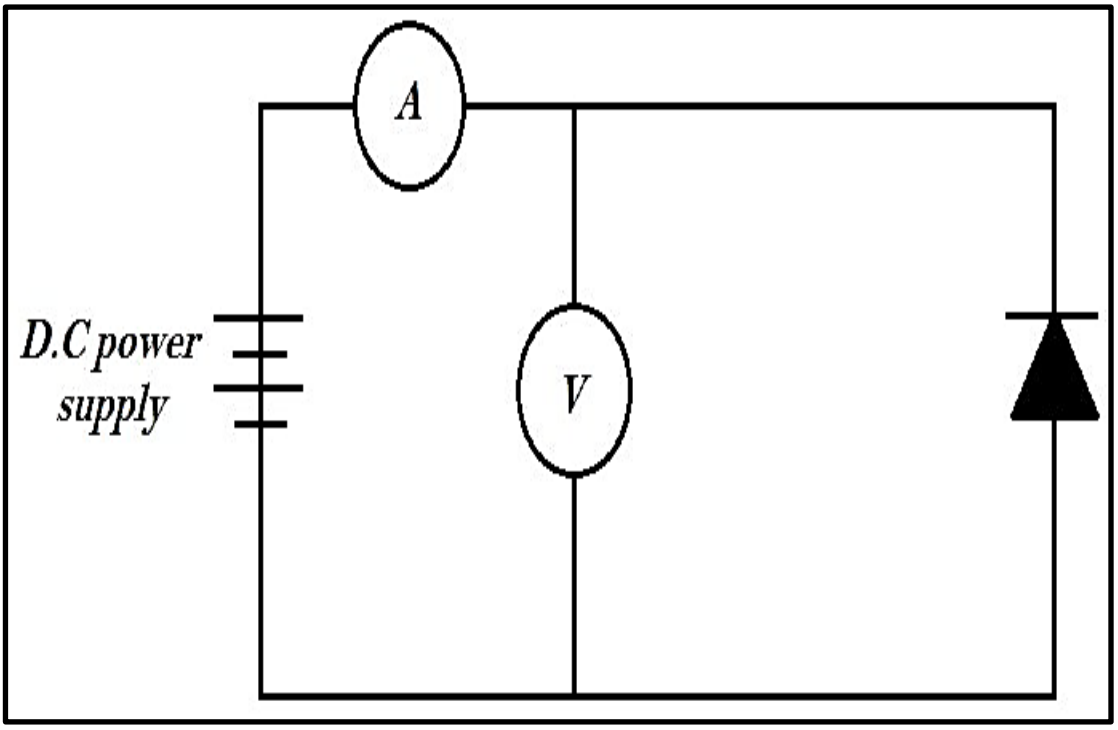

Figure (3. 5): Circuit diagram for I-V measurement in the dark.

3.9.2 The I-V Characteristics under Illumination Condition

The I-V measurements were made for n-SiC/p-Si and n-SiC:AgO/p-Si as shown in figure (3.6) heterojunctions when they exposed to a halogen lamp light source with a power of (120W) and an intensity of (105 mW/cm^2). The bias voltage changes in the range of (-5 to 5) volts in the forward and reverse bias. The device is located in the College of Science, University of Baghdad.

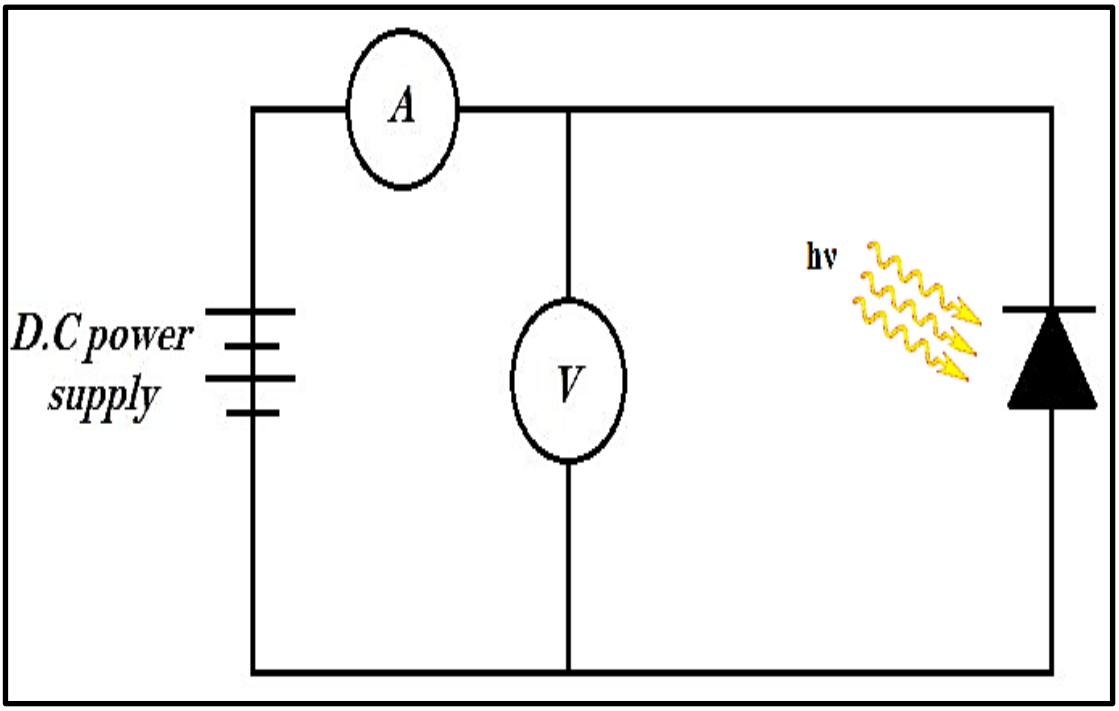

Figure (3. 6): Circuit diagram for I-V measurement in the illumination.

3.10 Gas Sensor System

Sensor measurements have been carried out by measuring the variation in resistivity resulting from exposing the surface of the thin film to gases like NH_3 (reduced gas) and NO_2 (oxidizing gas), and the temperature is recorded by a thermocouple type-K (XB 9208B). The bias voltage was provided by the power provider (FARNELL E350). Resistance is recorded through (Fluke Digital Multimeter 8845A/8846 A) and the sensor characteristics of thin films are measured using it. The device is located in the College of Science, University of Baghdad.

Chapter Four

Results and Discussion

4.1 Introduction

This chapter includes the results and the analysis of the experimental measurements of the structural, optical, and electrical properties for SiC and SiC:AgO thin films prepared by pulsed laser deposition technique at different AgO content (1, 3, 5, and 7 AgO) wt% on glass, quarts and p-type silicon substrates at about (250 ℃). XRD, SEM, EDX, AFM, and UV-Vis spectrophotometer techniques were used to study the structural and optical properties of the prepared films. The thickness of the thin films was found to be (200 ± 5) nm. The current-voltage characteristics measurements at dark and illumination were investigated for SiC/p-Si and SiC:AgO/p-Si heterojunctions. The photovoltaic measurements that include solar cells' efficiency and fill factor are discussed. Finally, sensitivity, response time, and recovery time have been measured of SiC thin films and determined operating temperature.

4.2 Structural Properties of SiC:AgO Thin Films

4.2.1 X-Ray Diffraction Analysis

Figure (4.1) is shown the XRD pattern of SiC powder. It is noted from the Figure that sharp and strong peaks have appeared, revealing the material's crystalline structure. The diffraction peaks at about (35.2˚), (42.05˚), (60.11˚) and (76.12˚), which correspond with (111), (200), (220) and (222) planes, according to standard (ICCD Card No:29-1129) [166]. The Figure reveals the crystalline nature of SiC powder due to diffraction peaks. SiC powder gives strong diffraction intensity and sharp peaks agree with its bigger particle size, this result is consistents with the studies [167-169].

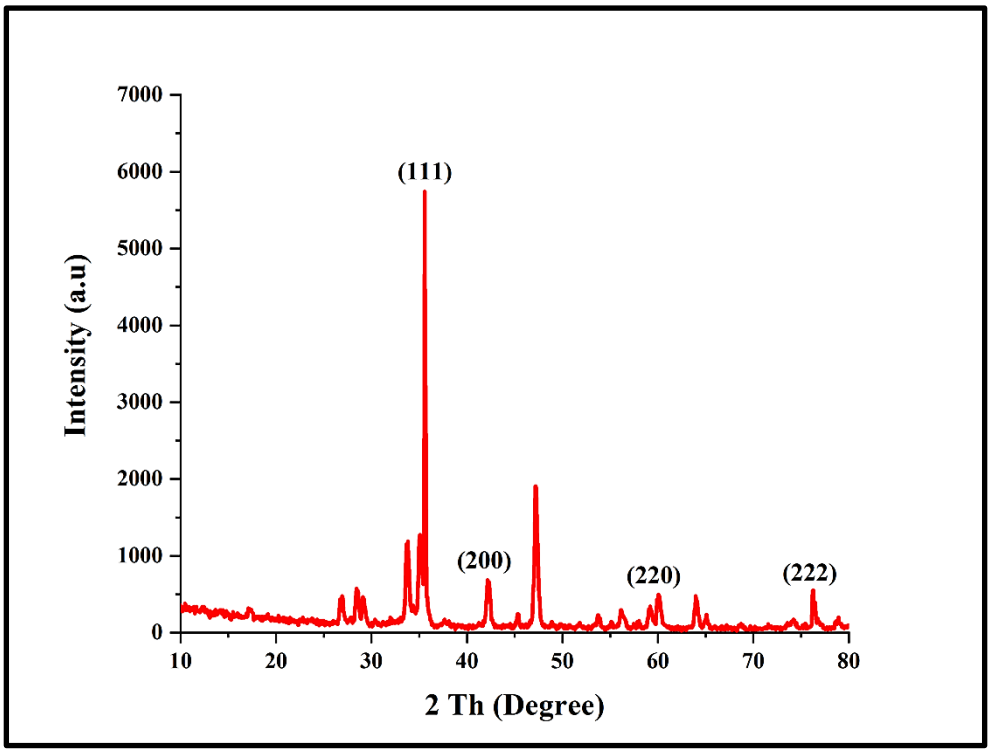

Figure (4.1): XRD pattern of silicon carbide powder.

Figure (4.2) show the X-ray diffraction spectra of as-deposited SiC:AgO thin film with different AgO ratios (1, 3, 5, and 7 AgO) wt% that were prepared by the PLD method at the substrate temperature of about (250℃). For the SiC:AgO thin films, no sharp and clear peaks were observed for the SiC material under the available deposition conditions, this agrees with the works [40, 50]. These studies confirmed that without annealing and with annealing temperatures ranging from (500 to 850℃) the results show broad and weak peaks.

The X-ray diffraction patterns for as-deposited SiC:AgO thin films show diffraction peaks of Si at (2θ) equal to (28.91˚), (47.8˚), (62.12˚), (66.314˚), and (69.577˚) which correspond with (111), (220), (332), (420), and (442) planes, according to standard (ICCD Card No:27-1402 and No:17-0901) [170, 171], these diffraction patterns refer that SiC:AgO thin films have a polycrystalline structure with a cubic phase. X-ray analysis also shows the sharp peak of (33.452˚) for silicon dioxide (SiO_2) which corresponds to the Miller index (320), based on standard

(ICCD Card No:45-0131) [172], where it was observed that the intensity of peak (33.452˚) increases significantly due to the large difference in the atomic radius of Si (111 pm) and oxygen (48 pm) [173].

The peak (16.573˚) that corresponds to reflection (100) belongs to the diffraction pattern of silver oxide (AgO), based on standard (ICCD Card No:43-1038) [174]. The two chemical compounds SiO_2 and AgO have been formed from the correlation of the oxygen atoms with silicon and silver atoms with different bonds (covalent and ionic).

It is noted that there is a slight displacement in the locations of some characteristic peaks of the prepared films with increasing the ratios of silver as well as a noticeable decrease in the intensity values and that the explanation for this may be attributed to the large atomic radius of silver (165 pm) compared to the atomic radius of silicon (111 pm) and carbon (67 pm) [173].

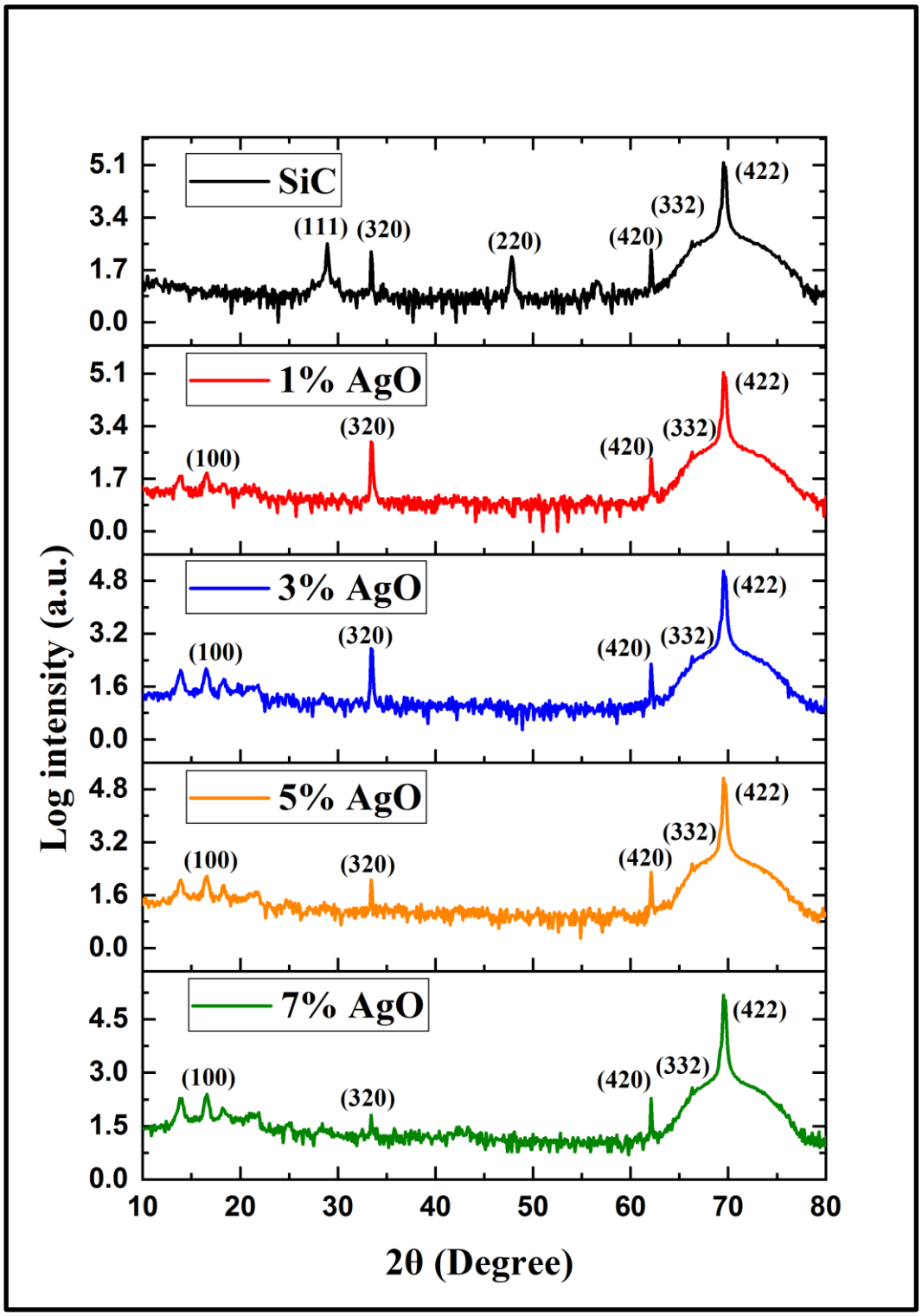

Figure (4.2): The XRD patterns of SiC:AgO thin films with different AgO ratios.

Tables (4.1) and (4.2) show the structural parameters, interplanar spacing (d), crystalline size (D), dislocation density (δ) and lattice microstrain (ε) for as-deposited SiC:AgO thin films. The d-spacing has been calculated using the equation (2.4), which shows good agreement

with the standard values as exhibited in Table (4.1). D, δ and ε were calculated using the equations (2.6), (2.7) and (2.8). Table (4.2) shows average crystalline size, dislocation density, and micro-strain values for prepared thin films.

Table (4.1): X-ray diffraction parameters of as-deposited SiC:AgO films.

Samples	2θ (Deg)	FWHM (Deg)	C.S (nm)	Dislocation density (δ) x 10^{-3} (lines/nm^2)	Micro Strain (ε) x 10^{-3}	hkl	d (nm)	d_{stand} (nm)
SiC	28.91	0.192	42.749	0.548	0.811	111	0.3086	0.3137
	66.314	0.407	23.323	1.838	1.486	332	0.1408	0.1409
	69.577	0.241	40.149	0.620	0.863	422	0.1351	0.1354
1% AgO	33.452	0.183	45.350	0.486	0.764	320	0.2677	0.2674
	66.308	0.343	27.674	1.306	1.253	332	0.1408	0.1409
	69.576	0.24	40.317	0.615	0.860	422	0.1350	0.1354
3% AgO	16.573	0.371	21.649	2.133	1.601	100	0.5345	0.5598
	66.264	0.33	28.757	1.209	1.205	332	0.1409	0.14096
	69.574	0.229	42.253	0.560	0.82	422	0.1350	0.1354
5% AgO	16.506	0.394	20.384	2.407	1.701	100	0.5366	0.5598
	33.452	0.184	45.104	0.492	0.769	320	0.2677	0.2674
	66.282	0.216	43.938	0.518	0.789	332	0.1409	0.14096
	69.574	0.246	39.333	0.646	0.881	422	0.1350	0.1354
7% AgO	16.568	0.402	19.980	2.505	1.735	100	0.5346	0.5598
	66.309	0.388	24.464	1.671	1.417	332	0.1409	0.14096
	69.573	0.231	41.887	0.570	0.828	422	0.1350	0.1354

From Table (4.2), it is noted that the average crystallite sizes of the (SiC) and (1, 3, 5, and 7 AgO) wt% samples were equal to (35.407, 37.780, 30.886, 37.189, and 28.777) nm, respectively, and this indicates that the structure of these films is in nanoscale. The noticeable change in crystalline size values for all samples is due to the addition of AgO with different ratios to SiC. The highest average values of the dislocation density and microstrain were (1.582) and (1.326) which belong to the (7% AgO) sample, this corresponds to the lowest value for the average crystallite size (25.842 nm) because of the inverse relationship between them [106, 107].

Table (4.2): The important calculated structural parameters of SiC:AgO films.

Samples	Avg.(D)	Avg.(δ) x 10^{-3}	Avg. strain x 10^{-3}
SiC	35.407	1.002	1.054
1% AgO	37.780	0.802	0.959
3% AgO	30.886	1.301	1.209
5% AgO	37.189	1.016	1.035
7% AgO	28.777	1.582	1.326

4.2.2 Field Emission Scanning Electron Microscopy

The surface morphology of as-deposited SiC:AgO films with different Ag content (1, 3, 5, and 7 AgO) wt% that have prepared under the same conditions were analyzed using field-emission scanning electron microscopy (FESEM). Figures (4.3) to (4.7) show the low magnification images (200nm and 500 nm) of the SiC and AgO-doped SiC thin films. The FESEM images of all films showed the appearance of different sizes of particles, where the average grain size of the films was approximate (38.88 nm), (31.04 nm), (31.72 nm), (31.89 nm) and (45.77 nm) for (SiC) and (1, 3, 5, and 7 AgO) wt% samples, respectively. The average grain

size values of the AgO-doped SiC gradually increase and the reason is attributed to the increase in the ratios of AgO. The highest value of the average grain size measured by the FESEM technique was for the (7% AgO) sample, while the lowest value was for the (1% AgO) sample.

From the FESEM images which appear in figures (4.3) to (4.7), it was found, that the shape of the particles was irregular and of various sizes; this is due to the non-homogeneity in the grains of the films because of their aggregation. . The images show a uniform distribution of nanosphere-like structures aggregated to develop a porous surface. When the SiC film was doped with silver oxide, more nanospheres aggregated into sea-stone-like structures with varying grain sizes, resulting in a highly porous surface.

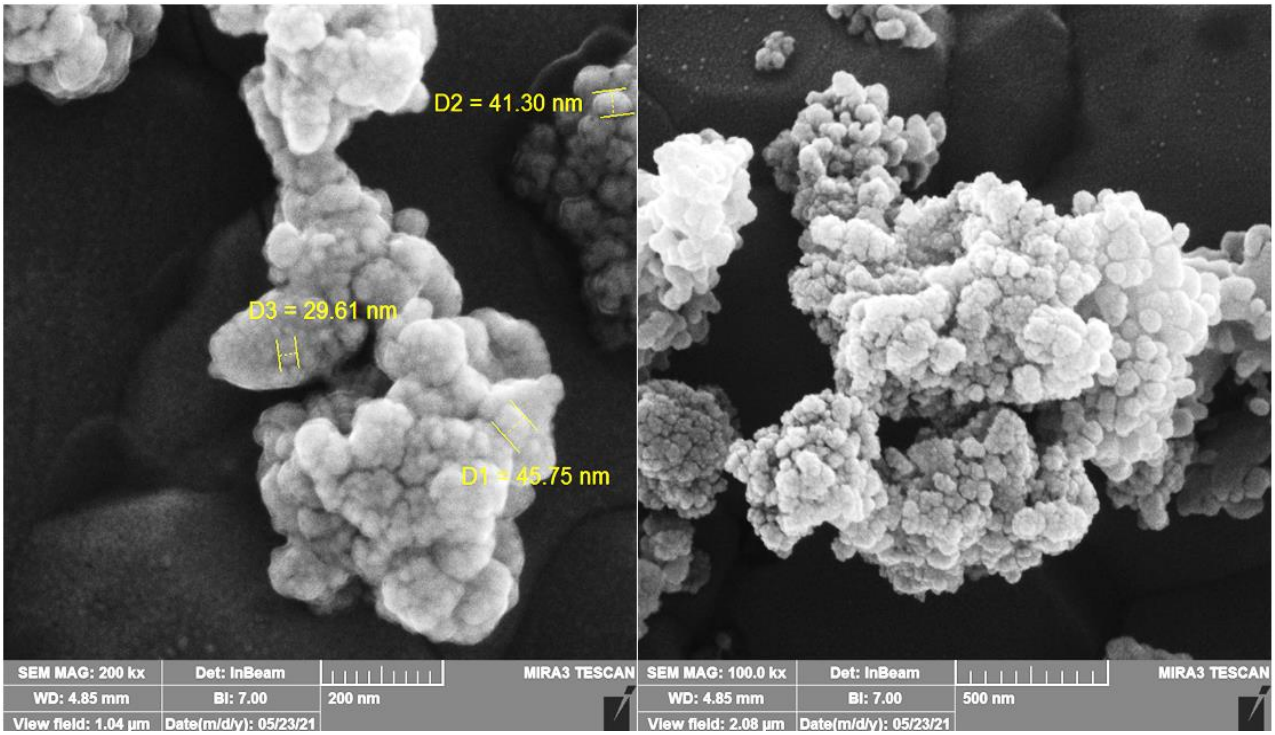

Figure (4.3): SEM image of the SiC thin films.

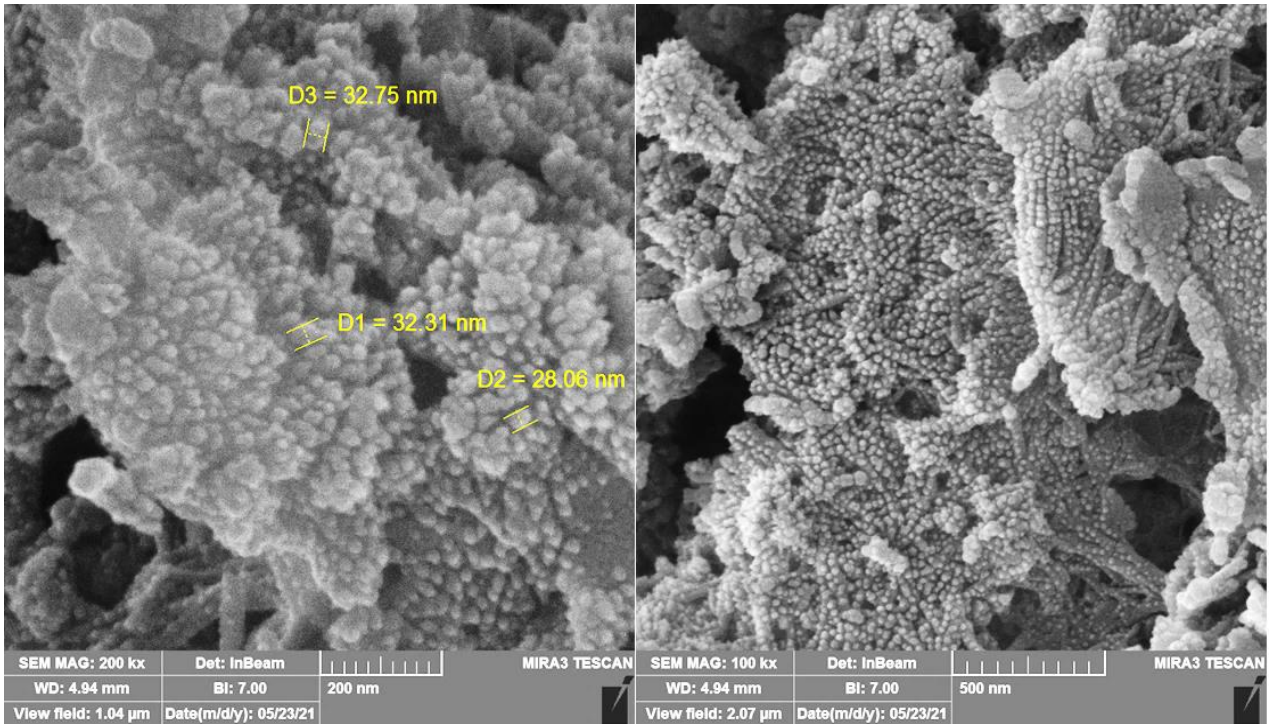

Figure (4.4): SEM image of the AgO-doped SiC thin films (1% AgO).

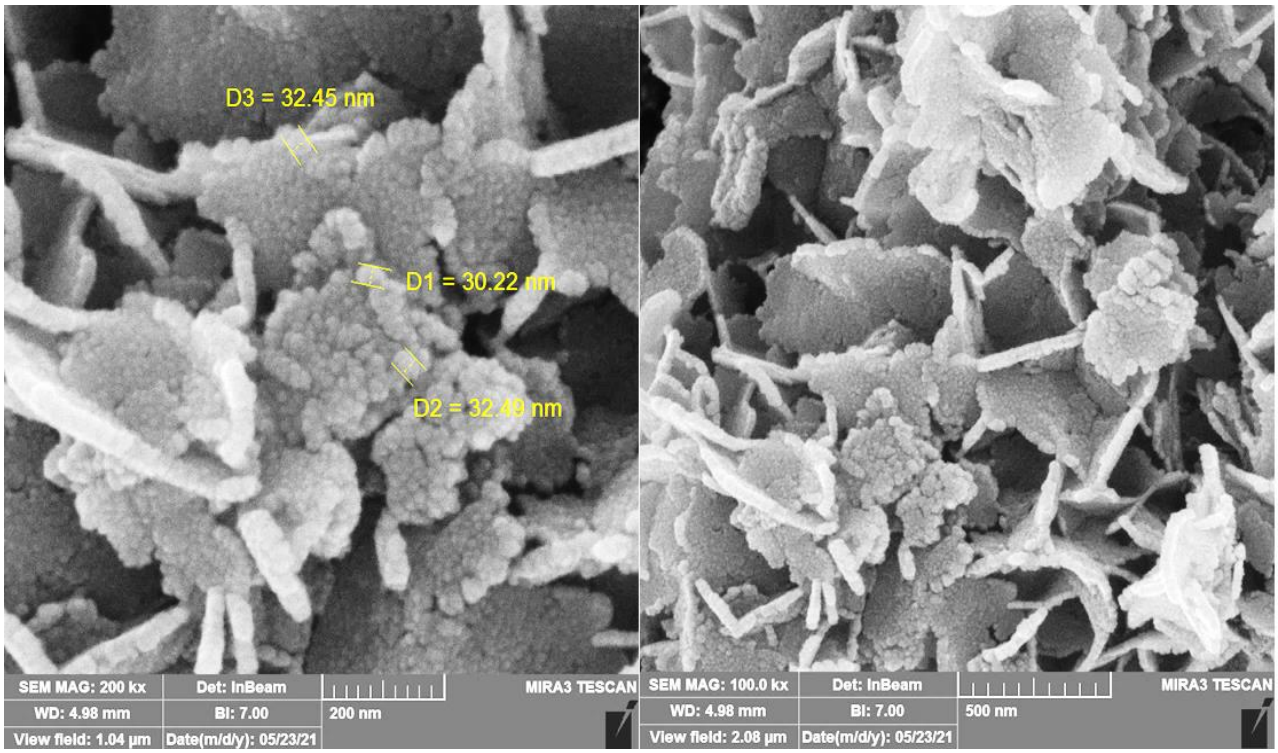

Figure (4.5): SEM image of the AgO-doped SiC thin films (3% AgO).

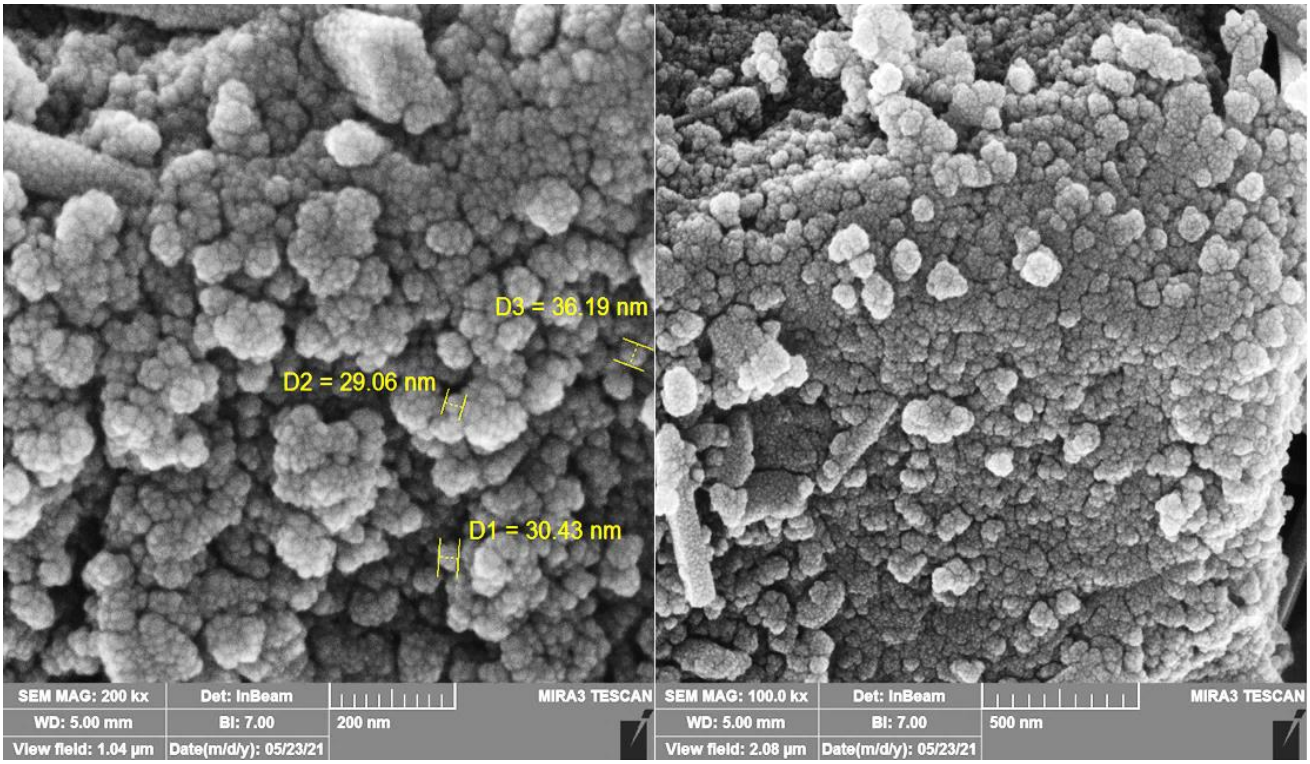

Figure (4.6): SEM image of the AgO-doped SiC thin films (5% AgO).

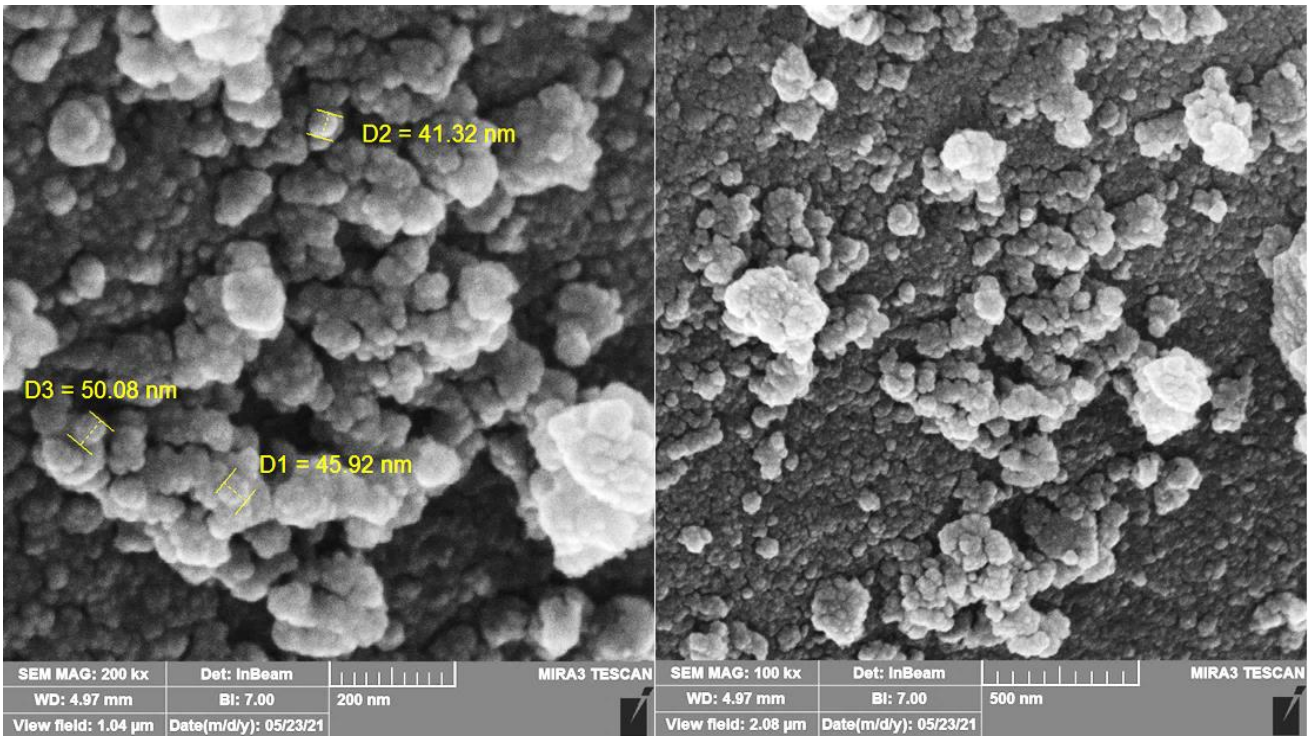

Figure (4.7): SEM image of the AgO-doped SiC thin films (7% AgO).

4.2.3 Elemental Analysis (EDX)

Energy-dispersive X-ray spectroscopy (EDX) utilizes the X-ray spectrum released by a solid sample bombarded with a directed beam of electrons to achieve a localized chemical analysis for elements of that sample [175]. Figures (4.8) to (4.12) exhibit the EDX spectra of SiC:AgO films with different ratios (1, 3, 5, and 7) wt% of AgO. In the EDX spectrum of the SiC sample, the Si, C, and O lines can be seen clearly. For the (1, 3, 5, and 7 AgO) wt% samples under study, the chemical elements (Si, C, O, and Ag) can be observed in the EDX spectrum. It found an increase in the element concentrations (C, O, and Ag) and a decrease in the concentration of Si, and the appearance of oxygen is attributed to the occurrence of an oxidation process that led to the formation of oxides of Si and Ag. This result corresponds with the measurements of the X-ray diffraction. The EDX analysis of the SiC:AgO films has been listed in Table (4.3).

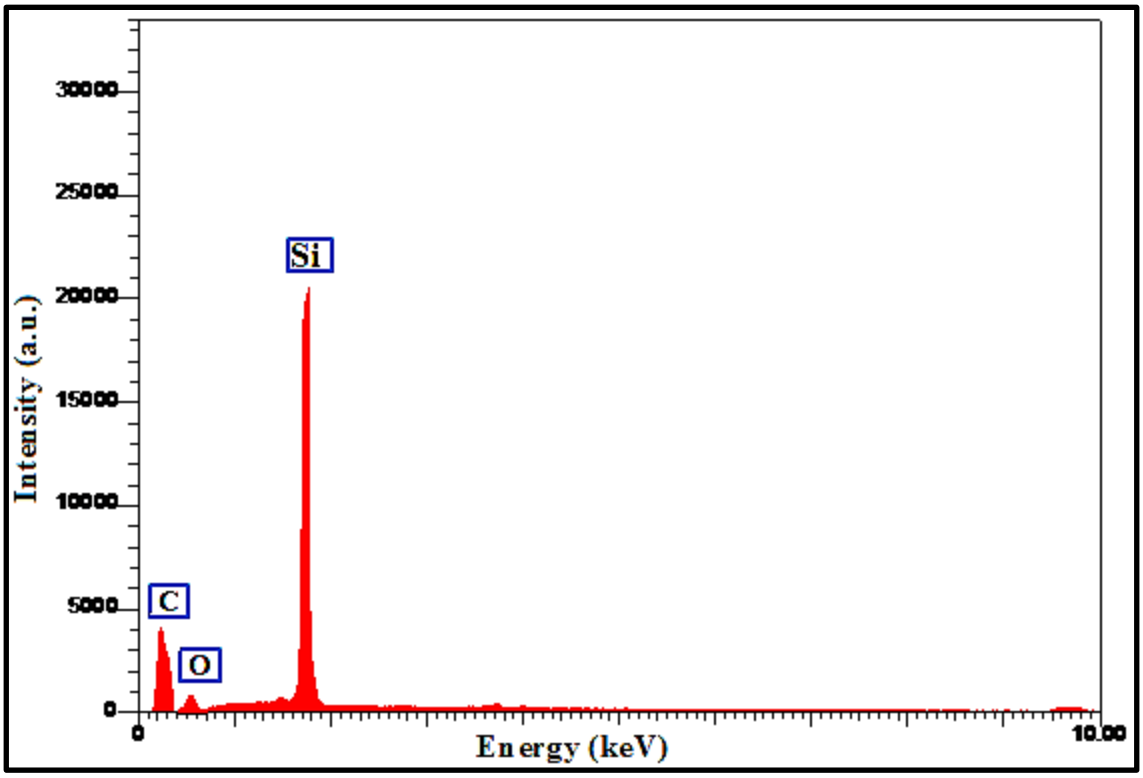

Figure (4.8): EDX spectra of the SiC thin film.

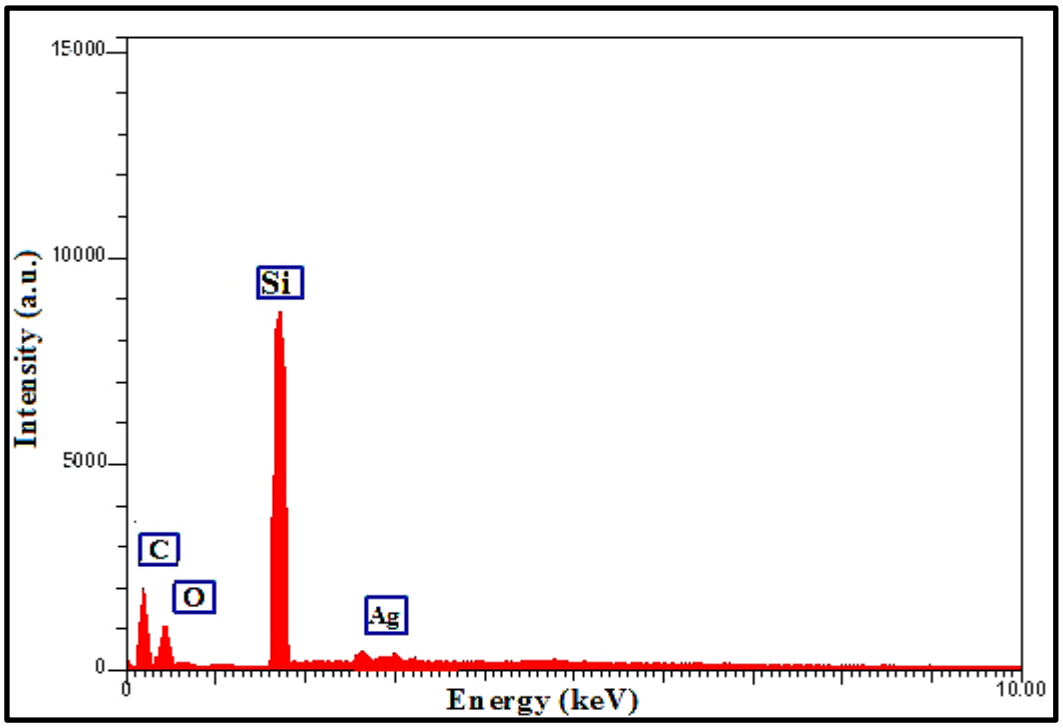

Figure (4.9): EDX spectra of the (1% AgO) thin film.

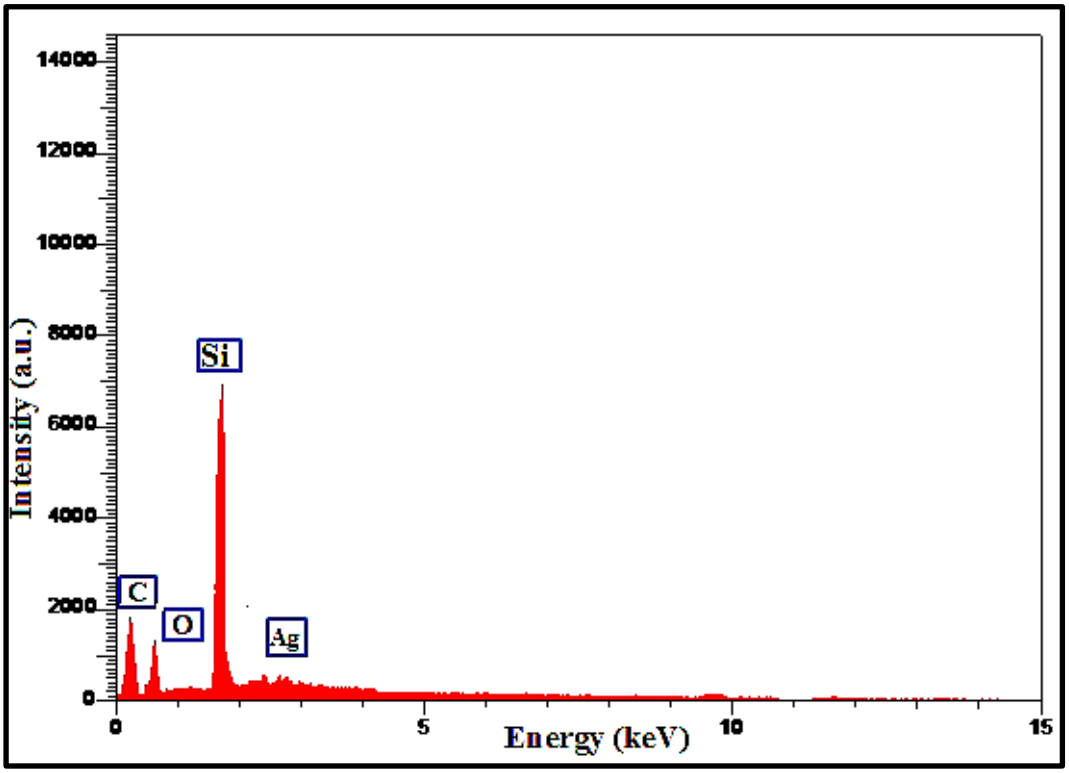

Figure (4.10): EDX spectra of the (3% AgO) thin film.

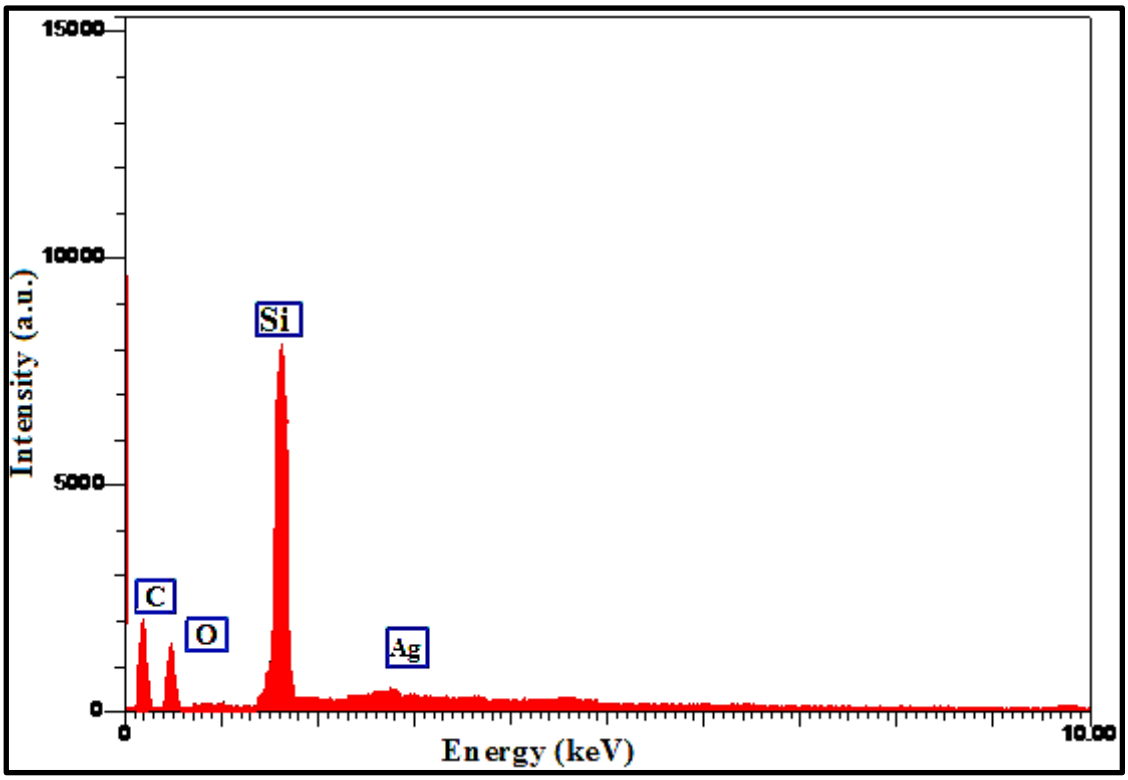

Figure (4.11): EDX spectra of the (5% AgO) thin film.

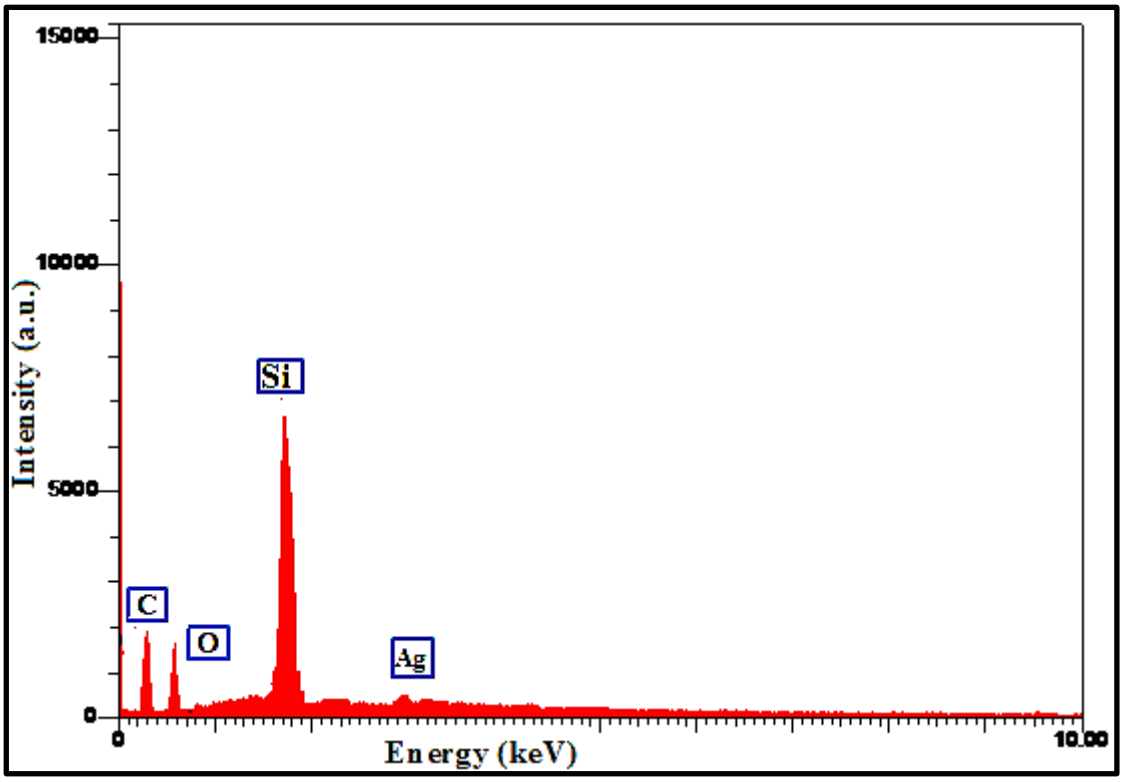

Figure (4.12): EDX spectra of the (7% AgO) thin film.

Table (4.3): The elements ratios of EDX analysis of SiC:AgO films.

Samples	Si	C	O	Ag	Total
SiC	70.13	22.52	7.35	0	100
1% AgO	63.42	23.86	9.13	3.59	100
3% AgO	58.49	25.38	11.26	4.87	100
5% AgO	53.04	26.93	14.37	5.66	100
7% AgO	48.61	27.83	17.24	6.32	100

4.2.4 Atomic Force Microscopy

Atomic force microscopy (AFM) was used to study the surfaces topography of SiC:AgO thin films prepared by PLD technique with different AgO ratios (1, 3, 5 and 7) wt% to analyze it and to give a clear idea about some essential parameters of them, such as the average particle size and distribution. As well as the values of root mean square (RMS) and roughness (Ra) of the surface as shown in Table (4.4).

As shown in the Table below, the results indicate a clear change in the surface topography of the samples. This is attributed to the change in AgO ratios. The highest value for the Ra, RMS, and average particle size have been recorded at (1.97 nm), (2.42 nm), and (45.06 nm) which belongs to the (3% AgO) sample, while the lowest values were obtained were (0.75 nm), (1.01 nm) and (12.66 nm) for the (7% AgO) sample. The small difference between the grain size values registered by the AFM and XRD are due to the values recorded by the AFM being direct and accurate, while the X-ray diffraction measures the grain size using Schererr's formula.

Figures (4.13- 4.17) show the three-dimension (3D) AFM and size distribution histograms images of the as-deposited SiC and SiC:AgO thin films. The white patches shown in these figures have been attributed to

the formation of agglomerated grains stacked on top of each other, consequence, close grains cluster together to form enormous clusters. Increasing AgO ratios improve the crystalline structure of SiC:AgO films which has an excellent agreement with XRD results and this leads to improving the sensitivity properties.

Table (4.4): AFM parameters for SiC:AgO thin films.

Samples	Ra (nm)	RMS (nm)	Ave. Particle Size (nm)
SiC	1.30	1.76	31.73
1% AgO	0.87	1.16	21.04
3% AgO	1.97	2.42	45.06
5% AgO	1.31	1.70	34.83
7% AgO	0.75	1.01	12.66

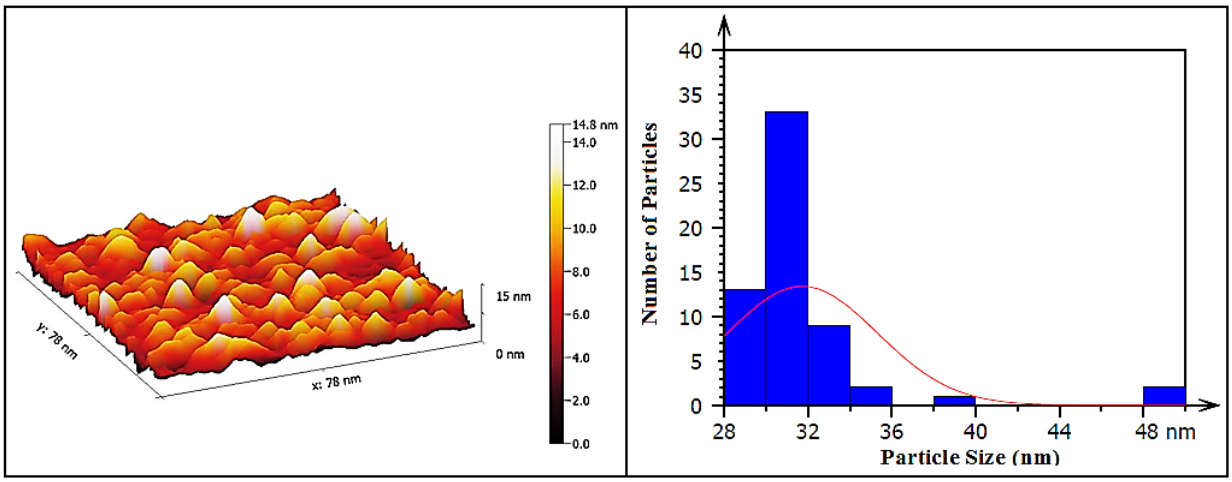

Figure (4.13): AFM and size distribution histograms images of SiC film.

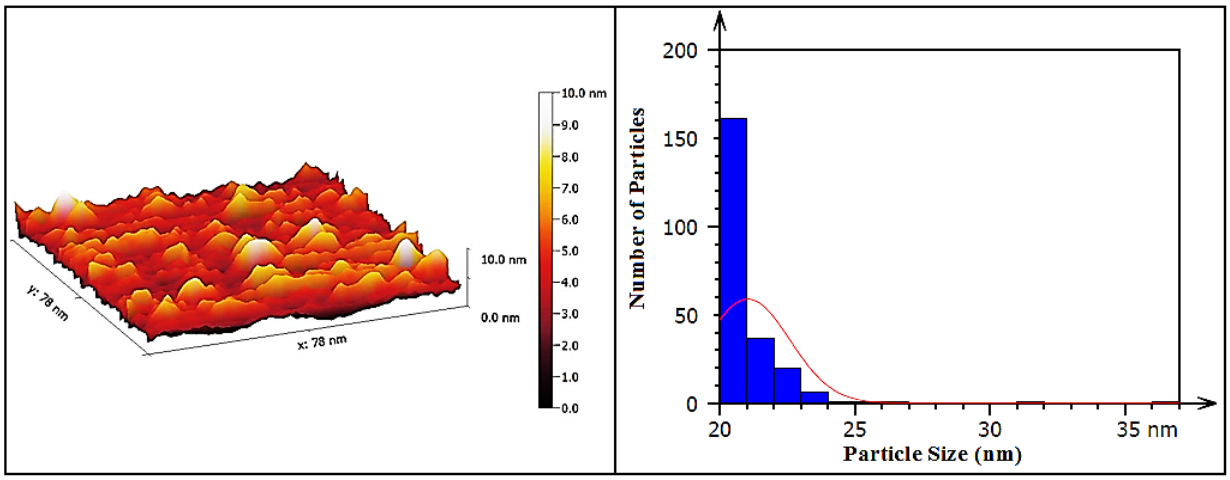

Figure (4.14): AFM and size distribution histograms images of SiC:AgO film with (1% AgO).

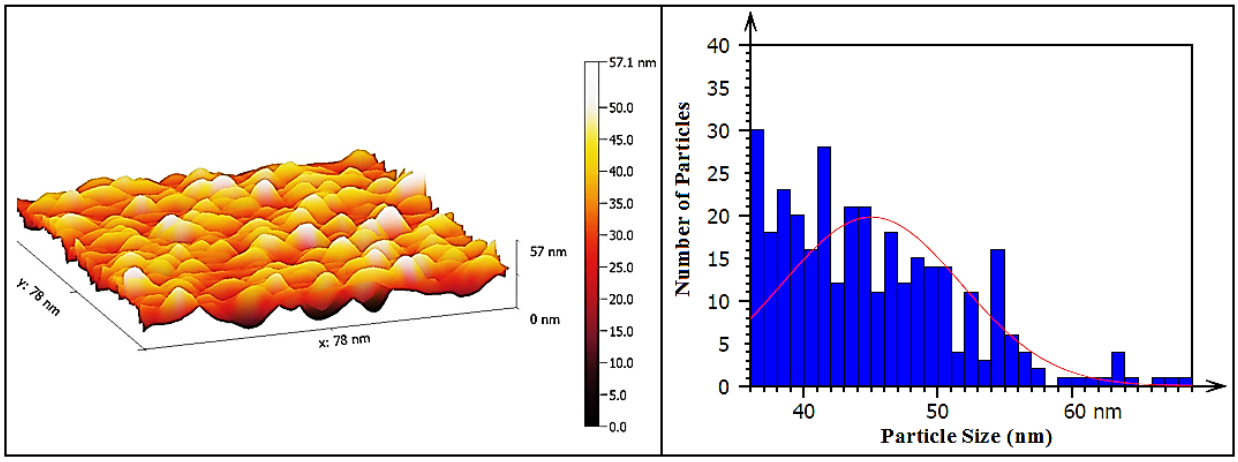

Figure (4.15): AFM and size distribution histograms images of SiC:AgO film with (3% AgO).

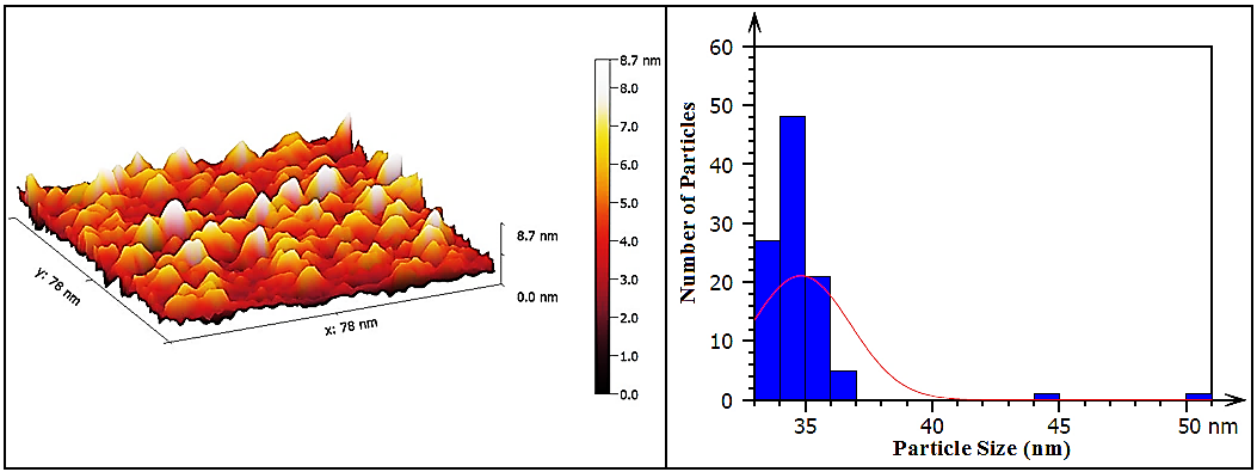

Figure (4.16): AFM and size distribution histograms images of SiC:AgO film with (5% AgO).

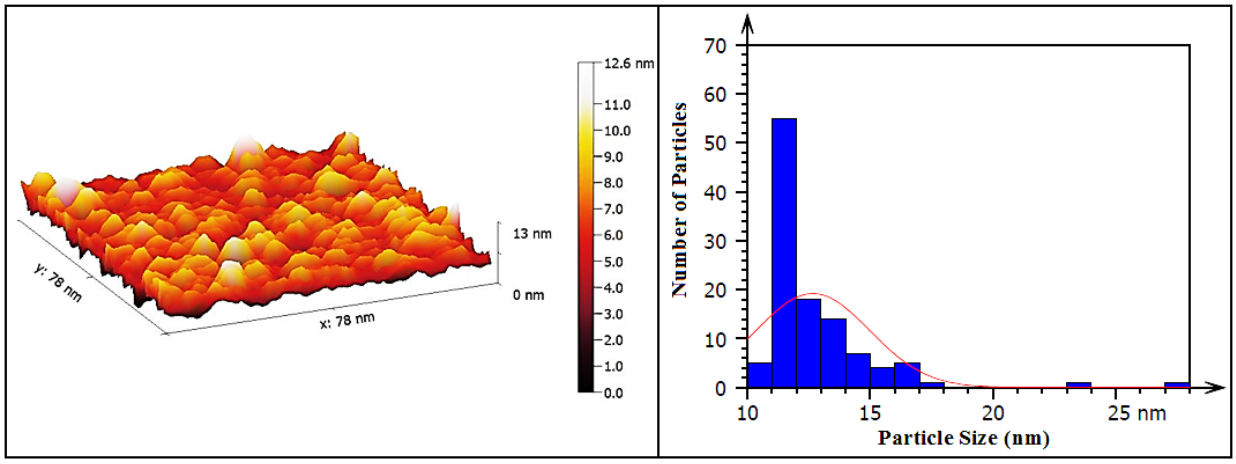

Figure (4.17): AFM and size distribution histograms images of SiC:AgO film with (7% AgO).

4.3 Optical Properties of SiC:Ag Thin Films

The study of the optical properties of the films is of great importance in finding the optical constants through which it is possible to know the value of the optical energy gap according to the specific preparation conditions (pressure, temperature, the thickness of the film, ... etc.) in addition to the possibility of knowing other optical constants **[**176].

4.3.1 Absorbance Spectrum

The optical absorbance spectrum of material depends on the energy of the incident photons, the type of material, and its crystal structure's nature [177].

Figure (4.18) shows the absorption spectrum as a function of the wavelength (λ) of SiC and AgO-doped SiC films within a range of wavelengths from (200 to 800) nm.

From figure (4.18), it is noted that the absorbance values of all the prepared films increase with the increase in the AgO ratios.

The results showed that the absorption edge for SiC film shifts towards the short wavelengths (blue shift) compared with the SiC bulk due to the quantum confinement phenomena. As for the SiC:AgO, the absorption edge has shifted towards the long wavelengths (red shift) because of the increase in the AgO ratios.

The figure shows that the absorbance spectra of the prepared films, begin to increase gradually with increasing the incident photons energy until it reaches its peak and becomes quasi-sharp when the energy of the incident photons becomes equal to or greater than the value of the optical energy gap of the prepared films.

All films have low absorbance in the visible and near-infrared regions. This can be explained as follows: for long wavelengths, incident photons do not have enough energy to interact with atoms onto the film's surface, so they are transmitted. When the wavelength of an incident photon decreases, the interaction between it and the material occurs, and the absorbance rises [99].The maximum absorption of the (SiC) and (1, 3, 5, and 7% AgO)wt were (0.171, 0.197, 0.336, 0.436 and 0.912).

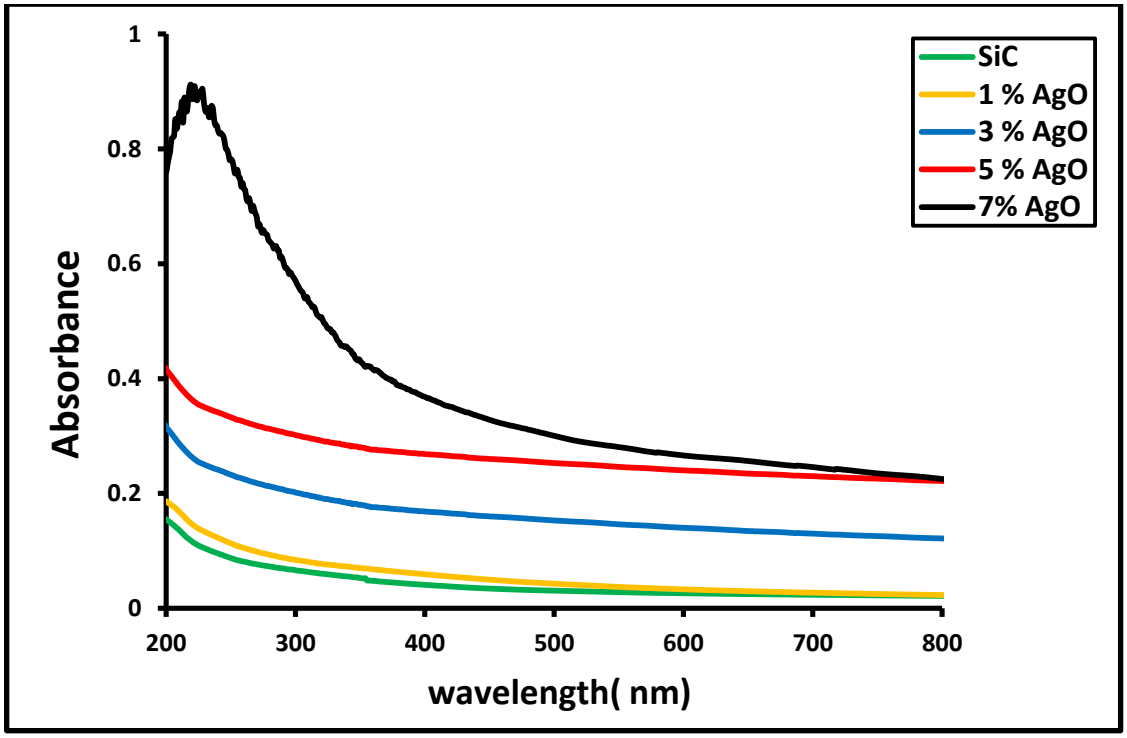

Figure (4.18): The optical absorbance spectra of SiC:AgO films with various dopant ratios of AgO.

4.3.2 Transmittance and Reflectance

The transmittance is is given by the relation (2.3). Reflectance is related to absorbance and transmittance and can be calculated using equation (2.12). Figures (4.19) and (4.20) show the transmittance and reflectance of SiC and SiC:AgO films as a function of the wavelength.

From Figure (4.19), it can note that the transmittance spectrum has the opposite behavior of the absorbance spectrum, where the transmittance of the films decreases with the increase in the AgO ratios. The transmittance spectrum of SiC:AgO films gradually decreases with the increase in the impurity ratios due to the localized levels that form within the forbidden energy gap between the valence and conduction band as a result of the presence of impurity atoms. The maximum transmittance of the SiC:AgO films were (0.9537, 0.953, 0.768, 0.609 and 0.621), respectively.

Also, it have been noted from the Figure (4.20), that an increase in the reflectance spectrum is due to an increase in the AgO ratios.

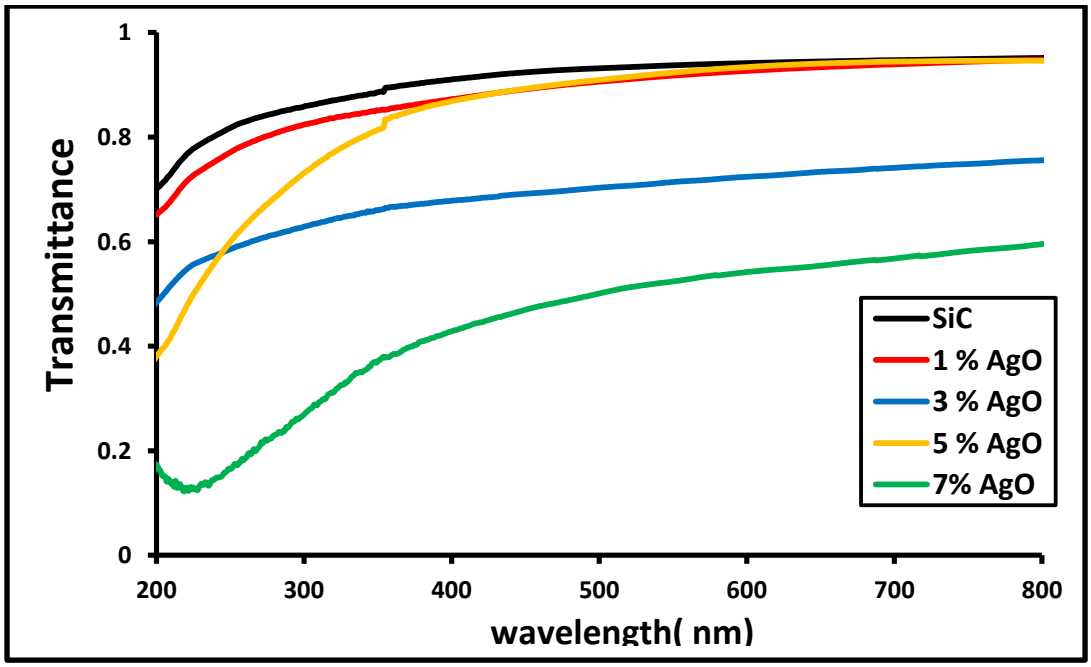

Figure (4.19): The optical transmission spectra of SiC:AgO films with various dopant ratios of AgO.

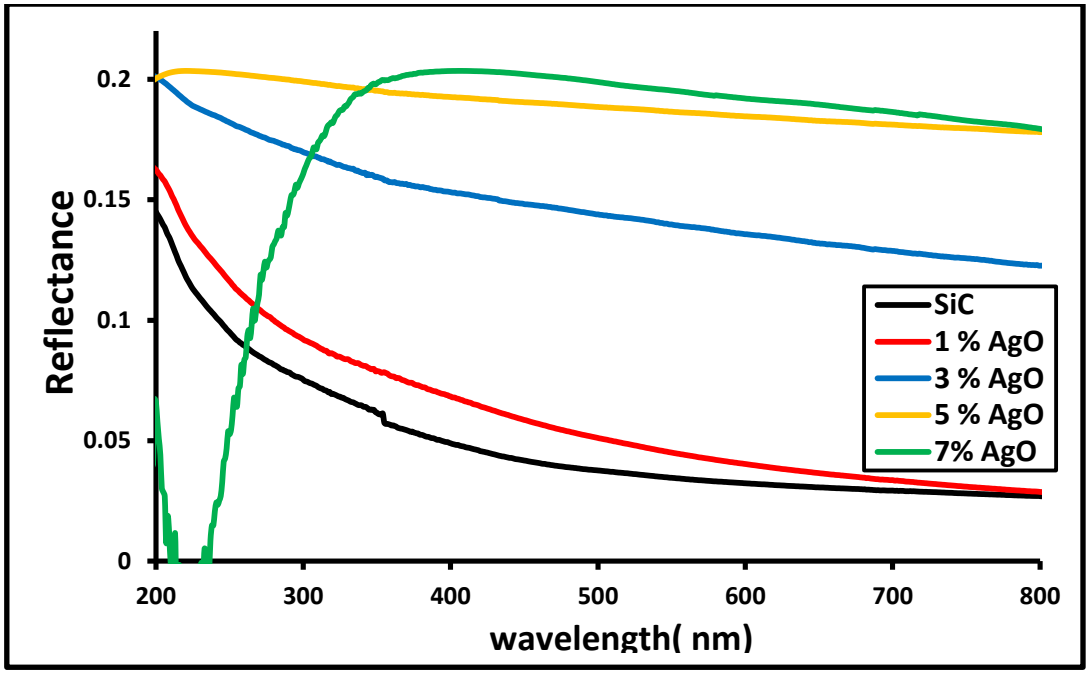

Figure (4.20): The Optical reflectance of SiC:AgO films with various dopant ratios of AgO.

4.3.3 Absorption Coefficient

The absorption coefficient (α) was calculated from the absorbance spectrum of the prepared films using the relation (2.20).

Figure (4.21) shows the absorption coefficient of SiC and SiC:AgO films as a function of the incident photon energy. From this Figure, it is noted that the absorption coefficient of the SiC and SiC:AgO films increase with the increase in the AgO ratios. It is seen from the above Figure that the absorption coefficient of the SiC:AgO films increases with the increase in the AgO ratios and that the absorption coefficient behaves similarly to the absorption spectrum and this could be attributed to the nature of the relation between them according to eq.(2.20).

The values of the absorption coefficient increase when approaching the ultraviolet region while all films have low absorption coefficients in the visible and near-infrared regions due to the same reason mentioned in the absorption spectrum. The maximum absorption coefficients of the SiC:AgO films were (1970.1, 2270.5, 3869.4, 5020.8 and 9495) cm^{-1} for the SiC, 1%, 3%, 5% and 7%, respectively.

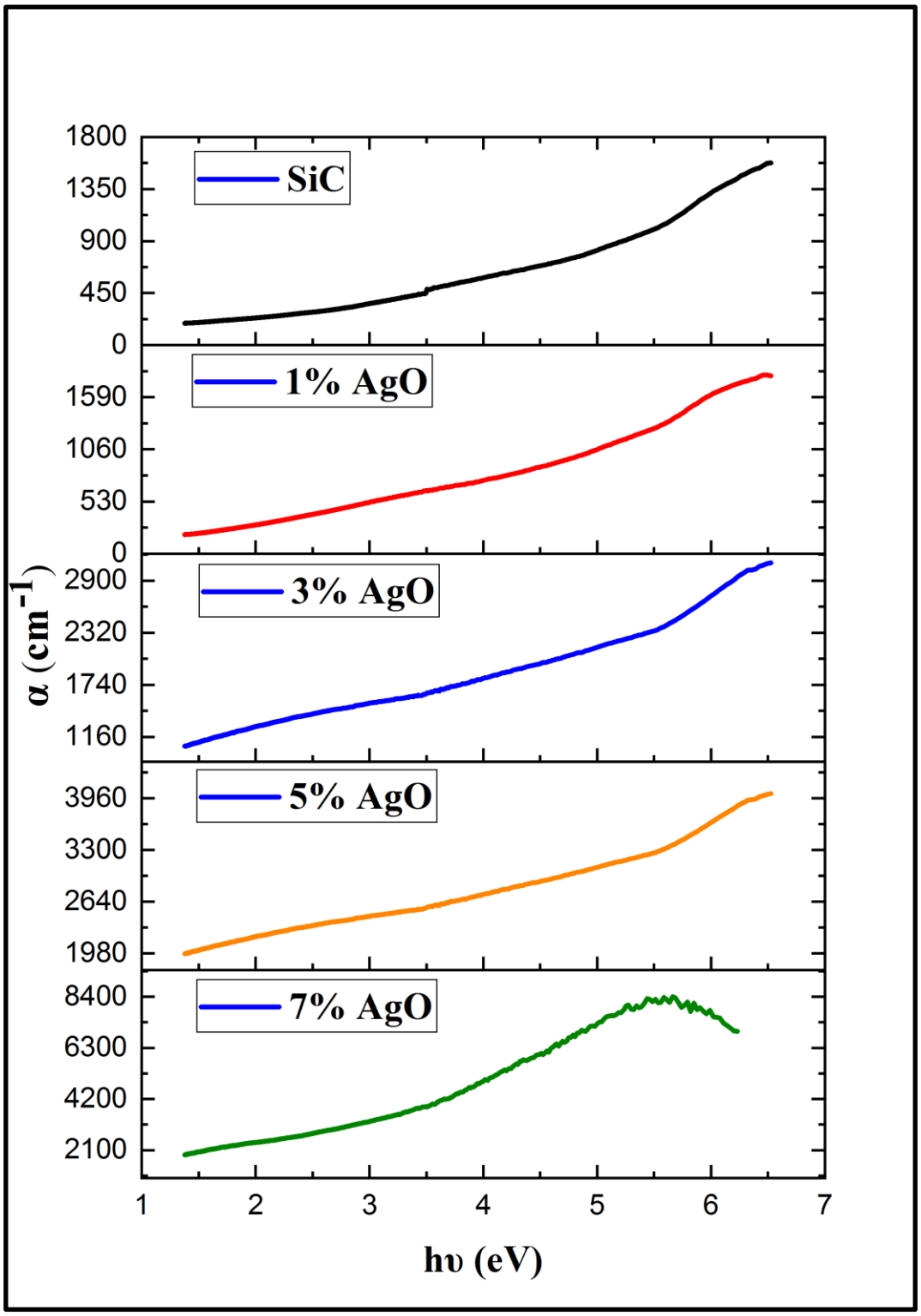

Figure (4.21): The absorption coefficient of SiC:AgO films with various dopant ratios of AgO.

4.3.4 Optical energy gap

The optical energy gap (E_g) of the SiC:AgO films was calculated for the indirect electronic transitions using the equation (2.18).

Figure (4.22) show the photon energy of prepared films as a function of the $(\alpha h\nu)^{1/2}$. It can be seen from figure (4.22) that the energy gap values of SiC:AgO films decrease with the increase of the AgO doping ratios. This decrease in the energy gap is attributed to the fact that the higher doping results in additional levels in the energy gap due to the incorporation of impurities with energy levels close to the edge of the gap which causes a decrease in the inclination $(\alpha h\nu)^{1/2}$ with $(h\nu)$ and thus reducing of the energy gap. The obtained energy gap values are listed in Table (4.5).

Table (4.5): Energy gap values of SiC and AgO-doped SiC thin films.

Samples	E_g (eV)
SiC	2.61
1% AgO	2.38
3% AgO	2.18
5% AgO	2.10
7% AgO	2

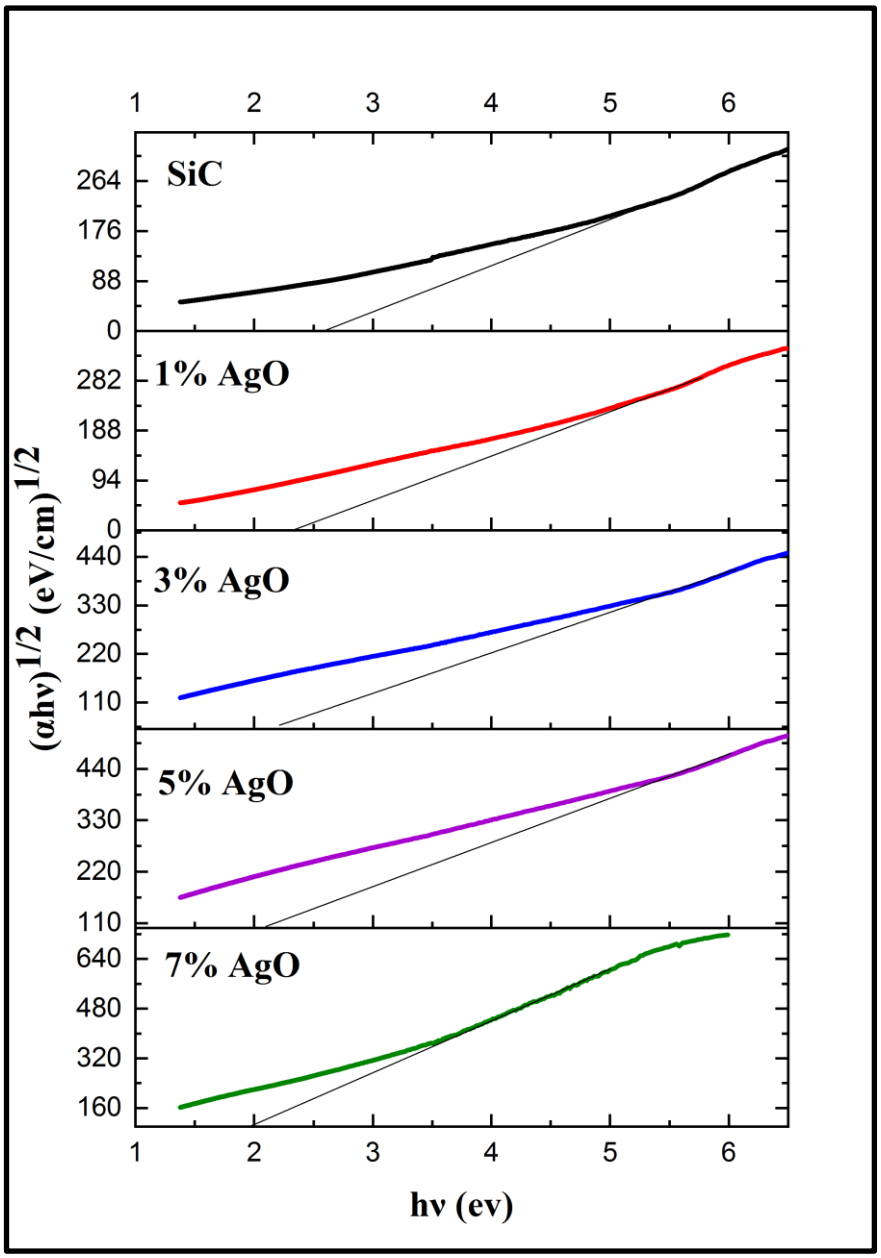

Figure (4.22): The optical energy gap of SiC:AgO films with various dopant ratios of AgO.

4.3.5 Extinction Coefficient

The extinction coefficient (k_o) indicates the electromagnetic wave's attenuation as it passes through the medium, and its value can be found from the equation (2.21).

Figure (4.23) shows the change of the extinction coefficient as a function of the wavelength of the SiC and AgO-doped films. The nature of the extinction coefficient curves is almost similar to the behaviour of

the absorption coefficient curves due to the same behaviour illustrated by eq.(2.21).

For the 7% AgO sample, it can be noted that the values of the extinction coefficient decrease after the fundamental absorption edge, then increase when approaching the visible wavelengths. It is also noted that the extinction coefficient values gradually decrease with the decrease in the doping ratios. The maximum extinction coefficient of the SiC:AgO films were (0.029, 0.035, 0.095, 0.177 and 0.189) for the SiC, 1%, 3%, 5% and 7%, respectively.

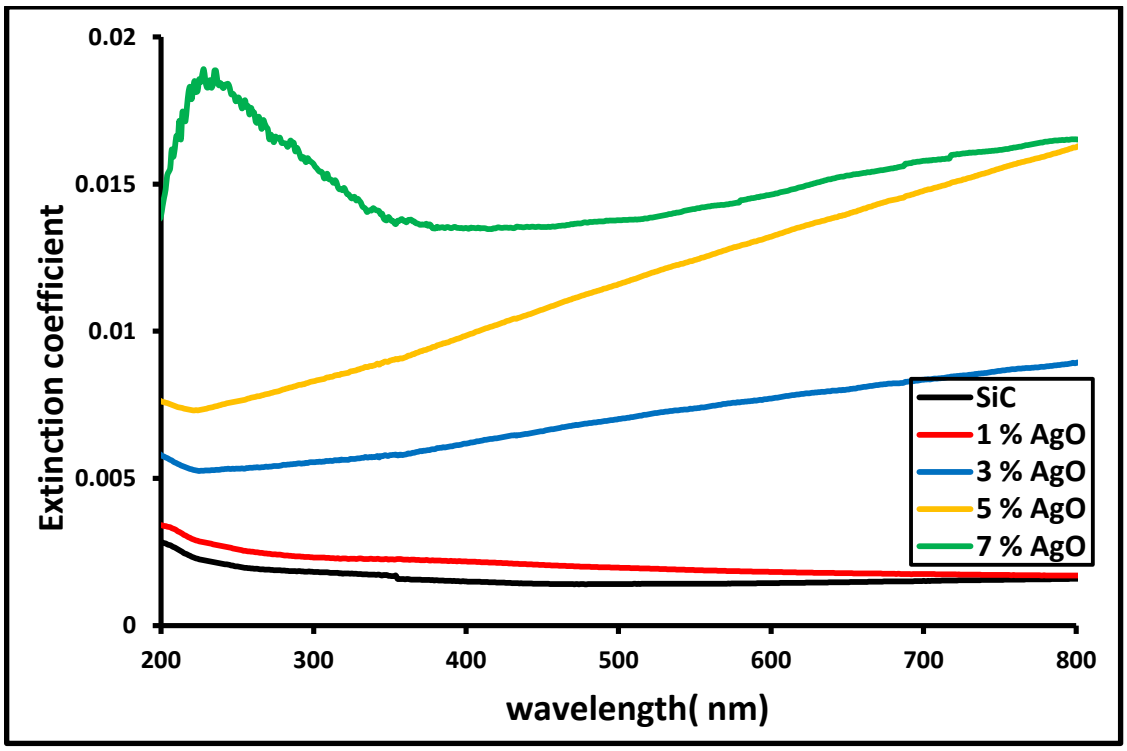

Figure (4.23): The extinction coefficient of SiC:AgO films with various dopant ratios of AgO.

4.3.6 Refractive Index

The refractive index (*n*) is related to film reflectance and extinction coefficient according to equation (2.24).

Figure (4.24) shows the refractive index change as a function of the wavelength. It can note that the nature of the refractive index curve is almost similar to the nature of the reflection curve due to its relation to

the refractive index. The refractive index changes from (2.229) to (2.785) with an increase in the AgO ratios.

The refractive index of a 7% AgO film increases when approaching the fundamental absorption edge and then gradually decreases at the visible and near-infrared wavelengths.

The increase in the AgO ratios of the prepared films has led to an increase in the refractive index of the films in the ultraviolet region, and this may attribute to the rise in the secondary energy levels formed in the forbidden gap, which in turn act as scattering centers for the incident rays, as a result, the reflectance increases, and thus the refractive index increases according to eq.(2.24).

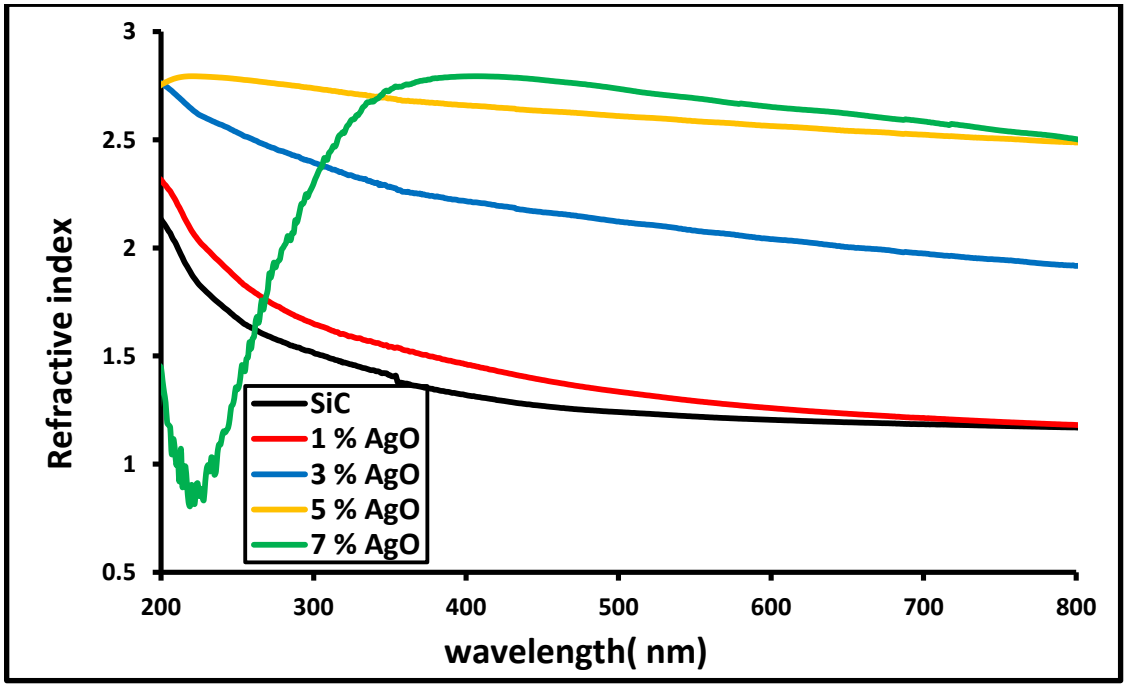

Figure (4.24): The refractive index of SiC: AgO films with various dopant ratios of AgO.

4.4 The Electrical Properties of SiC:AgO Thin Films

The electrical properties of SiC and AgO-doped SiC thin films deposited on glass substrates will be presented. These properties include the Hall effect, which gives information about carriers' type, density, and mobility.

4.4.1 Hall Effect Measurements

Table (4.6) illustrates the main parameters estimated from Hall effect measurements for prepared thin films. The results have revealed that the Hall constant is negative, indicating that all samples examined are of n-type. The results show that the highest value for the concentration of charge carriers was (19.3×10^{14} cm^{-3}) for the SiC sample and the lowest value was (5.87×10^{14} cm^{-3}) for the (1% AgO) sample. It also note that the mobility of carriers ranges between 19.14×10^4 ($cm^2\ V^{-1}\ s^{-1}$) for the (1% AgO) sample as the highest value and 6.53×10^4 ($cm^2\ V^{-1}\ s^{-1}$) for the SiC sample as the lowest value. The decrease in the concentration of mobility of charge carriers with the increase in the doping ratios may be attributed to the scattering of electrons by impurity atoms and the scattering of some free carriers as a result of thermal vibrations of the lattice.

Table (4.6): Hall parameters for SiC and AgO-doped SiC thin films.

Samples	$n \times 10^{14}$ $(cm)^{-3}$	$R_H \times 10^3$ $(cm^{-3}.C^{-1})$	$\mu \times 10^4$ $(cm^2\ V^{-1}\ s^{-1})$	ρ (Ω.cm)	σ $(\Omega.cm)^{-1}$	Type
SiC	-19.3	-3.24	6.532	0.0496	20.177	n
1% AgO	-5.87	-10.6	19.144	0.0555	18.018	n
3% AgO	-6.89	-9.06	18.318	0.0495	20.209	n
5% AgO	-6.91	-9.03	17.136	0.0527	18.974	n
7% AgO	-6.89	-9.06	17.039	0.0532	18.806	n

4.5 I-V Characteristics of SiC:AgO/p-Si Heterojunction in Light and Dark.

In this section, the current-voltage measurements have been used to determine the electrical properties of SiC and AgO-doped SiC films. The study of current-voltage properties in the dark and light case is important because it clearly indicates the possibility of using SiC films as a photosensor. Figure (4.25) shows (I-V) characteristics for SiC:AgO/p-Si heterojunction under light with various AgO content (1, 3, 5 and 7 AgO) wt% for forward and reverse bias voltages where the effect of light is clearly in changing the current values for prepared samples. From this Figure, it can observe that the values of photocurrent increase with an increase in the applied voltage in the light case which is attributed to the increase of the charge carriers. Therefore, the current flow across the junction will be increased.

The highest value of the forward current was (327, 2360, 155, 1626 and 3600 μA) for the (SiC) and (1, 3, 5, and 7 AgO) wt% samples respectively. This increase in the photocurrent values is due to the addition of AgO atoms doping with different ratios to SiC material, thus improving its electrical properties. The importance of photocurrent of the SiC and 3% AgO samples remains almost constant and then increases when the applied voltage reaches about 3 volts. It can be seen from this Figure also that the curve exhibits a non-linear feature, indicating that the conduction mechanism is non-ohmic.

For the SiC:AgO/p-Si heterojunction under illumination at reverse bias, the width of the depletion region increases with the increase of the applied voltage which leads to an increase in the absorption through it and the creation of the electron-hole pairs.

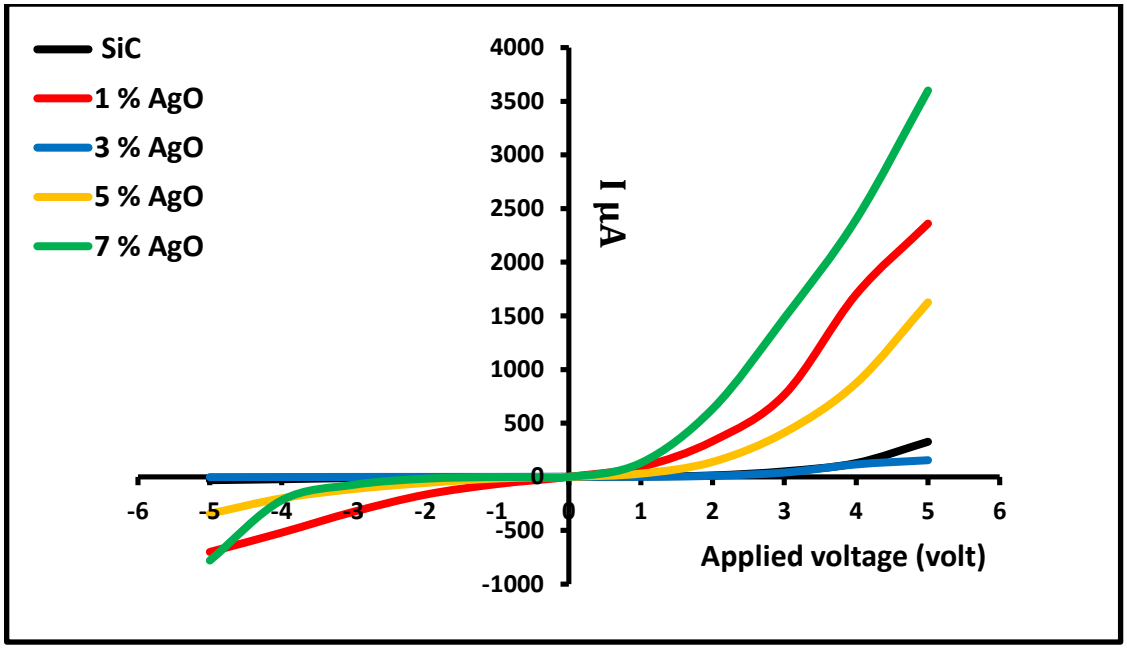

Figure (4.25): I-V Characteristics in light of SiC:AgO/p-Si heterojunction at forward and reverse bias with various dopant ratios of AgO.

Figures (4.26- 4.30) exhibit the reverse current as a function of applied voltage in dark and light for SiC:AgO/p-Si heterojunction. The results showed that the values of current increase with the increase of the applied reverse voltage due to the change in doping ratios and this behavior are similar to what we observed in the forward bias.

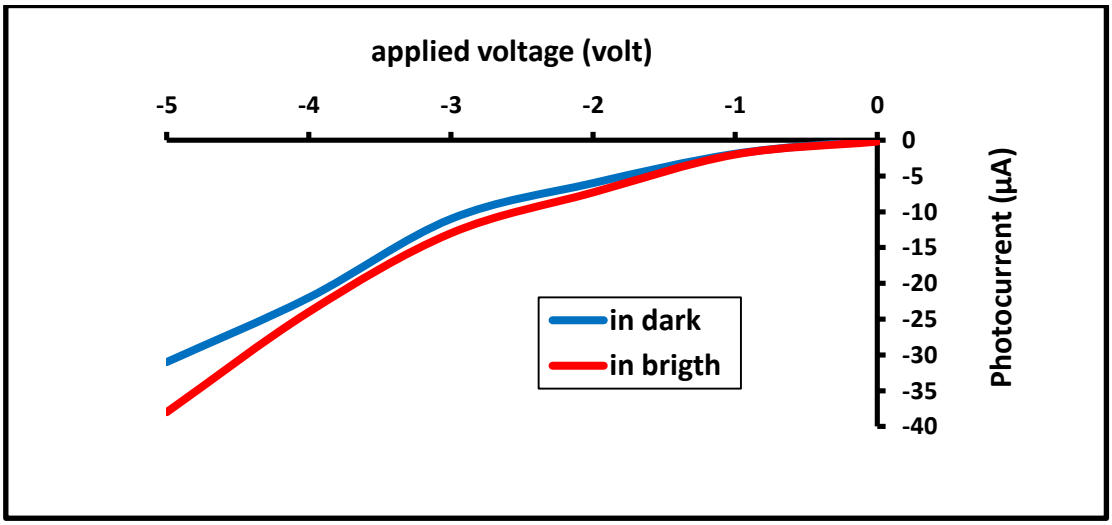

Figure (4.26): I-V Characteristics under dark and light of SiC/p-Si heterojunction at reverse bias.

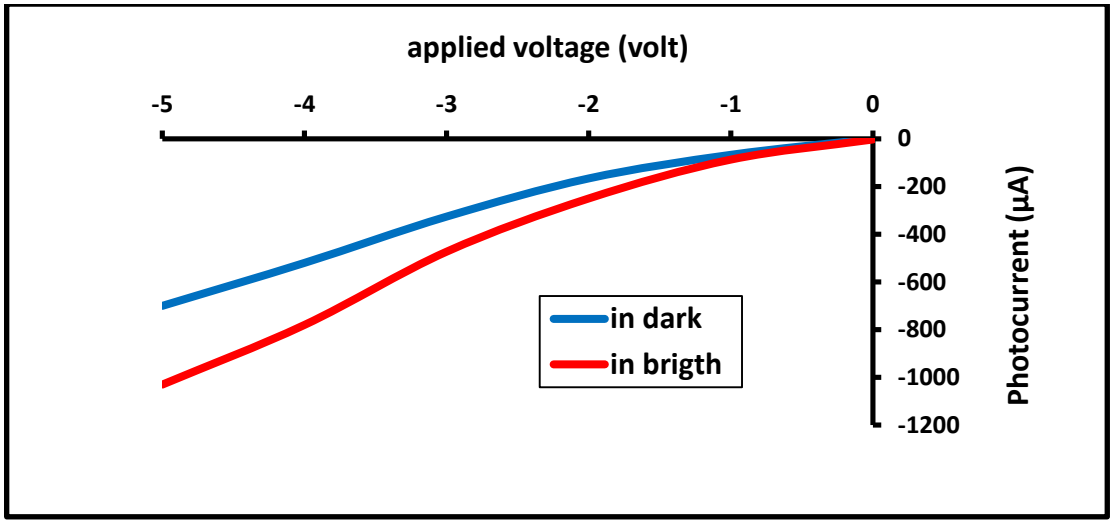

Figure (4.27): I-V Characteristics under dark and light of SiC:AgO/p-Si heterojunction at reverse bias (1% AgO).

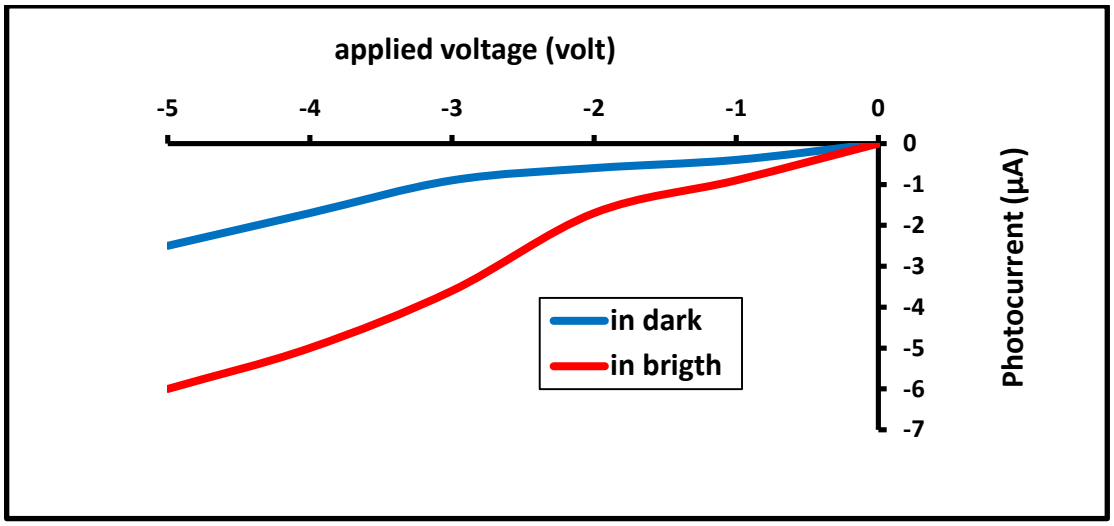

Figure (4.28): I-V Characteristics under dark and light of SiC:AgO/p-Si heterojunction at reverse bias (3% AgO).

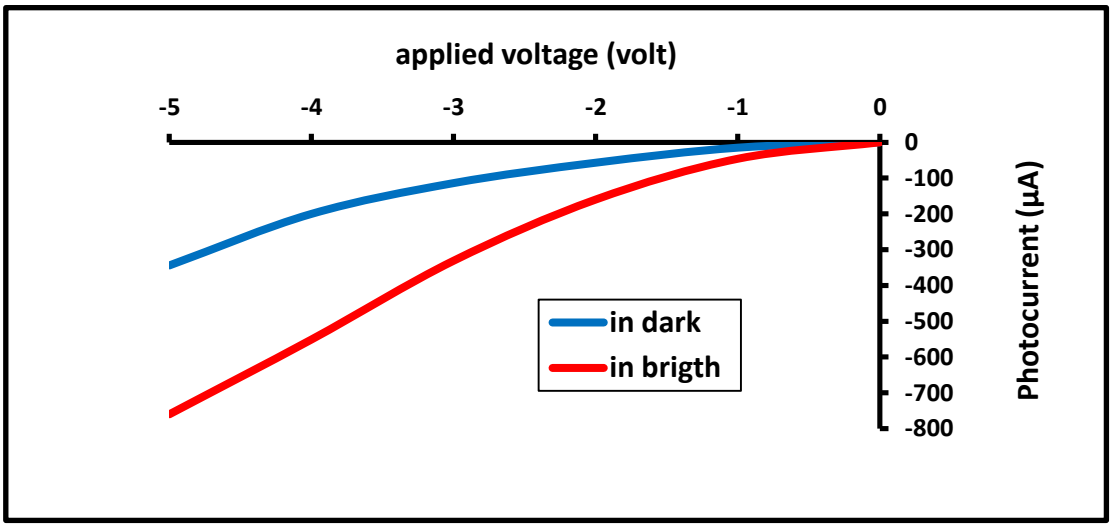

Figure (4.29): I-V Characteristics under dark and light of SiC:AgO/p-Si heterojunction at reverse bias (5% AgO)

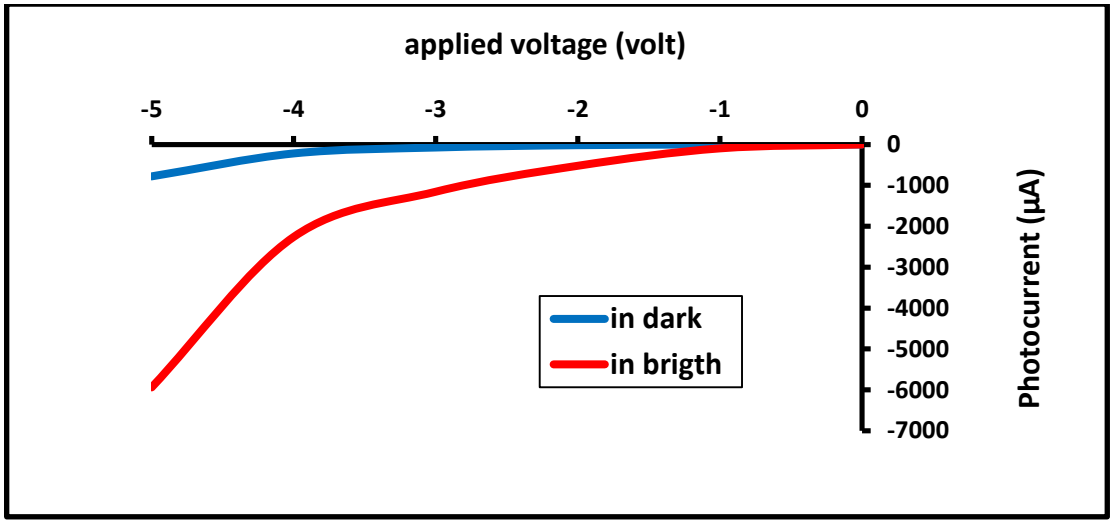

Figure (4.30): I-V Characteristics under dark and light of SiC:AgO/p-Si heterojunction at reverse bias (7% AgO).

The values of solar cell parameters of (V_{oc}, I_{sc}, V_{max}, I_{max}, F.F and η) of SiC: AgO/p-Si heterojunction were arranged in Table (4.7). The fill factor and efficiency can be calculated from equations (2.34) and (2.35) respectively. In general, it can be observed that the maximum efficiency value was (0.165 %) for (7% AgO) sample, while the lowest value was (0.005 %) for (1% AgO) sample.

Table (4.7): Measured and calculated values of SiC: AgO/p-Si heterojunction.

Sample name	V_{oc} (mV)	I_{sc} (mA)	V_{max} (mV)	I_{max} (mA)	F.F	η%
SiC	116	0.0007	11.5	0.0004	0.06	0.0096
1% AgO	59	0.0003	24	0.0001	0.14	0.005
3% AgO	101	0.0048	15.3	0.0005	0.02	0.016
5% AgO	146	0.0011	26	0.0005	0.08	0.0271
7% AgO	112	0.0046	61	0.0013	0.15	0.165

4.6 Gas Sensing Measurements of SiC:AgO Thin Films

The effect of changing doping ratios (1, 2, 3, and 7 AgO) wt% and operating temperature (25, 60, 100, 200, 250 and 300℃) on improving sensor characteristics (sensitivity, response time, and recovery time) was studied. The response and recovery times are determined through the time that it takes for the sensor to experience (10-90)% of the steady-state resistance when the target gas/air is introduced [178, 179].

4.6.1 Influence of the Operating Temperature

The temperature has pronounced effects on the sensitivity of thin-film gas sensors, as it influences the physical properties of semiconductors (change of the free carrier concentration, Debye length). In this way, dynamic properties of the sensors such as response and recovery time and the static characteristics of the sensor depend on the temperature of operation, and a temperature for which the sensitivity of a semiconductor gas sensor is maximum always observed.

Different possible temperature-dependent elementary steps of molecular recognition with semiconductor gas sensors have to be optimized to detect a specific molecule. These steps firstly involve the low-temperature surface reactions. Examples are adsorption and catalytic reactions at active sites (the latter involving intrinsic point defects, such as (O^2) vacancies, and/or extrinsic point defects, e.g., segregated metal atoms) and similar reactions at grain boundaries or three-phase boundaries (e.g., at metallic contacts or surface metallic clusters). All of these reactions involve adsorbed negatively charged molecular (O^{2-}) or atomic (O^-) species as well as hydroxyl groups (OH^-) at different surface sites. Secondly, these steps involve the high-temperature bulk reactions between point defects in the SiC crystal and oxygen (O^2) in the gas phase. The key to the controlled operation of such sensors is the careful

adjustment of the operation temperature since conduction changes upon exposure to different gas components, usually showing different maxima as a function of temperature.

Figures (4.31) and (4.32) exhibit the sensitivity of SiC and AgO-doped SiC with various AgO ratios (1, 3, 5, and 7 AgO) wt% as a function of operating temperature in the range (25-300℃) with pulse laser deposition which is deposited on p-type Si substrates at 5 % NO_2:air mixing ratio and 10 % NH_3:air mixing ratio on the all samples.

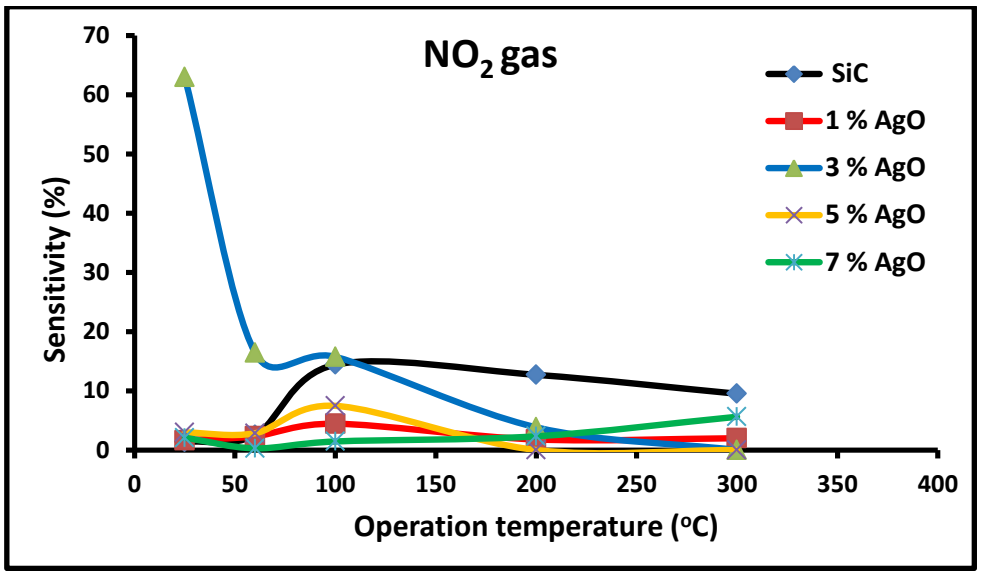

Figure (4.31): Sensitivity as a function of the operating temperature of SiC doped with AgO on a silicon substrate using NO_2 as a gas sensing technique.

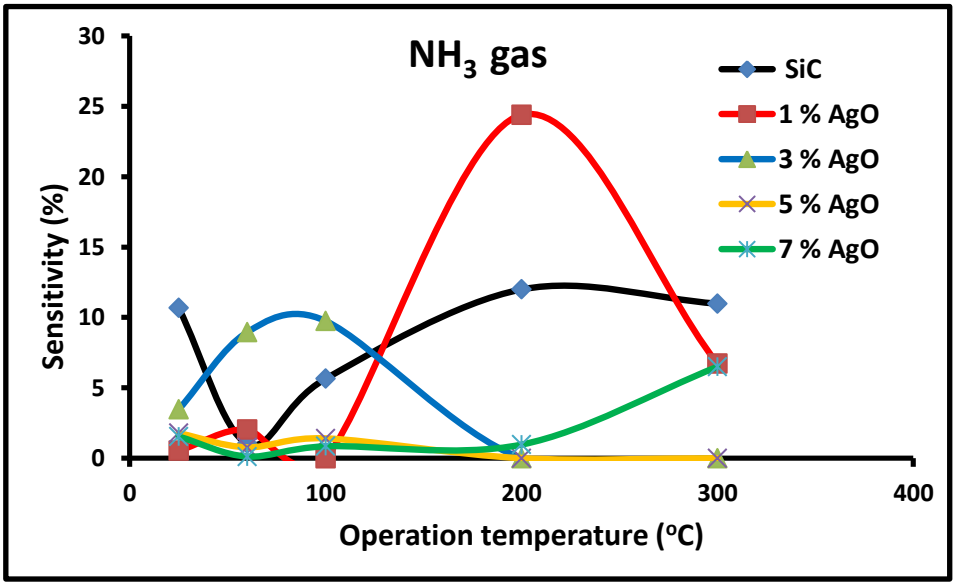

Figure (4.32): Sensitivity as a function of the operating temperature of SiC doped with AgO on a silicon substrate using NH_3 as a gas sensing technique.

The effect of the operation temperature on thin films sensitivity is studied to optimize the operating temperature to the lowest possible value. The operating temperature is defined as the temperature at which the sensor's resistance reaches a constant value. The changing of resistance is only influenced by the presence of some gases of interest [178, 179].

The results show that the sensitivity has slowly increased with increasing operating temperature. The sensitivity of samples when working at room temperature to (100℃) has regular behaviour, while the sensitivity is irregular when the operating temperature is up to (200-300℃). For these reasons, the AgO-doped SiC samples cannot record sensing signals up to (200℃).

The maximum sensitivity of the tested gas sensor to (40 ppm) of NO_2 is about (62.9%) at around (25℃) for 3% AgO-doped SiC, while the 7% AgO-doped SiC gas sensor has (0.8%) lowest sensitivity to NO_2. It should also be noted that the optimum sensing temperature required for the maximum sensitivity is around (100℃) for the AgO-doped SiC gas sensor.

When NH_3 is used as the probing gas, the maximum sensitivity of the samples gas sensor to (50 ppm) of NH_3 can reach (24.38%) for 1% AgO-doped SiC, and the optimum sensing temperature of the sensor is around (25-100℃).

The above results have shown that the sensitivities to the oxidizing and reducing gases have been greatly enhanced. The reason can be attributed to the nano-sized SiC particle on the silicon substrate and the increased amount of surface adsorbed oxygen species.

It can also be noted that the samples that have AgO-doped SiC with respect to SiC have enhanced sensitivity at room temperature to the oxidizing NO_2 and reducing NH_3 gases, as is evident in the figures.

This result could be attributed to the fact that AgO has a lower energy gap than SiC.

Figures (4.33) and (4.34) show the sensitivity variation as a function of operation temperature for SiC:AgO gas sensor on glass substrate for NO_2 and NH_3 gases.

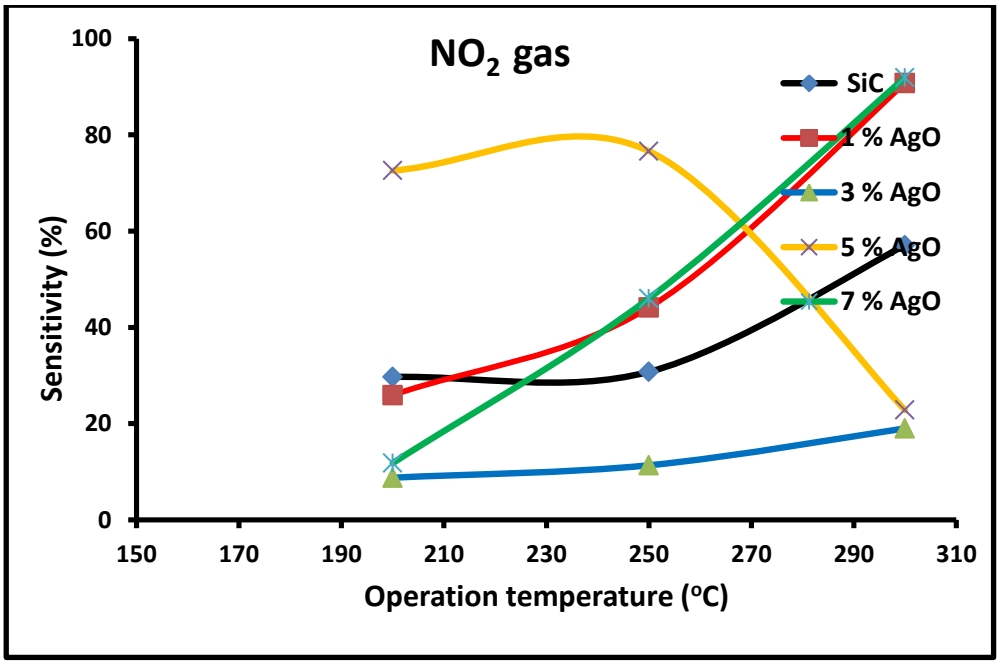

Figure (4.33): Sensitivity as a function of the operating temperature of SiC doped with AgO on a glass substrate using NO_2 as a gas sensing technique.

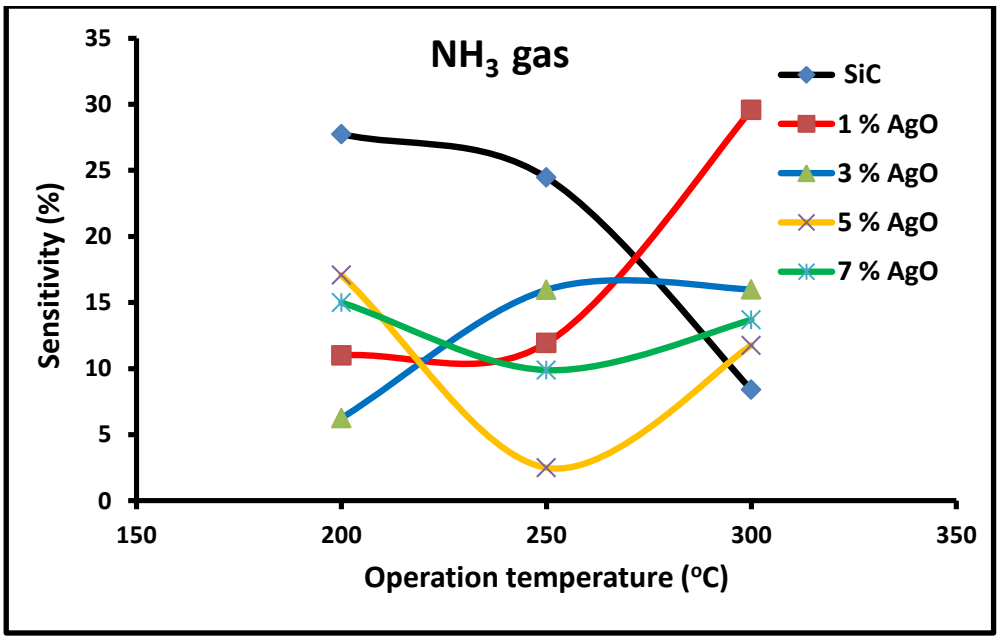

Figure (4.34): Sensitivity as a function of the operating temperature of SiC doped with AgO on a glass substrate using NH_3 as a gas sensing technique.

Figure (4.33) shows that the higher sensitivity for 50 ppm NO_2: air mixed ratio for temperature up to (300℃) was about (90.769%) and (91.8%) for 1% AgO and 7% AgO-doped SiC gas sensor while the maximum sensitivity for to 40 ppm NH_3 test gas shown in figure (4.34) to (300℃) was about (29.565%) for 1% AgO-doped SiC gas sensor. It should also be noted that the optimum sensing temperature required for the maximum sensitivity is around (250℃) for all SiC gas sensors.

As can be seen from these four figures, the SiC samples deposited on a silicon substrate have higher conductance than the SiC samples deposited on a glass substrate. The higher conductance of SiC samples makes these samples work at low temperatures than the samples deposited on the glass substrate. On the other hand, the silicon substrate form conducting layer with SiC film, making distortion in the sensor single, where, and the glass substrate has seen this distortion.

All the above results have shown that the sensitivities of SiC gas sensors to oxidizing and reducing gases have been greatly enhanced. The reason can be attributed to the nano-sized SiC particle on the glass substrate, and the increased amount of surface adsorbed oxygen species.
When the particle size of SiC is small enough, especially the grain size is comparable to the depth of the sub-surface depletion layers, the whole resistance and sensitivity of the SiC sensor are controlled by the grains themselves, inducing an inverse relationship between particle size and gas sensitivity, with the smaller particle producing higher sensitivity. The higher sensitivity may be attributed to the optimum surface roughness, porosity, large surface area and large rate of oxidation or reduction of the sensor.

4.6.2 Response Time and Recovery Time

Figures (4.35) to (4.38) show the relationship between the response time and the recovery time as a function of the operating temperature. Figures (4.35) and (4.36) show that the response time decrease with rising operating temperature for NO_2 and NH_3 test gases. The fastest response time for NO_2 gas (13.5 s) for 3% AgO sample at (100℃) and (13.5 s) for 7% AgO sample at (100℃) for NH_3 gas. At the same time, figures (4.37) and (4.38) show that the recovery time decrease with rising operating temperature for NO_2 and NH_3 test gases. The fastest recovery time for NO_2 gas was (30.6 s) for SiC sample at (200℃) and (33.3 s) for NH_3 gas for SiC sample at (100℃).

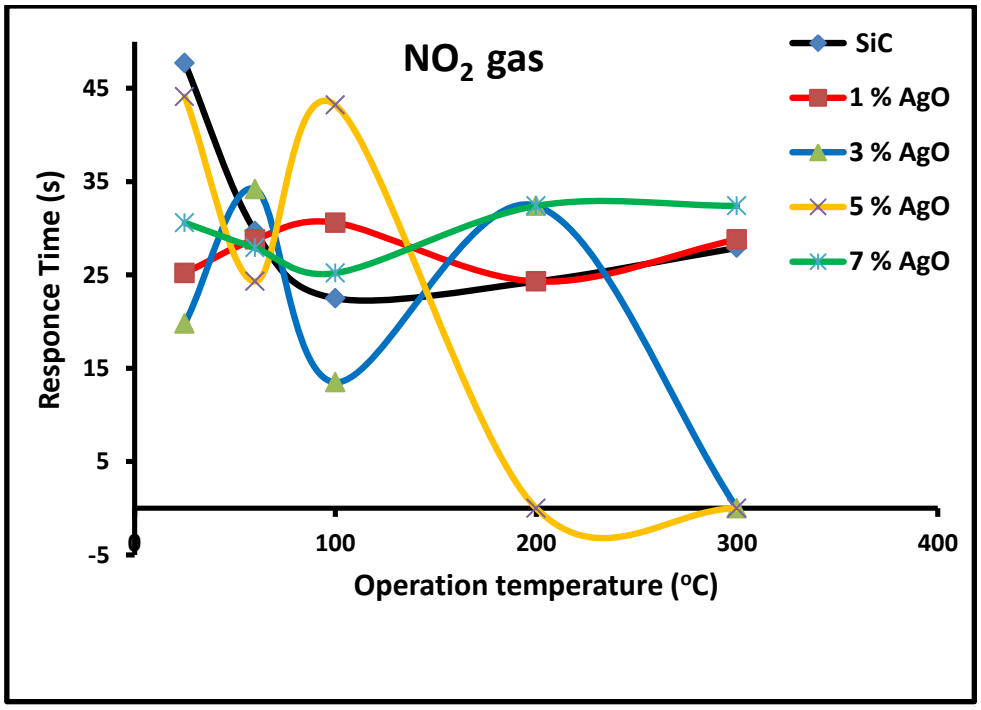

Figure (4.35): Response time as a function of the operation temperature of the SiC:AgO/Si gas sensor using NO_2 gas.

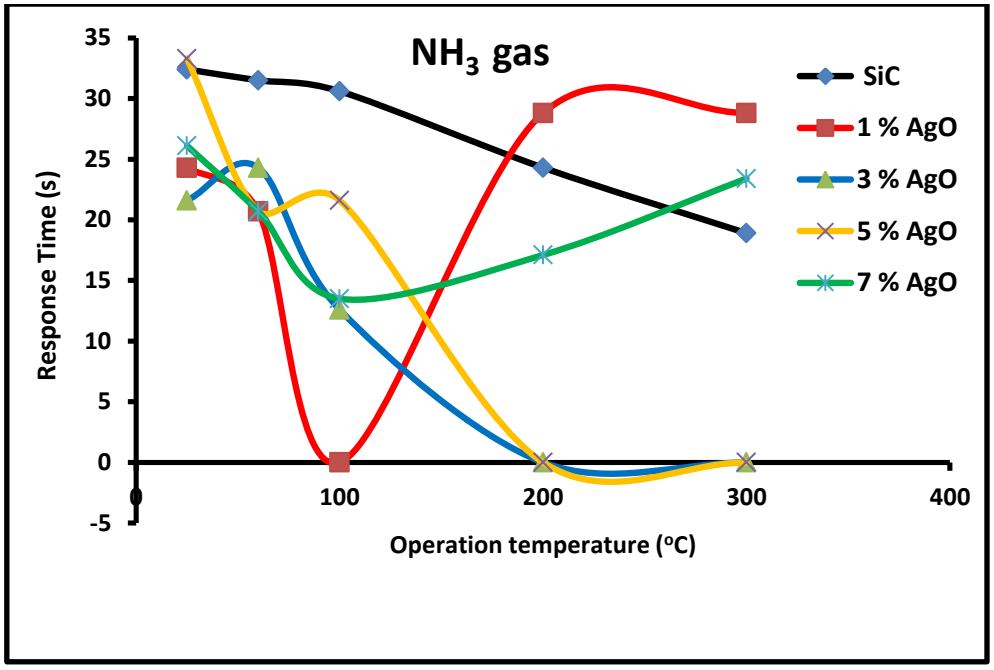

Figure (4.36): Response time as a function of the operation temperature of the SiC:AgO/Si gas sensor using NH_3 gas.

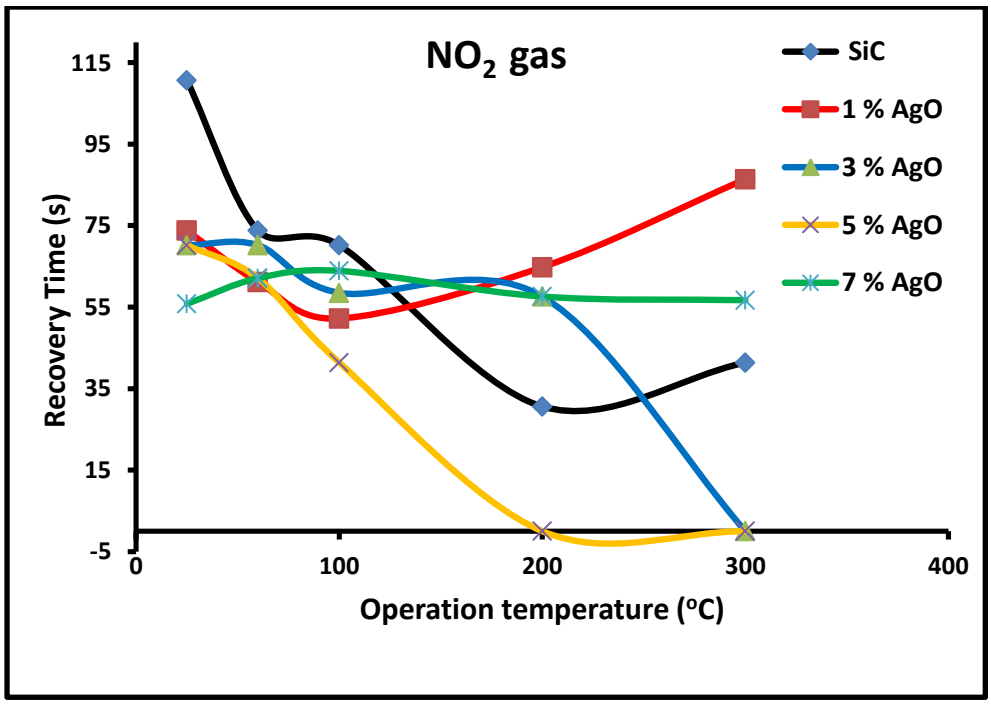

Figure (4.37): Recovery time as a function of the operation temperature of the SiC:AgO/Si gas sensor using NO_2 gas.

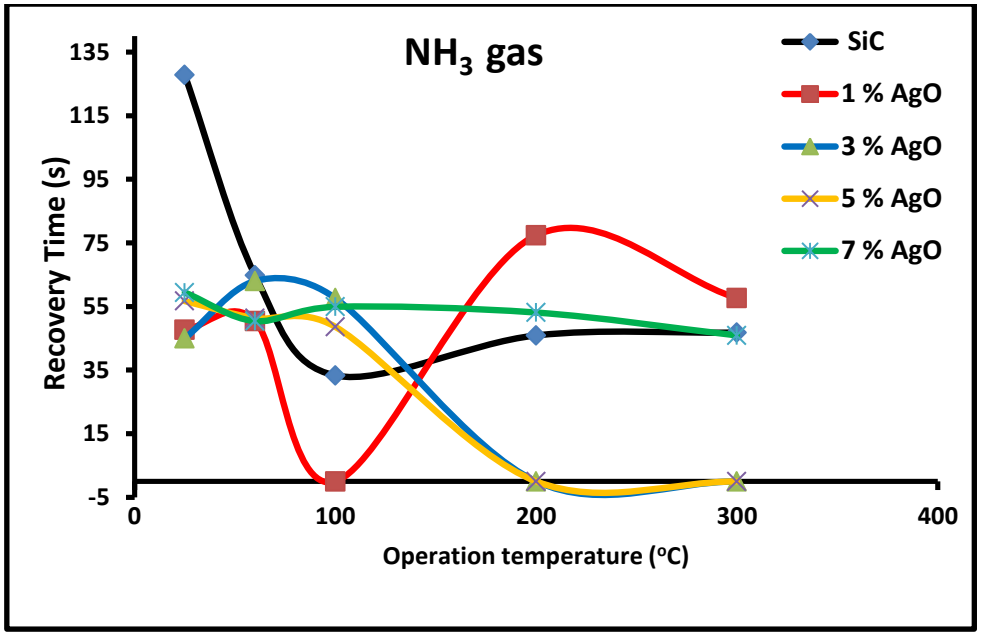

Figure (4.38): Recovery time as a function of the operation temperature of the SiC:AgO/Si gas sensor using NH_3 gas.

Figures (4.39) to (4.42) show the relationship between the response time and the recovery time of the SiC:AgO/glass gas sensor with operating temperature. Figures (4.39) and (4.40) show that the response time decrease with rising operating temperature for NO_2 and NH_3 test gases. The fastest response time for SiC sensor was (6.3 s) for NO_2 gas and (11.7 s) for NH_3 gas at (250℃) and (300℃), respectively.

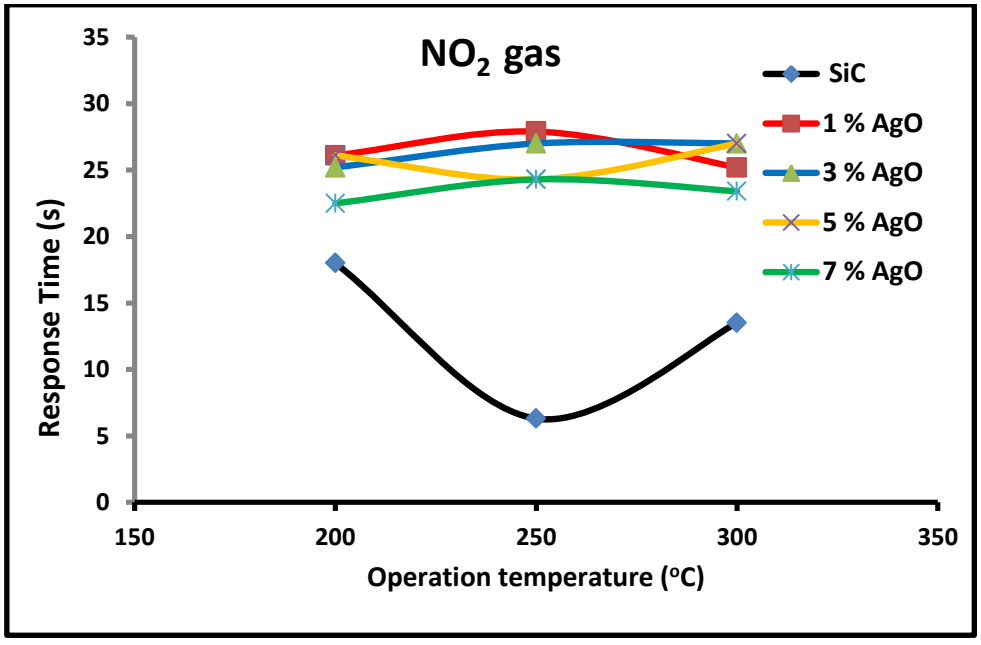

Figure (4.39): Response time as a function of the operation temperature of the SiC:AgO/glass gas sensor using NO_2 gas.

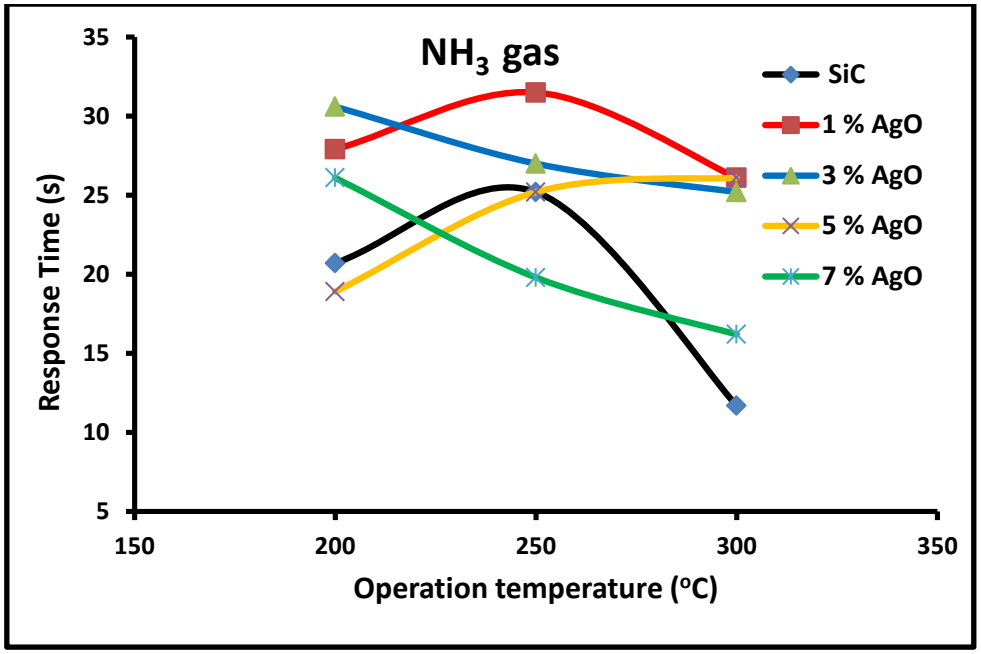

Figure (4.40): Response time as a function of the operation temperature of the SiC:AgO/glass gas sensor using NH_3 gas.

The figures (4.41) and (4.42) show that the recovery time decrease with increasing operating temperature for NO_2 and NH_3 test gases. The fast recovery time for NO_2 gas is equal (42.3 s) for 1% Ag-doped SiC sample at (200℃) and (34.2s) for NH_3 gas for 1% AgO-doped SiC sample at (250℃).

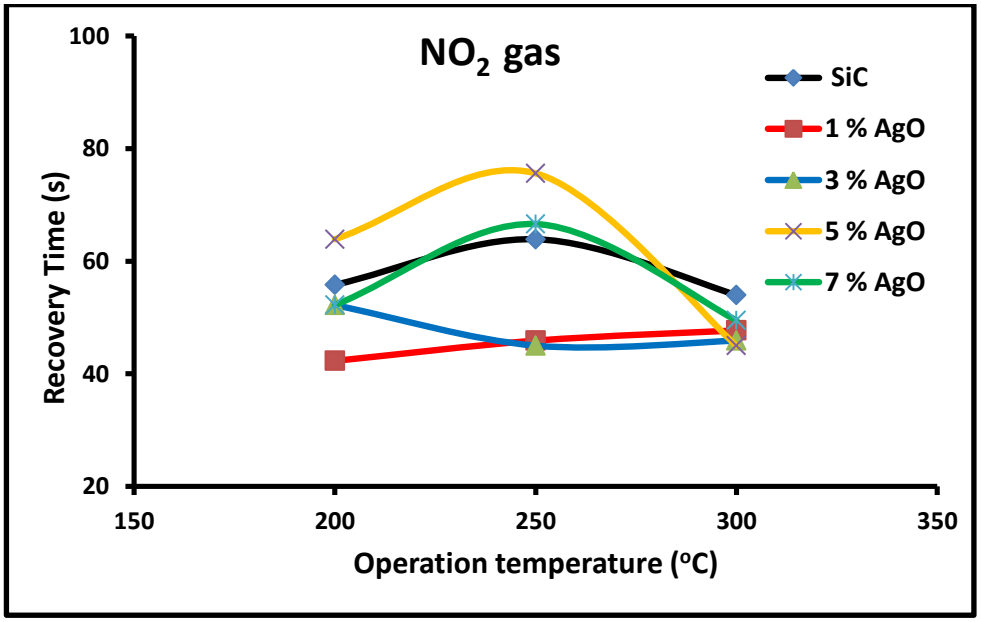

Figure (4.41): Recovery time as a function of the operation temperature of the SiC:AgO/glass gas sensor using NO_2 gas.

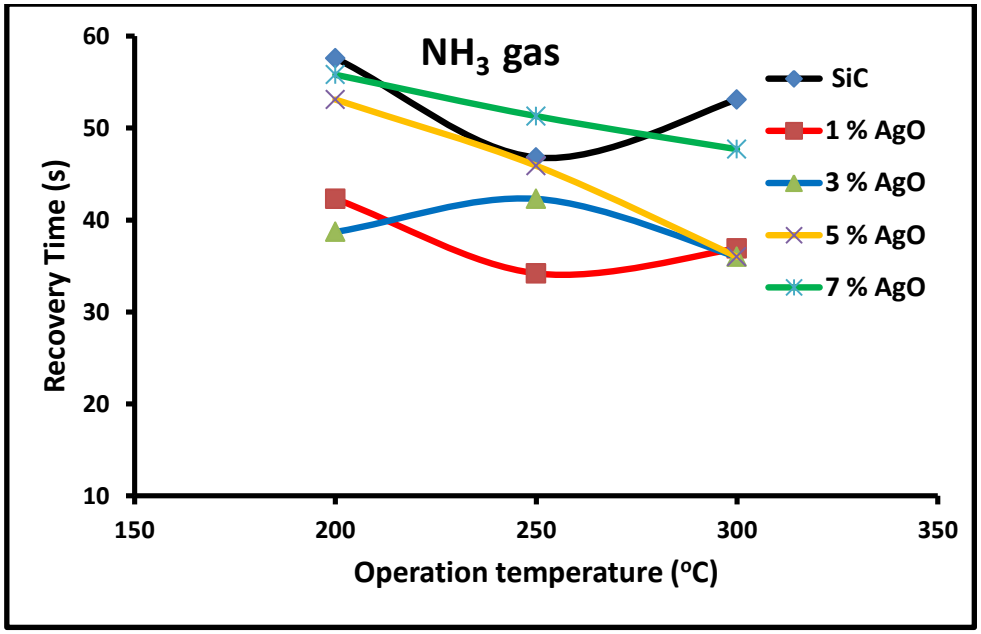

Figure (4.42): Recovery time as a function of the operation temperature of the SiC:AgO/glass gas sensor using NH_3 gas.

The particular reduction in the work function and the activation energy of surface reaction may be associated with decreasing grain size and an increase in vacancies created upon SiC lattice [180].

The increased oxygen adsorption on the surface extracts conduction electrons from the near-surface region forming an electron depleted surface layer. That increased number of active adsorption sites achieved a fast response time for sensors. In general, the response time and recovery time are decreases when increasing the operating temperature, as shown in the previous figures. In real situations, a fast response time is usually required and a fast recovery time.

4.6.3 Sensing Mechanism

Figures (4.43) to (4.52) show the variation of resistance with a time of SiC and AgO-doped SiC sensor for silicon and glass substrates as exposed to 5 % NO_2 and 10 % NH_3 in the air ambient injected into the testing chamber. The bias voltage is keeping at (3V), at an optimal operating temperature of each sample. The resistance is measured directly with time and the sensor resistance initially reaches the steady-state

before gas opening, at this time the gas is opened to allow mixing with air inside the chamber. The resistance decreases abruptly to reach a steady-state then we switch the gas off. Then, electrical resistance returned to the initial case. The ability of a sensor to sense the presence of gas depends on the nature of the interaction between the gas molecules and the surface atoms of the sensing film.

Figures (4.43) to (4.47) of the SiC and AgO-doped SiC/Si substrate show that the resistance of samples increased with exposed NO_2 gas and decreased when exposed to NH_3 gas on the surface. The different behave of samples indicate that SiC/Si substrate and 7% AgO-doped SiC/Si substrate have a higher selectivity for NO_2 oxidizing gas and NH_3 reducing gas, especially at room temperature.

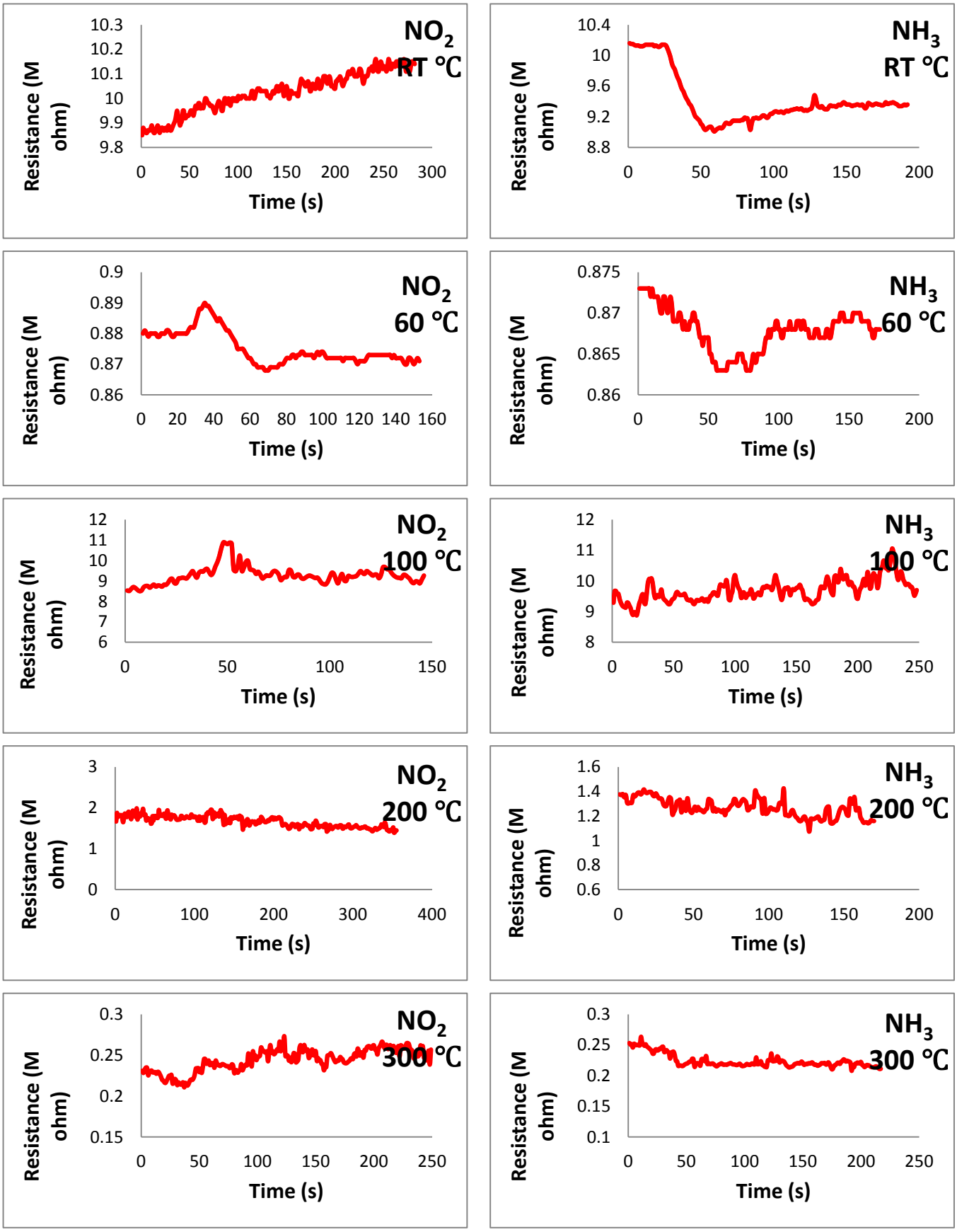

Figure (4.43): The variation resistance with time for different operation temperatures of NO_2 and NH_3 gases for the SiC/p-Si gas sensor.

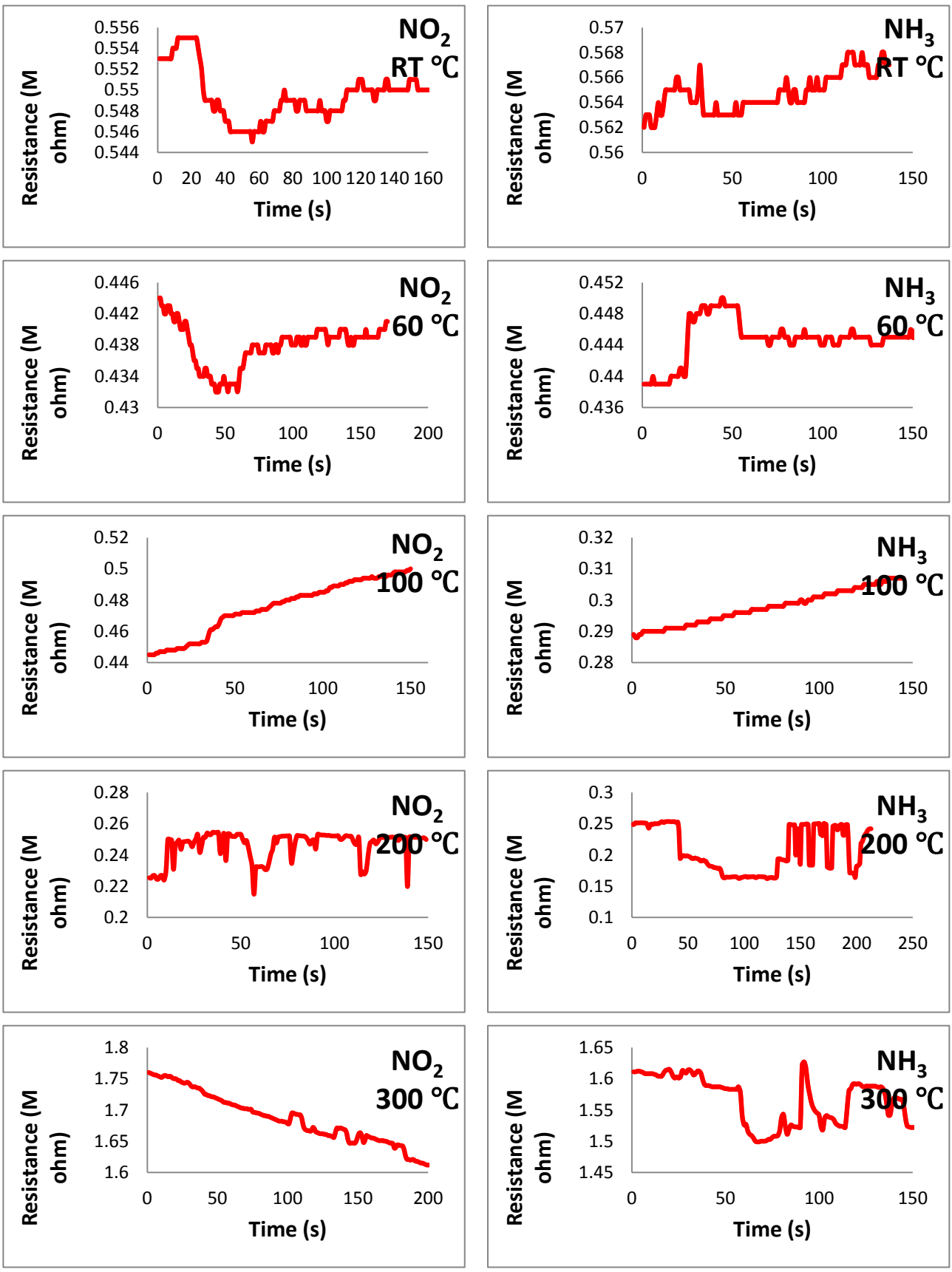

Figure (4.44): The variation resistance with time for different operation temperatures of NO_2 and NH_3 gases for the SiC:AgO/p-Si gas sensor (1% AgO).

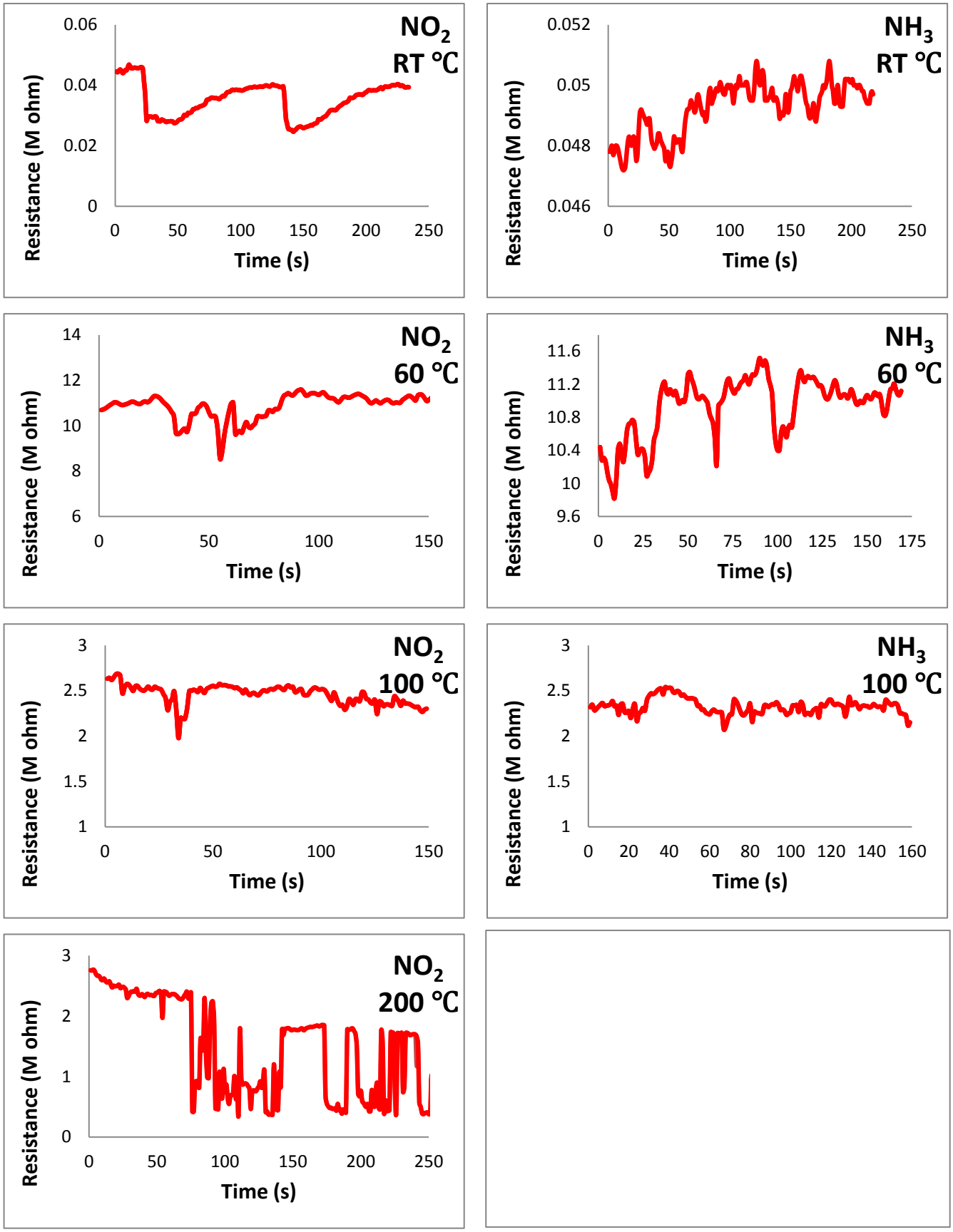

Figure (4.45): The variation resistance with time for different operation temperatures of NO_2 and NH_3 gases for the SiC:AgO/p-Si gas sensor (3% AgO).

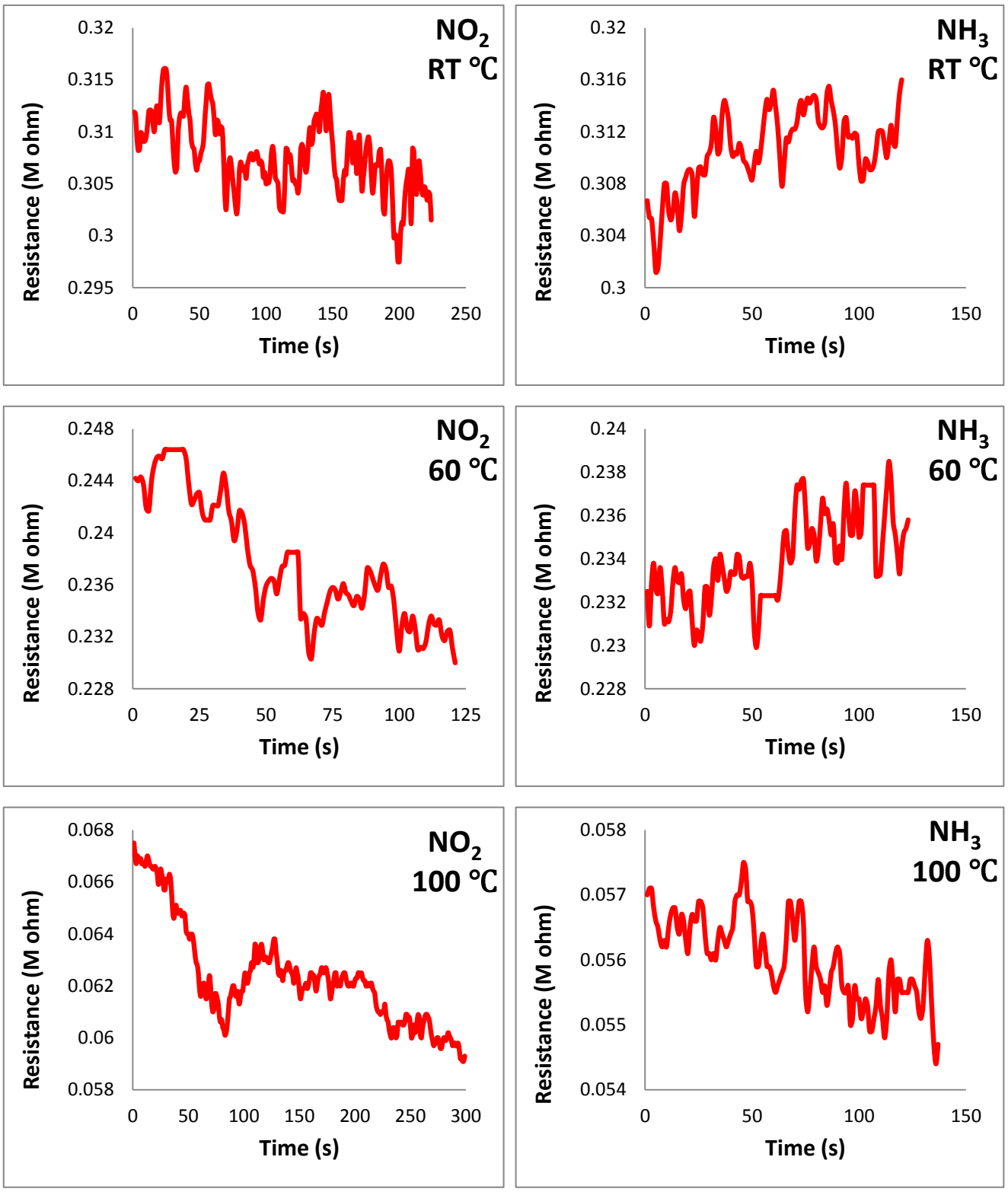

Figure (4.46): The variation resistance with time for different operation temperatures of NO_2 and NH_3 gases for the SiC:AgO/p-Si gas sensor (5% AgO).

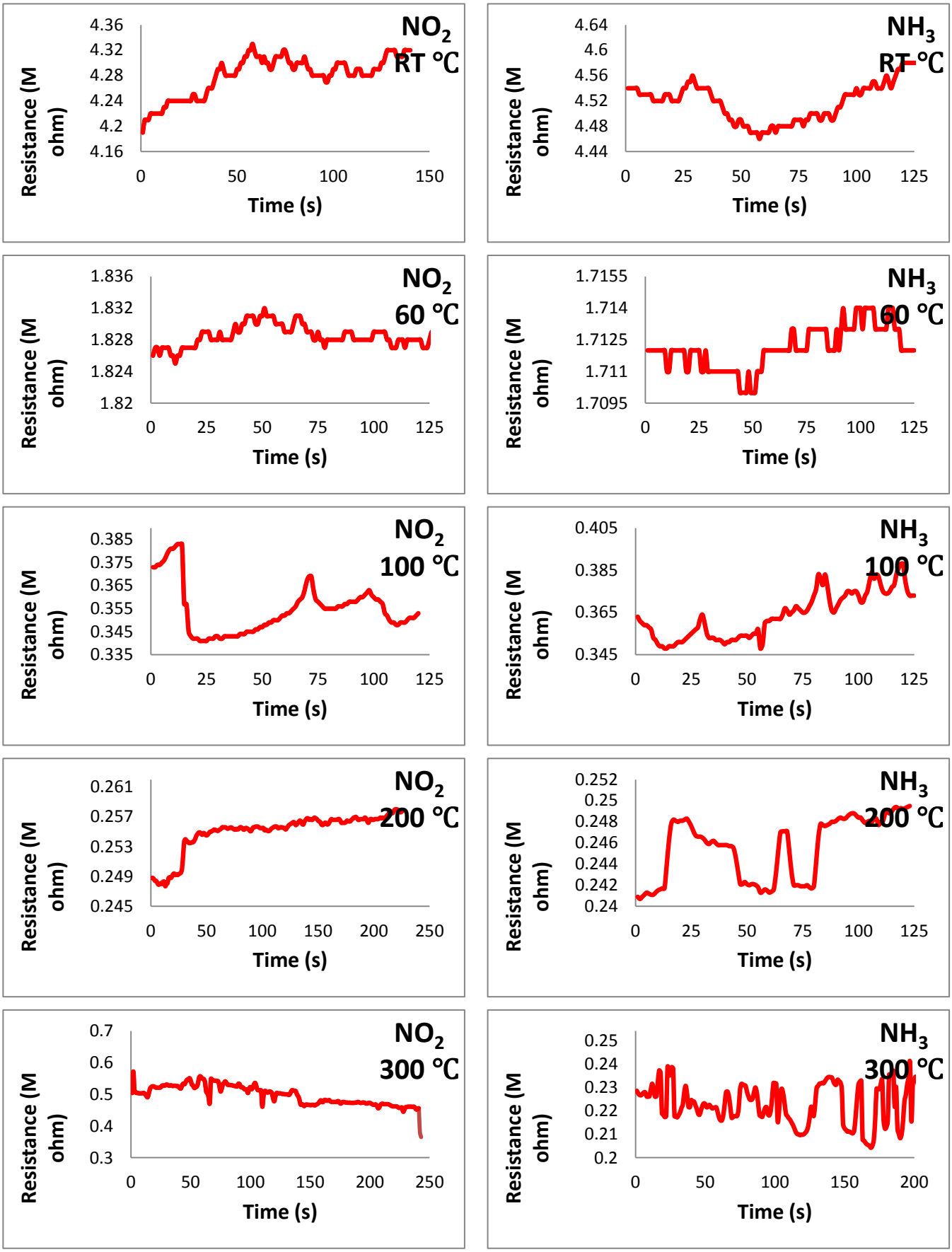

Figure (4.47): The variation resistance with time for different operation temperatures of NO_2 and NH_3 gases for the SiC:AgO/p-Si gas sensor (7% AgO).

Figures (4.48) to (4.52) of the SiC and AgO-doped SiC/glass substrate show that the resistance of samples decreased with exposed NO_2 gas and NH_3 gas. The behave of samples indicates that SiC and AgO-doped SiC/glass substrates have no selectivity for NO_2 oxidizing gas and NH_3 reducing gas.

From the previous results, it can be noted that the samples deposited on a silicon substrate have selectivity to the reducing and oxidization gases with higher distortion single, while the SiC deposited on a glass substrate have a smooth single, but, these samples need a higher temperature for working with no selectivity.

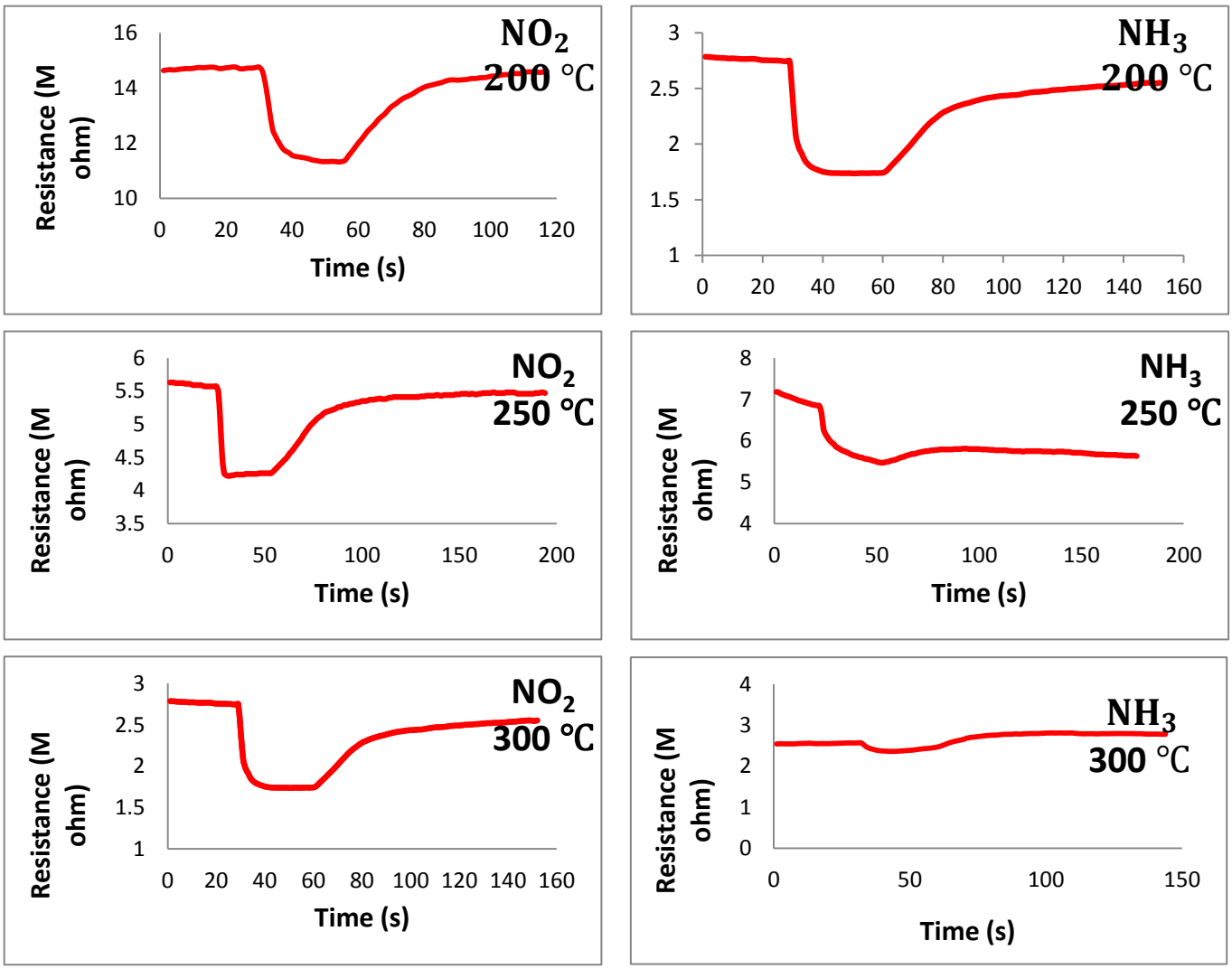

Figure (4.48): The variation resistance with time for different operation temperatures of NO_2 and NH_3 gases for the SiC/glass gas sensor.

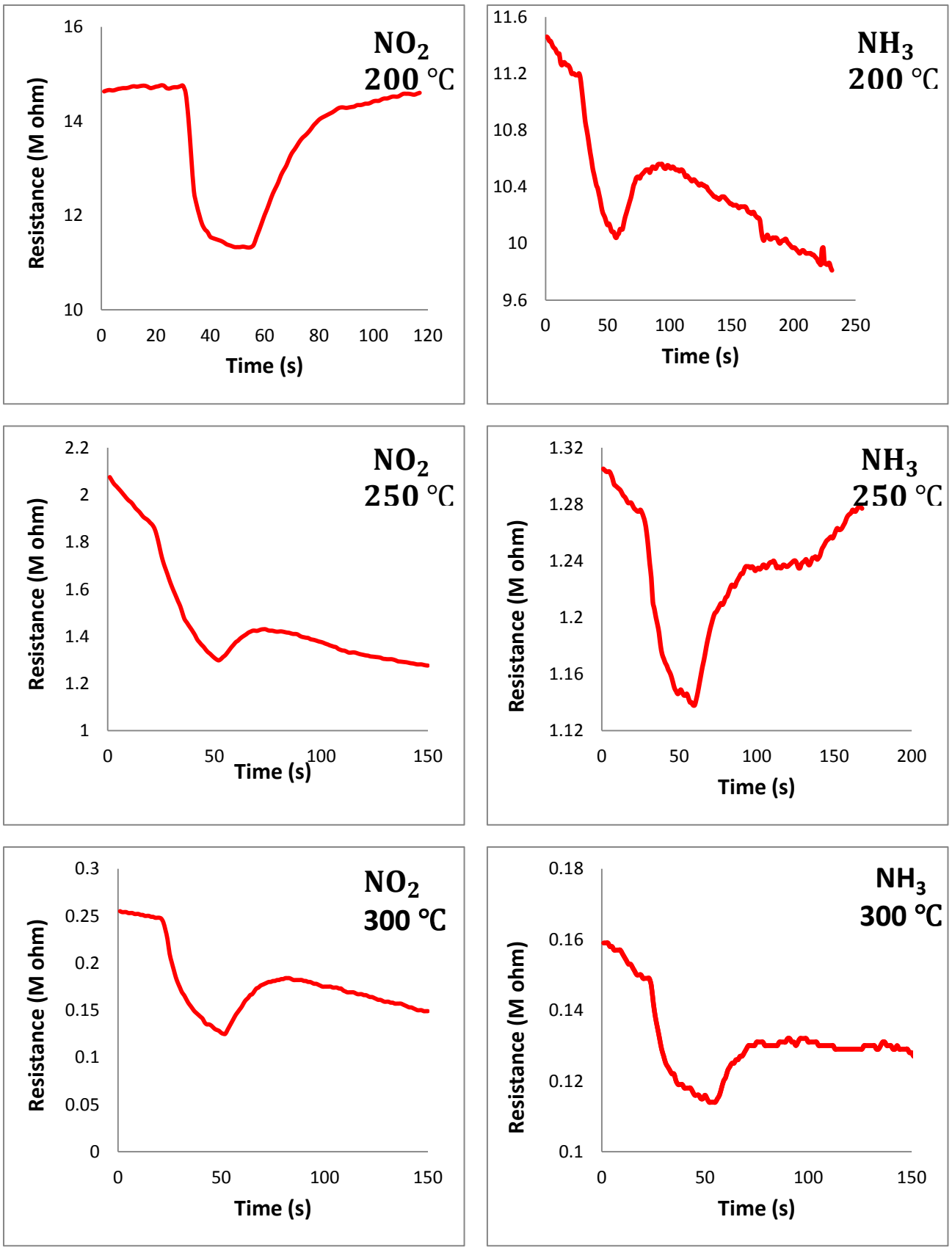

Figure (4.49): The variation resistance with time for different operation temperatures of NO_2 and NH_3 gases for the SiC:AgO/glass gas sensor (1% AgO).

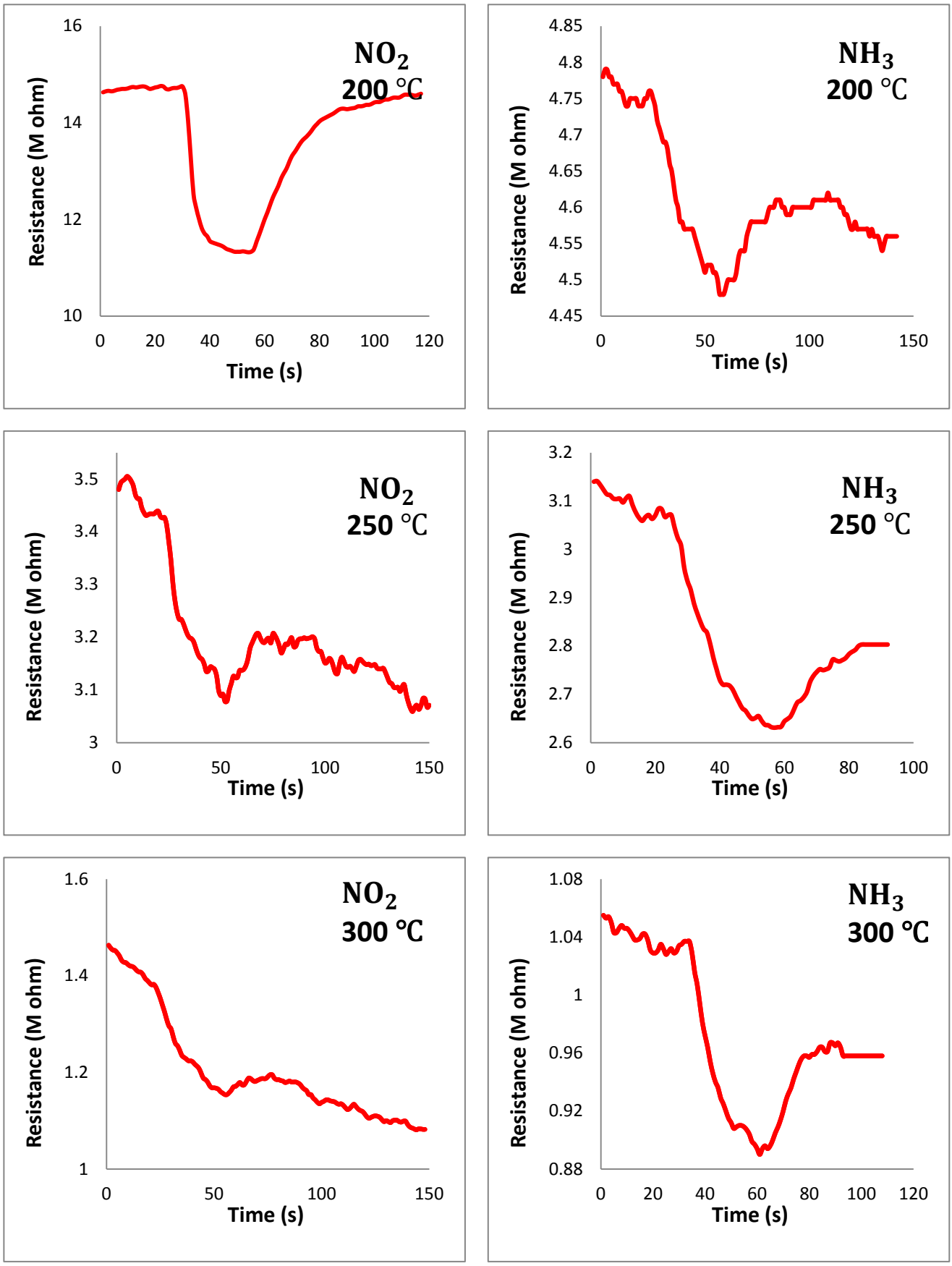

Figure (4.50): The variation resistance with time for different operation temperatures of NO_2 and NH_3 gases for the SiC:AgO/glass gas sensor (3% AgO).

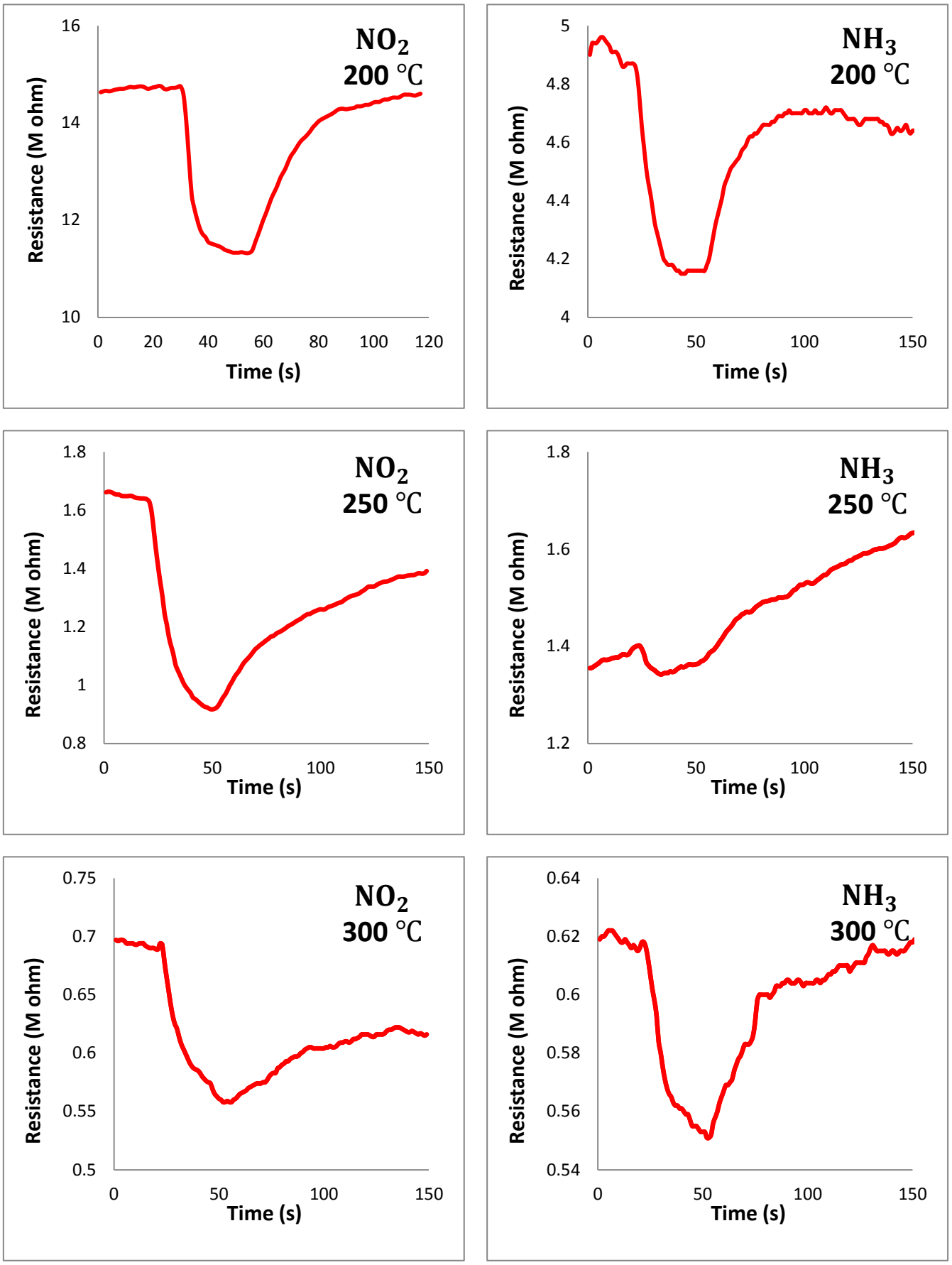

Figure (4.51): The variation resistance with time for different operation temperatures of NO_2 and NH_3 gases for the SiC:AgO/glass gas sensor (5% AgO).

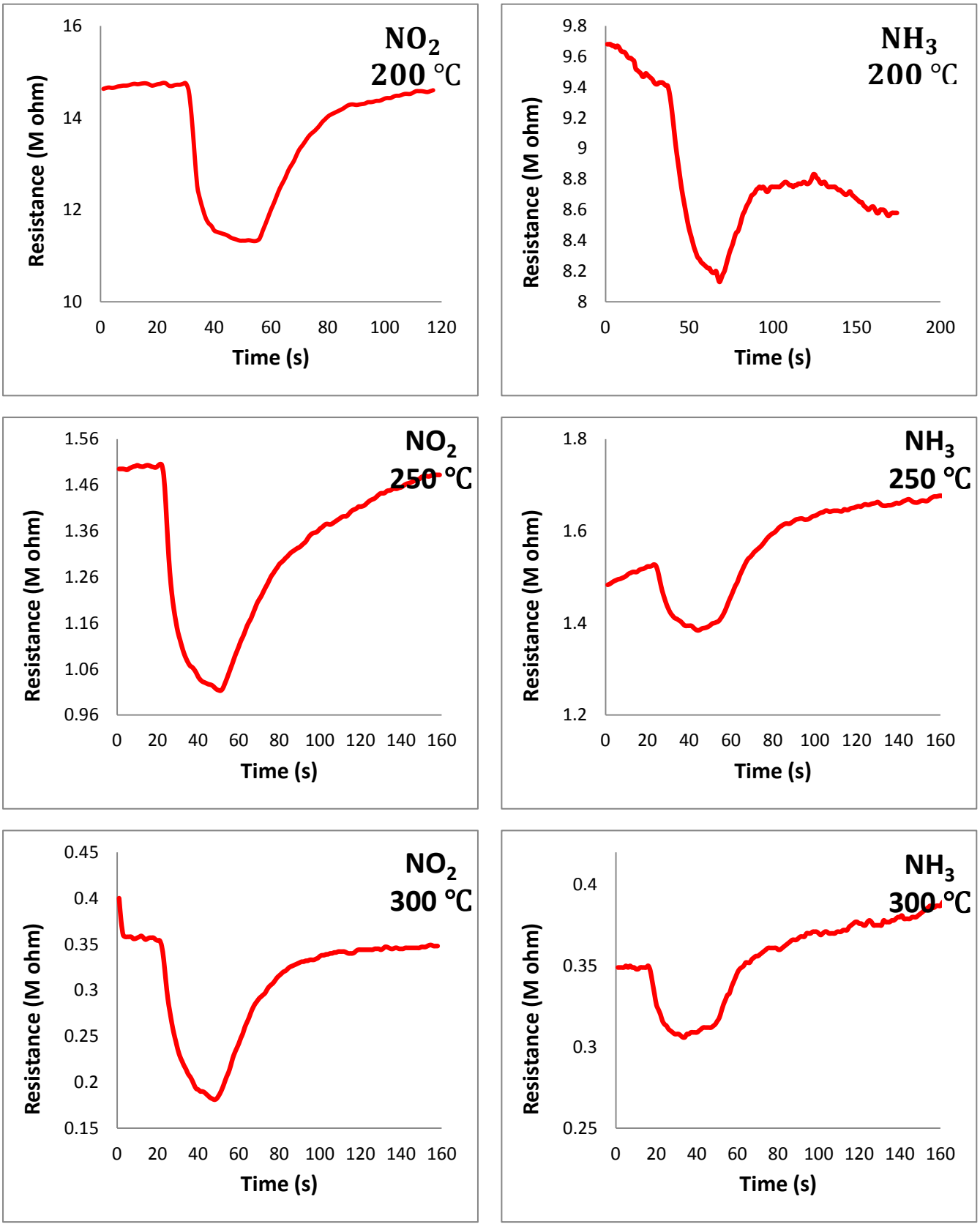

Figure (4.52): The variation resistance with time for different operation temperatures of NO_2 and NH_3 gases for the SiC:AgO/glass gas sensor (7% AgO).

4.7 Conclusions

The most significant conclusions gained during this research will be provided in this section, which will cover the most important measurements and observations, which include the following:

1. The pulsed laser deposition technique has proven to effectively produce thin films at high pressure ($\geq 10^{-4}$ mbar).
2. The X-ray diffraction of SiC:AgO films with different AgO ratios revealed that the SiC films are amorphous, while the AgO-doped SiC films are polycrystalline. The increase in the average crystal size is irregular due to the addition of AgO atoms, where the highest value was for the (1% AgO) sample while the lowest value was for the (7% AgO) sample.
3. The scanning electron microscopy (FESEM) results showed that the shape of the particles was irregular and with different sizes and gradually increased with the increase in the ratios of doping.
4. The EDX exam showed that the films contained (Si, C, and O) elements for pure SiC and (Si, C, O, and Ag) for AgO-doped SiC films.
5. The highest values of the surface roughness (Ra), root mean squared (RMS) and particle size of the film measured by atomic force microscopy (AFM) were (3% AgO) and the lowest value was for the film (7% AgO).
6. Due to the constant number of pulses, the film thickness is nearly equal to (200 nm $\pm$ 5) nm for all prepared films.
7. The increase of the optical absorbance values with an increase in the ratios of AgO.
8. The increasing of AgO ratios, leads to optical energy gap values decrease from (2.61 eV) to (2 eV).

9. All films under study are n-type, that is, the electrical behavior of the SiC film is dominant on all AgO-doped SiC films.
10. Increasing the AgO ratios and applied voltage led to an increase in forward and reverse photocurrent.
11. The efficiency of the SiC/p-Si and SiC:AgO/p-Si films heterojunctions increase gradually with an increase in the ratios of AgO. These results could be improved if we use SiC as a buffer layer, antireflection coating, or Copper Indium Gallium Di-Selenide CIGS.
12. The results demonstrated that samples deposited on silicon substrates operated at room temperature, while those generated on glass substrates operated at high temperatures (200°C).
13. The maximum sensitivity of SiC:AgO/Si films was for (1% AgO and 3% AgO) gas sensors at (200℃ and 25℃) of (NH_3 and NO_2) gases.
14. The fastest response time ms was for the (NH_3 and NO_2) gases at (100℃) of the (3% AgO) gas sensor while the fastest recovery time was for the (NH_3 and NO_2) gases at (25℃ and 100℃) for the (3% AgO and 5% AgO) gas sensor.
15. The maximum sensitivity of SiC:AgO/glass films was for (1% AgO and 7% AgO) gas sensors of (NH_3 and NO_2) gases at (300℃).
16. The fastest response time was of the (SiC) gas sensor at (300℃ and 250℃) for (NH_3 and NO_2) gases while the fastest recovery time was of (1% AgO and 3% AgO) gas sensors at (250℃ and 300℃) for (NH_3 and NO_2) gases.

4.8 Future works and Suggestions

It is possible that the following topics could be suggested in the future.

1. The RF magnetron sputtering technique is used for deposition of the SiC:AgO films for optoelectronics applications.
2. Studying the effect of Noble Metals Oxides on the efficiency of SiC films photodetector using the PLD method.
3. Study and prepare SiC:(Au, Ag, Pt) Nanostructures as the antibacterial application by pulse laser ablation method.

References

[1] Fraga, M. A., Pessoa, R. S., Massi, M., and Maciel, H. S. (2012). Applications of SiC-based thin films in electronic and MEMS devices. *Physics and technology of silicon carbide devices*, **1**: p. 313-336.

[2] Chava, V. S. N. R., (2018). *Study of 4H-SiC and Al_x Ga_{1-x} N Based Heterojunction Devices for Ultraviolet Detection Applications*. PhD Thesis. University of South Carolina.

[3] Maboudian, R., Carraro, C., Senesky, D. G., and Roper, C. S., (2013). Advances in silicon carbide science and technology at the micro- and nanoscales. *Journal of Vacuum Science and Technology A: Vacuum, Surfaces, and Films*, **31**(5): p. 050805.

[4] Eckertova, L. (2012). *Physics of thin films*. Springer Science and Business Media, New York.

[5] Chopra, K. L., and Kaur, I. (1983). Thin film technology: An introduction. *Thin Film Device Applications*. Springer, Boston, MA. p. 1-54.

[6] Nandasiri, M. I., and Thevuthasan, S. (2015). Thin Film Structures in Energy Applications. Springer International Publishing, p. 167-214.

[7] Baskaran, A., and Smereka, P. (2012). Mechanisms of stranski-krastanov growth. *Journal of Applied Physics*, **111**(4): p. 044321.

[8] Saddow, S. E., and Agarwal, A. K. (2004). *Advances in silicon carbide processing and applications*. Artech House Publishers.

[9] Maboudian, R., Carraro, C., Senesky, D. G., and Roper, C. S. (2013). Advances in silicon carbide science and technology at the micro-and nanoscales. *Journal of Vacuum Science and Technology A: Vacuum, Surfaces, and Films*, **31**(5): p. 050805.

[10] Yoshida, S., Ito, T., Hiraki, A., Saito, H., Fujita, S., Ishitani, Y., and Mizutani, T. (2007). Fundamental properties of wide bandgap

semiconductors. In *Wide Bandgap Semiconductors*. Springer, Berlin, Heidelberg, p. 25-96.

[11] Saddow, S. E. (2012). *Silicon carbide biotechnology: a biocompatible semiconductor for advanced biomedical devices and applications*. Elsevier's Science and Technology Rights Department in Oxford, UK.

[12] Kimoto, T., and Cooper, J. A. (2014). *Fundamentals of silicon carbide technology: growth, characterization, devices and applications*. John Wiley and Sons.

[13] Fissel, A. (2003). Artificially layered heteropolytypic structures based on SiC polytypes: molecular beam epitaxy, characterization and properties. *Physics Reports,* **379**(3-4): p. 149-255.

[14] Karch, K., Bechstedt, F., Pavone, P., and Strauch, D. (1996). Pressure-dependent properties of SiC polytypes. *Physical Review B,* **53**(20): p. 13400-13413.

[15] Wang, R., Ma, R., and Zupan, M. (2006). Modeling of Chemical Vapor Deposition of Large-Area Silicon Carbide Thin Film. *Crystal Growth and Design,* **6**(11): p. 2592-2597.

[16] Willander, M., Friesel, M., Wahab, Q.-u., and Straumal, B. (2006). Silicon carbide and diamond for high temperature device applications. *Journal of Materials Science: Materials in Electronics,* **17**(1): p. 1-25.

[17] Irfan, M., Ajmal, M., Mazhar, M. E., Usmani, M. N., Ahmad, S., Abbas, W., and Hussain, M. (2019). Growth and characterization of 4H-SiC by thermal evaporation method. *Dig. J. Nanomater. Biostruct,* **14**: p. 243-247.

[18] Levinshtein, M. E., Rumyantsev, S. L., and Shur, M. S. (Eds.). (2001). *Properties of Advanced Semiconductor Materials: GaN, AIN, InN, BN, SiC, SiGe*. John Wiley and Sons, New York.

[19] Wijesundara, M. B., and Azevedo, R. G. (2011). SiC materials and processing technology. In *Silicon carbide microsystems for harsh environments*. Springer, New York, NY. p. 33-95

[20] Mehregany, M., Tong, L., Matus, L. G., and Larkin, D. J. (1997). Internal stress and elastic modulus measurements on micromachined 3C-SiC thin films. *IEEE Transactions on Electron Devices*, **44**(1): p. 74-79.

[21] Morkoc, B. H., Strite, S., Gao, G. B., Lin, M. E., Sverdlov, B., and Burns, M. (1994). Large-band-gap SiC, III-V nitride, and II-VI ZnSe-based semiconductor device technologies. *Journal of Applied physics*, **76**(3): p. 1363-1398.

[22] Pensl, G., Ciobanu, F., Frank, T., Krieger, M., Reshanov, S., Schmid, F., and Weidner, M. (2005). SiC material properties. *International journal of high speed electronics and systems*, **15**(04): p. 705-745.

[23] Willander, M., Friesel, M., Wahab, Q. U., and Straumal, B. (2006). Silicon carbide and diamond for high temperature device applications. *Journal of Materials Science: Materials in Electronics*, **17**(1): p.1-25.

[24] Choyke, W. J., Matsunami, H., and Pensl, G. (Eds.). (2013). *Silicon carbide: recent major advances*. Springer Science and Business Media, New York.

[25] Presser, V., and Nickel, K. G. (2008). Silica on silicon carbide. *Critical reviews in solid state and materials sciences*, **33**(1): p. 1-99.

[26] Cicero, G., Catellani, A., and Galli, G. (2004). Atomic control of water interaction with biocompatible surfaces: the case of SiC (001). *Physical review letters*, **93**(1): p. 016102.

[27] Ruff, M., Mitlehner, H., and Helbig, R. (1994). SiC devices: physics and numerical simulation. *IEEE Transactions on electron devices*, **41**(6): p. 1040-1054.

[28] Wijesundara, M., and Azevedo, R. (2011). *Silicon carbide microsystems for harsh environments*. Springer-Verlag, New York.

[29] Mokhov, E. N. (2018). Doping of SiC crystals during sublimation growth and diffusion. In *Crystal Growth*. IntechOpen.

[30] Jansson, M. (2015). Optical properties of free-standing cubic silicon carbide. M.Sc. Thesis, Linköping University, Faculty of Science and Engineering.

[31] Poole Jr, C. P. (2004). *Encyclopedic dictionary of condensed matter physics*. Academic Press and Elsevier.

[32] Trigg, G. L. (1993). Encyclopedia of Applied Physics. *International Journal of Materials Research*, **84**(9): p. 604-604.

[33] Russell, A., and Lee, K. L. (2005). *Structure-property relations in nonferrous metals*. John Wiley and Sons, Inc., Hoboken, New Jersey.

[34] Haynes, W. M. (Ed.). (2014). *CRC handbook of chemistry and physics*. CRC press.

[35] Monaco, G., Garoli, D., Natali, M., Pelizzo, M. G., and Nicolosi, P. (2010). Crystalline 3C-SiC Deposited by PLD Using Different Manufactured Targets. In *AIP Conference Proceedings*, **1292**(1): p. 35-38.

[36] Lim, G., DeSilva, U. P., Quick, N. R., and Kar, A. (2010). Laser optical gas sensor by photoexcitation effect on refractive index. *Applied optics*, **49**(9): p. 1563-1573.

[37] Monaco, G., Garoli, D., Natali, M., Pelizzo, M. G., and Nicolosi, P. (2011). Synthesis of heteroepytaxial 3C-SiC by means of PLD. *Applied Physics A*, **105**(1): p. 225-231.

[38] Zheng, H. W., Wang, Z. Q., Liu, X. Y., Diao, C. L., Zhang, H. R., and Gu, Y. Z. (2011). Local structure and magnetic properties of Mn-doped 3C-SiC nanoparticles. *Applied physics letters*, **99**(22): p. 222512.

[39] Kim, K. S., and Chung, G. S. (2011). Characterization of porous cubic silicon carbide deposited with Pd and Pt nanoparticles as a hydrogen sensor. *Sensors and Actuators B: Chemical*, **157**(2): p. 482-487.

[40] Bhimasingu, V., Vasa, N. J., and Palani, I. A. (2012). Influence of Substrate Temperature, Pressure and Grit Size on Synthesis of SiC Thin Film by Pulsed Laser Deposition. Technique. In *International Conference on Intelligent Robotics, Automation, and Manufacturing*, p. 379-388.

[41] An, Y., Duan, L., Li, X., Wu, Z., and Liu, J. (2012). Investigation of microstructures and optical properties in Mn-doped SiC films. *Applied surface science*, **258**(18): p. 7070-7074.

[42] Mao, H. Y., Wuu, D. S., Wu, B. R., Lo, S. Y., Hsieh, H. Y., and Horng, R. H. (2012). Hot-wire chemical vapor deposition and characterization of p-type nanocrystalline SiC films and their use in Si heterojunction solar cells. *Thin Solid Films*, **520**(6): p. 2110-2114.

[43] Mishra, P. K., and Sahoo, B. (2013). Silicon carbide thin film formation by pulse laser ablation and its characterization study. *International Atomic Energy Agency* (IAEA), **44**(37): p. 1-9.

[44] Ma, J., Ni, J., Zhang, J., Huang, Z., Hou, G., Chen, X., and Zhao, Y. (2013). Improvement of solar cells performance by boron doped amorphous silicon carbide/nanocrystalline silicon hybrid window layers. *Solar energy materials and solar cells*, **114**: p. 9-14.

[45] Keffous, A., Cheriet, A., Hadjersi, T., Boukennous, Y., Gabouze, N., Boukezzata, A., and Ouadah, Y. (2013). 40 Å Platinum–porous SiC gas sensor: Investigation sensing properties of H_2 gas. *Physica B: Condensed Matter*, **408**: p. 193-197.

[46] Zakhvalinskii, V., Piliuk, E., Goncharov, I., Simashkevich, A. V., Sherban, D. A., Bruc, L. I., and Rusu, M. (2013). p-Si/n-SiC nanolayer photovoltaic cell. In *Proceedings of the 28th European Photovoltaic Solar Energy Conference*. p. 1317-1320

[47] Socol, G., Galca, A. C., Craciun, D., Hanna, M., Taylor, C. R., Lambers, E., and Craciun, V. (2014). Pulsed laser deposition of nanocrystalline SiC films. *Applied surface science*, **306**: p. 66-69.

[48] Wang, S., An, Y., Li, X., Wu, Z., and Liu, J. (2014). Effect of Mn doping on the structural, magnetic and transport properties of SiC films. *Journal of alloys and compounds*, **584**: p. 339-343.

[49] Latha, H. K. E., Udayakumar, A., and Prasad, V. S. (2014). Effect of nitrogen doping on the electrical properties of 3C-SiC thin films for high-temperature sensors applications. *Acta Metallurgica Sinica (English Letters)*, **27**(1): p. 168-174.

[50] Ryndya, S. M., Kargin, N. I., Gusev, A. S., and Pavlova, E. P. (2015). PLD grown 3C-SiC thin films on Si: morphology and structure. In *Materials Science Forum*, **821**: p. 213-216.

[51] Badea, M., Braic, M., Kiss, A., Moga, M., Pozna, E., Pana, I., and Vladescu, A. (2016). Influence of Ag content on the antibacterial properties of SiC doped hydroxyapatite coatings. *Ceramics International*, **42**(1): p. 1801-1811.

[52] Dey, P. P., and Khare, A. (2016). Effect of substrate temperature on structural and linear and nonlinear optical properties of nanostructured PLD a-SiC thin films. *Materials Research Bulletin*, **84**: p. 105-117.

[53] Šály, V., Perný, M., Packa, J., Janíček, F., Váry, M., Mikolášek, M., and Huran, J. (2017). AC and DC response of heterojunction a-SiC/c-Si for PV application. *International Scientific Conference on Electric Power Engineering (EPE)*, p. 1-4.

[54] Cheng, Y., Huang, X., Du, Z., and Xiao, J. (2017). Effect of sputtering power on the structure and optical band gap of SiC thin films. *Optical Materials*, **73**: p. 723-728.

[55] Perný, M., Šály, V., Janíček, F., Mikolášek, M., Vary, M., and Huran, J. (2018). Electric measurements of PV heterojunction structures a-SiC/c-Si. *Journal of Electrical Engineering*, **69**(1): p. 52-57.

[56] Kumar, A., Kumar, A., and Chandra, R. (2018). Fabrication of porous silicon filled Pd/SiC nanocauliflower thin films for high performance H_2 gas sensor. *Sensors and Actuators B: Chemical*, **264**: p. 10-19.

[57] Paneerselvam, E., Narayanan, L., Kumar, V., Vasa, N. J., Higashihata, M., Nakamura, D., and Rao, R. (2019). Laser Assisted Doping of Silicon Carbide Thin Films Grown by Pulsed Laser Deposition. *Journal of Electronic Materials*, **48**(6): p. 3468-3478

[58] Hsu, C. H., Zhang, X. Y., Zhao, M. J., Lin, H. J., Zhu, W. Z., and Lien, S. Y. (2019). Silicon heterojunction solar cells with p-type silicon carbon window layer. *Crystals*, **9**(8): p. 402.

[59] Tavsanoglu, T., Zayim, E. O., Agirseven, O., Yildirim, S., and Yucel, O. (2019). Optical, electrical and microstructural properties of SiC thin films deposited by reactive dc magnetron sputtering. *Thin Solid Films*, **674**: p. 1-6.

[60] Tehrani, F. S., Fakhredin, M., and Tafreshi, M. J. (2019). The optical properties of silicon carbide thin films prepared by HWCVD from pure silane and methane under various total gas partial pressure. *Materials Research Express*, **6**(8): p. 086469.

[61] Mourya, S., Kumar, A., Jaiswal, J., Malik, G., Kumar, B., and Chandra, R. (2019). Development of Pd-Pt functionalized high performance H_2 gas sensor based on silicon carbide coated porous silicon

for extreme environment applications. *Sensors and Actuators B: Chemical*, **283**: p. 373-383.

[62] Kumar, M., Kumar, A., Gautam, Y. K., Chandra, R., Goyat, M. S., Tewari, B. S., and Tewari, R. K. (2020). Influence of SiC thin films thickness on the electrical properties of Pd/SiC thin films for hydrogen gas sensor. *Vacuum*, **182**: p. 109750.

[63] Paneerselvam, E., Vasa, N. J., Nakamura, D., Palani, I. A., Higashihata, M., Rao, M. R., and Thomas, T. (2021). Pulsed laser deposition of SiC thin films and influence of laser-assisted annealing. *Materials Today: Proceedings*, **35**: p. 312-317.

[64] Mohsin, M. H., Numan, N. H., Salim, E. T., and Fakhri, M. A. (2021). Physical Properties of SiC Nanostructure for Optoelectronics Applications. *Journal of Renewable Materials*, **9**(9): p. 1530-1519.

[65] Chrisey, D. B., and Hubler, G. K. (Eds.). (1994). Pulsed laser deposition of thin films. Wiley-Interscience.

[66] Willmott, P. R., and Huber, J. R. (2000). Pulsed laser vaporization and deposition. *Reviews of Modern Physics*, **72**(1): p. 315.

[67] Ferrante, G., Zarcone, M., and Uryupin, S. A. (2001). Inverse bremsstrahlung in a plasma with electron temperature anisotropy. *Physics of Plasmas*, **8**(11): p. 4745-4752.

[68] Han, X., Wang, G., Jie, J., Zhu, X., and Hou, J. G. (2005). Properties of $Zn_{1-x}Co_xO$ thin films grown on silicon substrates prepared by pulsed laser deposition. *Thin Solid Films*, **491**(1-2): p. 249-252.

[69] Lowndes, D. H., Geohegan, D. B., Puretzky, A. A., Norton, D. P., and Rouleau, C. M. (1996). Synthesis of novel thin-film materials by pulsed laser deposition. *Science*, **273**(5277): p. 898-903.

[70] Grant-Jacob, J. A., Beecher, S. J., Prentice, J. J., Shepherd, D. P., Mackenzie, J. I., and Eason, R. W. (2018). Pulsed laser deposition of

crystalline garnet waveguides at a growth rate of 20 μm per hour. *Surface and Coatings Technology*, **343**: p. 7-10.

[71] Scharf, T., and Krebs, H. U. (2002). Influence of inert gas pressure on deposition rate during pulsed laser deposition. *Applied Physics A*, **75**(5): p. 551-554.

[72] Stafe, M., Marcu, A., and Puscas, N. N. (2013). *Pulsed laser ablation of solids: basics, theory and applications*. Springer Science and Business Media, New York.

[73] Eason, R. (Ed.). (2007). *Pulsed laser deposition of thin films: applications-led growth of functional materials*. John Wiley and Sons.

[74] Tang, Y. H., Sham, T. K., Yang, D., and Xue, L. (2006). Preparation and characterization of pulsed laser deposition (PLD) SiC films. *Applied surface science*, **252**(10): p. 3386-3389.

[75] Mittra, J., Abraham, G. J., Kesaria, M., Bahl, S., Gupta, A., Shivaprasad, S. M., and Dey, G. K. (2012). Role of substrate temperature in the pulsed laser deposition of zirconium oxide thin film. *Materials Science Forum*, **710**: p. 757-761.

[76] Shen, J., Gai, Z., and Kirschner, J. (2004). Growth and magnetism of metallic thin films and multilayers by pulsed-laser deposition. *Surface science reports*, **52**(5-6): p. 163-218.

[77] Harilal, S. S., Bindhu, C. V., Nampoori, V. P. N., and Vallabhan, C. P. G. (1998). Influence of ambient gas on the temperature and density of laser produced carbon plasma. *Applied Physics Letters*, **72**(2): p. 167-169.

[78] Mihailescu, I. N., and Caricato, A. P. (2018). *Pulsed Laser Ablation: Advances and Applications in Nanoparticles and Nanostructuring Thin Films*. Jenny Stanford Publishing.

[79] Donnelly, T. O. N. Y., Lunney, J. G., Amoruso, S., Bruzzese, R., Wang, X., and Ni, X. (2010). Dynamics of the plumes produced by

ultrafast laser ablation of metals. *Journal of Applied Physics*, **108**(4): p. 043309.

[80] Phipps, C. (Ed.). (2007). *Laser ablation and its applications* (Vol. 129). Springer.

[81] Fujioka, H. (2015). Pulsed laser deposition (PLD). *Handbook of Crystal Growth*.: Thin Films and Epitaxy (Second Edition), North-Holland, p. 365-397.

[82] Fang, R., Zhang, D., Li, Z., Li, L., Tan, X., and Yang, F. (2007). Laser-target interaction during high-power pulsed laser deposition of superconducting thin films. *physica status solidi (a)*, **204**(12): p. 4241-4248.

[83] Kools, J. C. S., Baller, T. S., De Zwart, S. T., and Dieleman, J. (1992). Gas flow dynamics in laser ablation deposition. *Journal of Applied Physics*, **71**(9): p. 4547-4556.

[84] Anisimov, S. I., Bäuerle, D., and Luk'Yanchuk, B. S. (1993). Gas dynamics and film profiles in pulsed laser deposition of materials. *Physical Review B*, **48**(16): p. 12076.

[85] Itina, T. E., Hermann, J., Delaporte, P., and Sentis, M. (2002). Laser-generated plasma plume expansion: Combined continuous-microscopic modeling. *Physical Review E*, **66**(6): p. 066406.

[86] Ausanio, G. A., Barone, A. C., Iannotti, V., Lanotte, L., Amoruso, S., Bruzzese, R., and Vitiello, M. (2004). Magnetic and morphological characteristics of nickel nanoparticles films produced by femtosecond laser ablation. *Applied physics letters*, **85**(18): p. 4103-4105.

[87] Eliezer, S., Eliaz, N., Grossman, E., Fisher, D., Gouzman, I., Henis, Z., and Lereah, Y. (2004). Synthesis of nanoparticles with femtosecond laser pulses. *Physical Review B*, **69**(14): p. 144119.

[88] Schou, J. (2009). Physical aspects of the pulsed laser deposition technique: The stoichiometric transfer of material from target to film. *Applied Surface Science*, **255**(10): p. 5191-5198.

[89] Amoruso, S., Toftmann, B., Schou, J., Velotta, R., and Wang, X. (2004). Diagnostics of laser ablated plasma plumes. *Thin solid films*, **453**: p. 562-572.

[90] Sivaram, S. (2013). *Chemical vapor deposition: thermal and plasma deposition of electronic materials*. Springer Science and Business Media, New York, NY.

[91] Constantinescu, C., Morintale, E., Scarisoreanu, N., Moldovan, A., and Dinescu, M. (2010). Nanometricsized Fe/Pt thin films with perpendicular anisotropy developed by layer-by-layer pulsed lased deposition. *Physics AUC*, **20**: p. 73.

[92] Schou, J. (2009). Physical aspects of the pulsed laser deposition technique: The stoichiometric transfer of material from target to film. *Applied Surface Science*, **255**(10): p. 5191-5198.

[93] Rajendiran, S. (2017). *Plasma enhanced pulsed laser deposition*. PhD thesis, University of York.

[94] Yacobi, B. G. (2003). *Semiconductor materials: an introduction to basic principles*. Springer Science and Business Media.

[95] Sapoval, B., and Hermann, C. (2003). *Physics of semiconductors*. Springer Science and Business Media.

[96] Kazmerski, L. L. (1980). Electrical properties of polycrystalline semiconductor thin films. *Polycrystalline and amorphous thin films and devices*, p. 59-133.

[97] Adachi, S. (2012). *Optical properties of crystalline and amorphous semiconductors: Materials and fundamental principles*. Springer Science and Business Media.

[98] Achimovičová, M., Rečnik, A., Fabián, M., and Baláž, P. (2011). Characterization of tin selenides synthesized by high-energy milling. *Acta Montanistica Slovaca*, **16**(2): 123.

[99] Streetman, B. G., and Banerjee, S. (2006). *Solid state electronic devices* (Vol. 10). Upper Saddle River, NJ: Pearson/Prentice Hall.

[100] Callister, W. D. (2006). An introduction: material science and engineering. *John Wiley and Sons Inc*.

[101] Grosso, Giuseppe, and Giuseppe Pastori Parravicini. (2013). *Solid state physics*. Academic press.

[102] Hass, G., Francombe, M. H., and Hoffman, R. W. (2013). *Physics of thin films: Advances in research and development*. Elsevier.

[103] Kittel, C. (2005). Introduction to Solid State Physics. 8th Edition, John Wiley and Sons, New York.

[104] Stanjek, H., and Häusler, W. J. H. I. (2004). Basics of X-ray Diffraction. *Hyperfine interactions*, **154**(1): p. 107-119.

[105] Pope, C. G. (1997). X-ray diffraction and the Bragg equation. *Journal of chemical education*, **74**(1): p. 129.

[106] Sadowski, M. L., Potemski, M., and Grynberg, M. (2000). *Optical properties of semiconductor nanostructures* (Vol. 81). Springer Science and Business Media.

[107] Pawlowski, L. (2008). *The science and engineering of thermal spray coatings*. John Wiley and Sons.

[108] Cohen, M. L., and Chelikowsky, J. R. (2012). *Electronic structure and optical properties of semiconductors* (Vol. 75). Springer Science and Business Media.

[109] Yon, V., Rochat, N., Charles, M., Nolot, E., and Gergaud, P. (2020). X-Ray Diffraction Microstrain Analysis for Extraction of Threading Dislocation Density of GaN Films Grown on Si, Sapphire, and SiC Substrates. *physica status solidi (b)*, **257**(4): p. 1900579.

[110] Blakemore, J. S. (1986). Solid state physics. Cambridge University Press.

[111**]** Havrdova, M., Polakova, K., Skopalik, J., Vujtek, M., Mokdad, A., Homolkova, M., and Zboril, R. (2014). Field emission scanning electron microscopy (FE-SEM) as an approach for nanoparticle detection inside cells. *Micron*, **67**: p. 149-154.

[112**]** Giridharagopal, R., Shao, G., Groves, C., and Ginger, D. S. (2010). New scanning probe microscopy techniques for analyzing organic photovoltaic materials and devices. *Photovoltaics world.*, **2**(4): p. 23-27.

[113] Bhagyaraj, S. M., Oluwafemi, O. S., Kalarikkal, N., and Thomas, S. (Eds.). (2018). Characterization of Nanomaterials: Advances and Key Technologies. Cambridge, MA: Woodhead Publishing.

[114] Eaton, P., and West, P. (2010). *Atomic force microscopy*. Oxford university press.

[115] Alford, T. L., Feldman, L. C., and Mayer, J. W. (2007). *Fundamentals of nanoscale film analysis*. Springer Science and Business Media.

[116] Wooten, F. (1973). Optical properties of solids. *American Journal of Physics*, **41**(7): p. 939-940.

[117] Majewski, J. A., Birner, S., Trellakis, A., Sabathil, M., & Vogl, P. (2004). Advances in the theory of electronic structure of semiconductors. *physica status solidi (c)*, **1**(8): p. 2003-2027.

[118] Omar, M. A. (1975). *Elementary solid state physics: principles and applications*. Pearson Education India.

[119] Pankove, J. I. (1971). Solid state physical electronics series. *Optical Processes in Semiconductors. Prentice-Hall, Inc.*

[120] Cun, W., Xinming, W., Jincai, Z., Bixian, M., Guoying, S., Ping'an, P., and Jiamo, F. (2002). Synthesis, characterization and photocatalytic

property of nano-sized Zn 2 SnO 4. *Journal of Materials Science*, **37**(14): p. 2989-2996.

[121] Callister Jr, W. D., and Rethwisch, D. G. (2020). *Fundamentals of materials science and engineering: an integrated approach*. John Wiley and Sons.

[122] Balkanski, M., and Wallis, R. F. (2000). *Semiconductor physics and applications* (Vol. 8). Oxford university press.

[123] Whitaker, J. C. (2018). *Microelectronics*. CRC Press, New York.

[124] Shannon, R. D., and Pask, J. A. (1965). Kinetics of the anatase-rutile transformation. *Journal of the American Ceramic Society*, **48**(8): p. 391-398.

[125] Al-Bataineh, Q. M., Alsaad, A. M., Ahmad, A. A., and Telfah, A. (2020). A novel optical model of the experimental transmission spectra of nanocomposite PVC-PS hybrid thin films doped with silica nanoparticles. *Heliyon*, **6**(6): p. e04177.

[126] Tauc, J. (Ed.). (2012). *Amorphous and liquid semiconductors*. Springer Science and Business Media.

[127] Eichler, H. J., and Hermerschmidt, A. (2006). Light-induced dynamic gratings and photorefraction. In *Photorefractive Materials and Their Applications*. Springer, New York, NY.

[128] Hofmann, P. (2015). *Solid state physics: an introduction*. John Wiley and Sons.

[129] Vasko, F. T., and Kuznetsov, A. V. (1998). *Electronic states and optical transitions in semiconductor heterostructures*. Springer Science and Business Media.

[130] Hilden, L. R., and Morris, K. R. (2004). Physics of amorphous solids. *Journal of pharmaceutical sciences*, **93**(1): p. 3-12.

[131] Shakti, N., and Gupta, P. S. (2010). Structural and optical properties of sol-gel prepared ZnO thin film. *Applied Physics Research*, **2**(1): p. 19.

[132] Fukuda, M. (1998). *Optical semiconductor devices* (Vol. 46). John Wiley and Sons.

[133] Tavsanoglu, T., Zayim, E. O., Agirseven, O., Yildirim, S., and Yucel, O. (2019). Optical, electrical and microstructural properties of SiC thin films deposited by reactive dc magnetron sputtering. *Thin Solid Films,* **674**: p. 1-6.

[134] Kazmerski, L. (Ed.). (2012). *Polycrystalline and amorphous thin films and devices*. Academic Press, Elsevier.

[135] Peter, Y. U., and Cardona, M. (2010). *Fundamentals of semiconductors: physics and materials properties*. Springer Science and Business Media.

[136] Burns, G. (1985). Solid State Physics. Academic Press. *Inc., United States*.

[137] Wooten, F. (2013). *Optical properties of solids*. Academic press.

[138] Chopra, K. L. (1979). *Thin film phenomena*. Krieger Publishing Company.

[139] Balogun, S. W., Sanusi, Y. K., and Aina, A. O. (2018). Structural and optical properties of Titanium dioxide thin film deposited by spin coating technique. *Inter. J. Dev. Res*, **8**(01): p. 18486-18490.

[140] Yakuphanoglu, F., Cukurovali, A., and Yilmaz, I. (2004). Single-oscillator model and determination of optical constants of some optical thin film materials. *Physica B: Condensed Matter*, **353**(3-4): p. 210-216.

[141] Sun, J., and Kosel, J. (2012). Finite-element modelling and analysis of hall effect and extraordinary magnetoresistance effect. *Finite Element Analysis-New Trends and Developments*, p. 201-224.

[142] Popovic, R. S. (2004). *Hall Effect Devices*, Published by CRC Press.

[143] Sze, S. M., and Kwok, K. Ng. (2006). *Physics of Semiconductor Devices*. John wiley and sons.

[144] Kressel, H. (2012). *Semiconductor lasers and herterojunction LEDs*. Elsevier.

[145] Milnes, A. G. (2012). *Heterojunctions and metal semiconductor junctions*. Elsevier.

[146] De Visschere, P., Burgelman, M., and Pauwels, H. (1987). II–VI heterojunction device physics. *Solid-State Electronics*, **30**(11): p. 1215-1220.

[147] Goetzberger, A., Knobloch, J., and Voss, B. (1998). *Crystalline silicon solar cells* (Vol. 1). Chichester: Wiley.

[148] Tanabe, K. (2021). Nanostructured Materials for Solar Cell Applications. *Nanomaterials*, **12**(1): p. 26.

[149] Colinge, J. P., and Colinge, C. A. (2005). *Physics of semiconductor devices*. Springer Science and Business Media.

[150] Martil, I., and Diaz, G. G. (1992). Determination of the dark and illuminated characteristic parameters of a solar cell from IV characteristics. *European journal of physics*, **13**(4): p. 193.

[151] Priambodo, P. S., Sukoco, D., Purnomo, W., Sudibyo, H., and Hartanto, D. (2013). Electric energy management and engineering in solar cell system. *Solar Cells–Res Appl Perspect, InTech*, **12**: p. 327-351.

[152] El Assyry, A., Lamsayah, M., Warad, I., Touzani, R., Bentiss, F., and Zarrouk, A. (2020). Theoretical investigation using DFT of quinoxaline derivatives for electronic and photovoltaic effects. *Heliyon*, **6**(3): p. e03620.

[153] Kalogirou, S. (Ed.). (2017). *McEvoy's handbook of photovoltaics: fundamentals and applications*. Academic Press.

[154] Sberveglieri, G. (Ed.). (2012). *Gas sensors: principles, operation and developments*. Springer Science and Business Media.

[155] Jaaniso, R., and Tan, O. K. (Eds.). (2013). *Semiconductor gas sensors*. Elsevier.

[156] Zeng, J. N., Low, J. K., Ren, Z. M., Liew, T., and Lu, Y. F. (2002). Effect of deposition conditions on optical and electrical properties of ZnO films prepared by pulsed laser deposition. *Applied surface science*, **197**: p. 362-367.

[157] Hulanicki, A., Glab, S., and Ingman, F. O. L. K. E. (1991). Chemical sensors: definitions and classification. *Pure and applied chemistry*, **63**(9): p. 1247-1250.

[158] Abdul-Ameer, Z.N, (2016). Investigation Characteristics of ZnO-CdO Nanocomposites for Gas Sensing Applications, Ph.D. Thesis, Al-Mustansiriyah University.

[159] Wang, C., Yin, L., Zhang, L., Xiang, D., and Gao, R. (2010). Metal oxide gas sensors: sensitivity and influencing factors. *sensors*, **10**(3): p. 2088-2106.

[160] Hildenbrand, J. (2003). *Simulation and characterisation of a micromachined gas sensor and preparation for model order reduction* (Ph.D. Thesis, Institute for Microsystem Technology, Albert Ludwig University Freiburg, Alemania).

[161] Singh, N., Kumar, A., and Kaur, D. (2018). Hydrogen gas sensing properties of platinum decorated silicon carbide (Pt/SiC) Nanoballs. *Sensors and Actuators B: Chemical*, **262**: p. 162-170.

[162] Yamazoe, N., Sakai, G., and Shimanoe, K. (2003). Oxide semiconductor gas sensors. *Catalysis Surveys from Asia*, **7**(1): p. 63-75.

[163] Mishra, R. L., Mishra, S. K., and Prakash, S. G. (2009). Optical and Gas Sensing Characteristics of Tin Oxide Nano-Crystalline Thin Film. *Journal of Ovonic Research*, **5**(4): p. 77-85.

[164] Sriram, S., Balu, A., and Thayumanavan, A. (2011). Design and Development of Automated Liquid Flow Deposition method for thin film formation. *Applied Science Research*, **3**: p. 438-447.

[165] Meakin, P. and Jullien, R., (1987). Restructuring effects in the rain model for random deposition. *journal de Physique*, **48**(10): p. 1651-1662.

[166] International Centre for Diffraction Data (ICCD Card No:29-1129).

[167] Soltanian, S., Wang, X., Horvat, J., Qin, M., Liu, H., Munroe, P. R., and Dou, S. X. (2003). Effect of grain size and doping level of SiC on the superconductivity and critical current density in MgB/sub 2/superconductor. *IEEE transactions on applied superconductivity*, **13**(2): p. 3273-3276.

[168] Yermekova, Z., Mansurov, Z., and Mukasyan, A. (2010). Influence of precursor morphology on the microstructure of silicon carbide nanopowder produced by combustion syntheses. *Ceramics International*, **36**(8): p. 2297-2305.

[169] Ortiz, A. L., Sanchez-Bajo, F., Cumbrera, F. L., and Guiberteau, F. (2001). X-ray powder diffraction analysis of a silicon carbide-based ceramic. *Materials Letters*, **49**(2): p. 137-145.

[170] Natl.Bur.Stand (US). Monogr. (1976). ICDD Grant-in-Aid. Penn State Univ., University Park, PA, USA.

[171] Kasper, J. S., and Richards, S. M. (1964). The crystal structures of new forms of silicon and germanium. *Acta Crystallographica*, **17**(6): p. 752-755.

[172] Hoyle, S. (1993). ICDD Grant-in-Aid. Penn State Univ., University Park, PA, USA.

[173] Slater, J. C. (1964). Atomic radii in crystals. *The Journal of Chemical Physics*, **41**(10): p. 3199-3204.

[174] Grier, D., and McCarthy, G. (1991). ICDD Grant-in-Aid. *North Dakota State University, Fargo, North Dakota, USA*.

[175] Karunagaran, B., Uthirakumar, P., Chung, S. J., Velumani, S., and Suh, E. K. (2007). TiO2 thin film gas sensor for monitoring ammonia. *Materials Characterization*, **58**(8-9): p. 680-684.

[176] Huang, J., Wang, L., Wen, J., Wang, Y., Lin, C., and Östling, M. (1999). Effect of annealing on SiC thin films prepared by pulsed laser deposition. *Diamond and related materials*, **8**(12): p. 2099-2102.

[177] Keffous, A., Bourenane, K., Kechouane, M., Gabouze, N., and Kerdja, T. (2007). Morphological, structural and optical properties of thin SiC layer growth onto silicon by pulsed laser deposition. *Vacuum*, **81**(5): p. 632-635.

[178] Sun, L., Han, C., Wu, N., Wang, B., and Wang, Y. (2018). High temperature gas sensing performances of silicon carbide nanosheets with an n–p conductivity transition. *RSC advances*, **8**(25): p. 13697-13707.

[179] Yu, C., Liu, Q., He, Z., Gao, X., Wu, E., Guo, J., and Feng, Z. (2020). Epitaxial graphene gas sensors on SiC substrate with high sensitivity. *Journal of Semiconductors*, **41**(3): p. 032101.

[180] Korotcenkov, G. (2007). Metal oxides for solid-state gas sensors: What determines our choice? *Materials Science and Engineering: B*, **139**(1): p. 1-23.

الخلاصة

تم استخدام تقنية الترسيب بالليزر النبضي لتحضير اغشية رقيقة من SiC و SiC:Ag بنسب مختلفة من اوكسيد الفضة wt% (1, 3, 5, and 7) ودراسة الخواص التركيبية والبصرية والكهربائية لها حيث يمكن اعتبار هذه التقنية ذات كفاءة عالية في تصنيع مثل هذه الاغشية. تم ترسيب الأغشية باستخدام ليزر Nd:YAG بطول موجي (1064 nm)، عدد النبضات (1000 نبضة)، معدل التكرارية (6 Hz)، والطاقة لكل نبضة (500 mJ) بينما كان مقدار الضغط داخل غرفة الترسيب (10^{-4} mbar) اما درجة حرارة الركيزة فكانت (250 ℃) تقريبا .

تمت دراسة الخواص التركيبية للأغشية الرقيقة كما رسبت باستخدام تقنية حيود الاشعة السينية (XRD) و اظهرت النتائج ان اغشية يلاحظ كذلك ان أغشية SiC:AgO المشوبة لها تركيب متعددة التبلور مع طور مكعب، و يلاحظ ايضاً ان الزيادة في معدل الحجم البلوري غير منتظمة نتيجة لإضافة ذرات أوكسيد الفضة حيث كانت أعلى قيمه للعينه (1% AgO) بينما اقل قيمه كانت للعينة (7% AgO).

اظهرت نتائج المجهر الالكتروني الماسح (FESEM) والتحليل الطيفي للأشعة السينية المشتتة للطاقة (EDX) أن شكل الجسيمات كان غير منتظم وبأحجام مختلفة تزداد تدريجيا مع زيادة نسب التشويب.

تمت دراسة طبوغرافية السطح للأغشية قيد الدراسة باستخدام مجهر القوة الذرية (AFM) حيث كانت اعلى قيمة لخشونة السطح (Ra) ومعدل الجذر التربيعي (RMS) وحجم الجسيمات كانت للغشاء (3% AgO) وأقل قيمة كانت للغشاء (7% AgO).

تمت دراسة الخواص البصرية للأغشية في المدى الطيفي (200 - 900) nm بينما كان سمك جميع الأغشية قيد الدراسة (200 ± 5) nm نانومتر تقريبا، لقد وجد ان مقدار الزيادة في نسب التطعيم بأوكسيد الفضة ادت الى انخفاض مقدار فجوة الطاقة من (2.61 eV) الى (2 eV) والانتقال من النوع غير المباشر المسموح بالإضافة الى حساب بعض الثوابت البصرية لجميع الأغشية.

تمت دراسة الخواص الكهربائية كتأثير هول حيث اظهرت نتائج الفحص ان قيم ثابت هول (R_H) تقل بشكل تدريجي مع زيادة نسب التشويب وان جميع الأغشية من النوع n (n-type)، كما يلاحظ كذلك انخفاض قيم تحركية حاملات الشحنة (μ_H) لنفس السبب المذكور أعلاه.

الخلاصة

أظهرت خصائص تيار- جهد للمفارق الهجينة المحضرة من الأغشية (SiC:AgO/p-Si) ان تيار الانحياز الامامي عند الاضاءة يتغير اسيا مع الجهد المطبق وان قيم الكفاءة صغيرة جدا تزداد تدريجيا ويعزى ذلك الى زيادة تركيز حاملات الشحنة نتيجة لتغير نسب التطعيم بأوكسيد الفضة.

تمت قياس خواص الاستشعار للأغشية الرقيقة المحضرة بطريقة الترسيب بالليزر النبضي على ركائز من السليكون (SiC:AgO/Si) والزجاج (SiC:AgO/glass) لغاز الامونيا (NH_3) وغاز ثنائي اوكسيد النتروجين (NO_2) عند درجات حرارة تشغيل مختلفة، اظهرت النتائج ان جميع العينات المرسبة على ركيزة السليكون يمكن ان تعمل عند درجة حرارة الغرفة بينما العينات التي يتم ترسيبها على ركيزة الزجاج تعمل عند درجات الحرارة العالية (200 ℃).

بالنسبة للعينات التي رسبت على ركيزة من السليكون الحساسية القصوى لأغشية SiC:AgO (62.98 %) لغاز NO_2 عند (25 ℃) لمستشعر الغاز (3% AgO)، وأن أسرع وقت استجابة كان (12.6s) و (13.5s) للغازات NH_3 و NO_2 عند (100℃) للعينة (3% AgO) اما اسرع وقت استرداد كان (33.3s) و (30.6 s) للغازات NH_3 و NO_2 عند (100℃) و (200 ℃) للعينة SiC.

بالنسبة للعينات التي رسبت على ركائز من الزجاج، الحساسية القصوى لأغشية SiC:AgO تبلغ (90.77 %) و (91.89 %) لغاز NO_2 عند (300 ℃) للعينات (1% AgO) و (7% AgO) على التوالي، وأن أسرع وقت استجابة كان (11.7 s) و (6.3 s) عند (300℃) و (250 ℃) للغازات NH_3 و NO_2 لعينة SiC عند (300℃) و (200℃) على التوالي، اما اسرع وقت استرداد كان (34.2 s) للعينة (1% AgO) عند (250℃).

جمهورية العراق
وزارة التعليم العـالي والبحث العلـمي
جامـــعة بـــابـــل
كليـــة العلـوم للبنات
قســـم فيزيـــاء الليزر

دراسة الخواص التركيبية، البصرية والكهربائية للمفارق الهجينة لأغشية SiC الرقيقة المشوبة بأوكسيد الفضة ذا التراكيب النانوية باستخدام الترسيب بالليزر النبضي لتطبيقات التحسس

أطروحة

مقدمة الى مجلس كلية العلوم للبنات في جامعة بابل

كجزء من متطلبات نيل درجة الدكتوراه فلسفة في العلوم/ فيزياء الليزر وتطبيقاته

من قبل

حسين حمد خضر

بكالوريوس في علوم الفيزياء (الجامعة المستنصرية - 1996)
ماجستير في علوم الفيزياء (جامعة الكوفة - 2017)

بأشراف

أ.م. د. جنان علي عبد

1443 هـ **2022 م**